Plasma Streaming Instabilities in the Laser Wakefield Acceleration Bubble

Lucas Ivan Iñigo Gamiz

Physics Department

University of Strathclyde, Glasgow

July 20, 2022

Abstract

This thesis presents a theory for investigating streaming instabilities in converging geometries in warm and cold plasmas. We address the number density inhomogeneity by approximating the perturbed components with the Wentzel-Kramers-Brillouin (WKB) approximation. In the case of a warm plasma, an isotropic temperature is added to the set of coupled ordinary differential equations and their wavenumbers are obtained. The temporal growth rates are determined by mapping the wavenumbers to the frequency and obtained saddle points. Particle-in-cell (PIC) simulations are performed to support the semi-analytical theory. The PIC simulations demonstrate an agreement to within an order of magnitude of the theoretical predictions for the cold plasma case. The PIC simulations for varying temperature and a fixed mode are performed and demonstrated to be in good agreement of less than an order of magnitude with the theoretical predictions. PIC simulations for fixed temperature and varying azimuthal mode number have been performed and demonstrate to be in good agreement within an order of magnitude with small qualitative differences.

PIC simulations are performed to replicate recent experiments. The simulations demonstrated that electrons are ejected transversely to the laser's propagation direction. They are known as “side electrons”. We then describe the differences between the simulations and experiments. A theory for the mechanism responsible for the azimuthal modulations in the “side electrons” is proposed. Electrons converge on the axis of propagation and are mostly reflected by the large fields given the on-axis charge concentration. Electrons that diverge and then counter-stream with electrons that are converging on-axis. As a result, an electric field co-moves with the back of the bubble thus perpetuatuating an instability. PIC simulations are performed for two colliding electron flows with an in-phase azimuthal sinusoidal modulation for converging geometry. The obtained change of phase in one of the annuli demonstrates the presence of an instability. Further slab geometry simulations are performed for two counter-streaming slabs with in-phase modulations with an asymmetric strength, symmetric strength, a reverse momenta and a reflective boundary. All the simulations demonstrate the growth of the waves. The instabilities considered are the two-stream instability and the current filamentation instability.

Contents

List of Figures

Preface/Acknowledgements

This Ph.D. journey culminating with this thesis could not have without the help of a number of people. First, I would like to thank my dad and mom, Lucas Juan Iñigo Pablovich and Gabriela Gamiz Salido. This thesis is for you. Thank you very much for all your patience, help, guidance and love not only through this journey but all through my life that has led me to this point. Thank you for pushing me to follow my dreams because you believed in me. Los amo, y muchas gracias por todo.

I'd also like to thank Prof. Dino Jaroszynski for supporting me through this Ph.D. and help me become a better researcher and believing in me. I'd like to thank Dr. Bernhard Ersfeld for his incredible support and patience throughout this journey. Thank you for all the discussions and times I've asked for assistance in a seemingly impossible (at the time) tasks and providing powerful insights to better understand complicated problems. I'd like to thank Dr. Samuel Yoffe for his help with all the computational problems I have had and guiding me in my journey of scientific programming. I've also like to thank Dr. Adam Noble for his help with some mathematics problems I have encountered and for our film talks (I still need to finish Twin Peaks!). I also would like to thank Dr. Enrico Brunetti for his help in all computational related issues and for his insight to

approach computational problems. And lastly, I would like to thank Prof. Alan Cairns for his incredible support and help to develop the theories presented in this thesis.

Besides my parents, supervisors, and researchers from our group, I would like to give a special thanks to my friends. I would like to thank my girlfriend, Natasha, for her love and support during this journey. I would like to thank George Holt, Dr. Antoine Matraillan, and Dr. Daniel Ullmann for their friendship. You guys made this journey much more fun and enjoyable, with the obvious exception of the terrible hangovers we ve had whilst I had to work in the weekends. I would like to thank Dr. John Totten for his incredible friendship and his parents, John and Lynn for their care and support. You guys were my "wee Scottish family", and I cannot thank you enough for your love and support. I would also like to thank my brother Daniel and my sister Gabriela. Thank you for all your help and support, those endless CoH games (gracias, Jorge!) and those DST games. On that note, I would also like to thank Hector and Gerardo for their friendship.

Thank you all for your support all the way through this unbelievable journey. It has been a very special one and I am grateful for all the people who have been with me through this.

Chapter 1

Introduction

Plasma is believed to constitute approximately 99% of the matter in the observable universe [1]. Which is more than enough reason to investigate it. The word plasma comes from the Greek word $\pi\lambda\alpha\sigma\mu\alpha$, which means jelly-like material. Irving Langmuir was the first person to systemically study plasma and identified ionized gas with plasma mainly because plasmas had a jelly like diffusion [1]. It is often identified as the fourth state of matter because if enough heat is administered electrons detach from their corresponding nuclei and yield an electrically neutral gas of charged particles. This give the plasma very interesting properties, and even more interesting applications. Plasma is usually created by heating a gas sufficiently to ionize it, or by administering a curring to gas to ionize it.

Plasma physics has been garnering a rather large interest due to its almost never ending array of applications in day-to-day life. Such applications can include welding, plasma-etching, smartphones, television, to state-of-the-art experiments and technology such as nuclear fusion. Considerable research is pursued to develop a way to have an energy reactor via nuclear fusion due that it is almost an infinite amount of clean energy. New and exciting particle acceleration methods have been proposed such as laser and plasma wakefield acceleration. Plasma can be notoriously challenging to control because of its n-particle composition and the electric charge in the plasma. Plasmas are also prone to positive feedback mechanisms that can disturb the overall flow or composition of the plasma, which can lead to unexpected or undesired effects.

1.1 Instabilities

Positive feedback mechanisms that can disrupt the overall flow and composition of plasma are know as plasma instabilities [1]. They come in many forms and are known to plague modern plasma physics experiments. Instabilities can arise from a long list of causes. An example of an instability that occurs both in plasma physics and fluid mechanics is the Kelvin-Helmholtz instability [1]. They occur for two fluids along their boundaries where both fluids propagate in the same direction but have different velocities and densities [1]. In nature, it is commonly observed in clouds as shown in Fig. 1.1.

Figure 1.1: Kelvin-Helmholtz instability in clouds [2]

In plasma, the velocity shear layer will cause exchange of momentum between the two layers [3]. However, this is not the only type of plasma instability. In recent years, there has been an increased interest in streaming-type instabilities because of novel technologies such as inertial confinement fusion [4] (ICF), which, have also reflected in an increase in research publications. In this thesis, we focus in streaming type of instabilities. These occur when two fluids flow relative to each other. A positive feedback loop mechanism persists as long as the two fluids interact which can lead to overall disruption, microstructure formation, and transfer of energy from the particles of each of the species to electromagnetic fields [1, 4].

1.2 Laser Wakefield Acceleration

On the 4th of July 2012, CERN announced the observation of a particle in the 125 GeV mass regime consistent with the Higgs' boson properties. These observations were made using the large hadron collider (LHC), which is a 27 kilometer circumference ring that accelerates particles using electromagnetic fields. Particle accelerators are commonly used to demonstraete the fundamental principles of physics by smashing particles together at high energies. They are usually very large and extremely expensive. An exciting new particle acceleration mechanism that can dramatically reduces the size of particle is the *laser wakefield accelerator* (LWFA).

In 1979, Tajima and Dawson [5] suggested a novel method for particle acceleration using intense ultrashort lasers. By focusing an intense laser pulse into plasma, electrons and ions are driven apart. The displaced electrons are attracted back to the ions. Some electrons form a sheath that surrounds the ion structure and inject into the cavity. After injection, the particles can be accelerated to very high energies in very short distances because of the very high electric fields inside the ion cavity. At the time when the wakefield accelerator was proposed, it was impossible to attain so high intensities. However, chirped pulse amplification, pioneered by Strickland and Mourou [6] resulted in terawatt to petawatt lasers.

1.3 Aim of this thesis

This thesis will explore streaming instabilites in a disk-like geometry where particles converge and diverging into a a common point. These are relevant in a wide range of applications including laboratory plasmas such as LWFA, and extreme astrophysical events such as, coronal mass ejections, and supernovae. We begin by introducing the constraints of these type of geometries and describe instabilities in converging geometries. We also apply a semi-analytical approach to obtain the growth rates and perform particle-in-cell (PIC) simulations to compare with the semi-analytical predictions. We then expand the theory to encompass warm plasma for a more realistic description of instabilities in converging geometries. We repeat the same process described for the cold plasma approach to find an agreement between the theoretical and numerical predictions.

In the following part of the thesis, we present a recent experimental campaign that investigated electrons ejected transversly to the direction of laser propagation. The ejected electrons exhibited features indicating plasma streaming instabilities, particularily the current filamentation instability. We perform full 3D PIC simulations to replicate the experiment and investigate correlations between numerical and experimental results and develop a theoretical description of particle interaction at the back of the LWFA bubble which may explain that the structures are a result from counter-streaming particle interactions leading to instabilities. We perform additional PIC simulations of reduced models to gain insight into the mechanisms underlying the instabilities. Finally, we present the results and conclusions of the study and suggest further studies that can be performed.

Chapter 2

The laser wakefield accelerator

2.1 Introduction

Before proceeding with the thesis, it is paramount to gain an understanding of the concepts underlying the following chapters. We start by introducing electrodynamics and electromagnetic plane waves. We then discuss wave-particle interactions before introducing ponderomotive force and laser wakefield acceleration plasmas. Then we introduce plasma physics, and finally a brief introduction to particle-in-cell codes.

2.2 Electrodynamics

To begin the journey through this thesis, there is no single, more important set of equations than *Maxwell's equations.* These are the foundation of almost everything that will be presented in this thesis. In classical electrodynamics, Maxwell's equations in the vacuum in differential form are:

$$\boldsymbol{\nabla} \cdot \boldsymbol{E} = \frac{\rho}{\epsilon_0}, \tag{2.1}$$

$$\boldsymbol{\nabla} \cdot \boldsymbol{B} = 0, \tag{2.2}$$

$$\boldsymbol{\nabla} \times \boldsymbol{E} = -\partial_t \boldsymbol{B}, \tag{2.3}$$

$$\boldsymbol{\nabla} \times \boldsymbol{B} = \mu_0 \epsilon_0 \partial_t \boldsymbol{E} + \mu_0 \boldsymbol{J}. \tag{2.4}$$

This set of coupled partial differential equations describe the production of electric fields $\boldsymbol{E}$ by charge densities $\boldsymbol{\rho}$ and/or by magnetic fields, $\boldsymbol{B}$, which change in time. The magnetic fields can be produced by either changing electric fields or currents $\boldsymbol{J}$[7]. ϵ_0 is the dielectric constant, μ_0 is the permittivity constant and $c = 1/\sqrt{\epsilon_0 \mu_0}$ is the speed of light. The homogeneous Maxwell's equations imply that the electric and magnetic fields can be rewritten in terms of the scalar, ϕ, and vector potential:

$$\boldsymbol{B} = \boldsymbol{\nabla} \times \boldsymbol{A}, \tag{2.5}$$

$$\boldsymbol{E} = -\boldsymbol{\nabla} \phi - \partial_t \boldsymbol{A}. \tag{2.6}$$

We can substitute back into the inhomogeneous equations (Gauss's law and Ampère's law) to obtain an expression relating the charges and currents to the scalar and vector potentials:

$$\nabla^2 \phi + \nabla \cdot \partial_t \boldsymbol{A} = -\frac{\rho}{\epsilon_0}, \tag{2.7}$$

$$\nabla^2 \boldsymbol{A} - \frac{1}{c^2} \partial_t^2 \boldsymbol{A} - \boldsymbol{\nabla} \left(\boldsymbol{\nabla} \cdot \boldsymbol{A} + \frac{1}{c^2} \partial_t \phi \right) = \mu_0 \boldsymbol{J}. \tag{2.8}$$

These two equations are coupled. However, one can decouple them by exploiting the arbitrariness in the definition of potentials [8]. Because the magnetic field is Eqn. (2.5), the vector potential is arbitrary to the extent that the gradient of some scalar function Λ can be added and the magnetic field is unchanged by this transformation.

$$\boldsymbol{A} \rightarrow \boldsymbol{A}' = \boldsymbol{A} + \boldsymbol{\nabla}.\Lambda \tag{2.9}$$

The scalar potential also needs to be transformed for $\boldsymbol{E}$ to remain unchanged, then we can add the time derivative of the scalar function Λ

$$\phi \rightarrow \phi' = \phi - \partial_t \Lambda \tag{2.10}$$

This implies that we can choose a set of potentials that yield

$$\boldsymbol{\nabla} \cdot \boldsymbol{A} + \frac{1}{c^2}\partial_t \boldsymbol{\phi} = 0, \tag{2.11}$$

and thus will uncouple Eqns. (2.7) and (2.8) and yield two inhomogeneous wave equations corresponding to ϕ and $\boldsymbol{A}$

$$\Box^2 \phi = -\frac{\rho}{\epsilon_0}, \tag{2.12}$$

$$\Box^2 \boldsymbol{A} = -\mu_0 \boldsymbol{J}, \tag{2.13}$$

where $\Box^2 = \nabla^2 - \mu_0 \epsilon_0 \partial_t^2$ is the d'Lambertian operator. The transformations in Eqns. (2.9) and (2.10) are called *gauge transformations*, and the invariance of the fields under such transformation is called *gauge invariance* [8]. Eqn. (2.11) is commonly referred as the *Lorentz gauge* or *Lorentz condition.*

Another gauge which is commonly used through electrodynamics is the *Coulomb gauge* or also known as *radiation* or *transverse gauge*[8]. In this gauge, we set

$$\boldsymbol{\nabla} \cdot \boldsymbol{A} = 0. \tag{2.14}$$

Using this gauge in Eqn. (2.7), we can observe that the scalar potential satisfies Poisson's equation

$$\nabla^2 \phi = -\frac{\rho}{\epsilon_0}, \tag{2.15}$$

which has the solution

$$\phi(\boldsymbol{x}, t) = \frac{1}{4\pi\epsilon_0} \int d^3x' \frac{\rho(\boldsymbol{x}', t)}{\mid \boldsymbol{x} - \boldsymbol{x}' \mid}, \tag{2.16}$$

where $\boldsymbol{x}$ is the position vector of the source charge and $\boldsymbol{x}'$ is the position vector of the charge.

2.2.1 Lorentz Force

Prior to discuss particle-wave interaction, we have to show how they interact. Consider the special case of electrostatics, where source charges are static, the force exerted on a test charge q from a source point charge q_s is calculated using Coulomb's Law:

$$\boldsymbol{F}_{\text{elec}} = \frac{1}{4\pi\epsilon_0} \frac{q_s q}{\mathfrak{r}^2} \hat{\mathfrak{r}}, \tag{2.17}$$

where $\boldsymbol{\mathfrak{r}}$ is the separation vector $\boldsymbol{\mathfrak{r}} = \boldsymbol{r} - \boldsymbol{r}'$ from $\boldsymbol{r}'$ (the location of q_s) to $\boldsymbol{r}$ (the location of q). If we have several points, we take the superposition of all the particles acting upon our test charge and if we have a continuous distribution, we can integrate the distribution accordingly and obtain

$$\boldsymbol{F} = q\boldsymbol{E}. \tag{2.18}$$

Now, consider we have the source and test charges propagating at a constant speed. This current, besides producing an electric field, will produce a magnetic (induction) field. The force of the magnetic induction acting on the test charge is:

$$\boldsymbol{F}_{\text{mag}} = q(\boldsymbol{v} \times \boldsymbol{B}), \tag{2.19}$$

where $\boldsymbol{v}$ is the velocity of the charge. In the presence of both, electric and magnetic fields, a charge will experience a net force from both fields, which lead to the *Lorentz Force Law*

$$\boldsymbol{F} = q\left(\boldsymbol{E} + \boldsymbol{v} \times \boldsymbol{B}\right). \tag{2.20}$$

2.3 Electromagnetic waves

Assuming vacuum, which is charge and current free, one can obtain wave equations for the magnetic and electric fields

$$\Box^2 \boldsymbol{E} = 0, \tag{2.21}$$

$$\Box^2 \boldsymbol{B} = 0. \tag{2.22}$$

The equations above allow for a different solutions. We can use the special case for plane waves and obtain:

$$\boldsymbol{E} = \boldsymbol{E}_0 e^{i\boldsymbol{k}\cdot\boldsymbol{x} - i\omega t}, \boldsymbol{B} = \boldsymbol{B}_0 e^{i\boldsymbol{k}\cdot\boldsymbol{x} - i\omega t}, \tag{2.23}$$

where the amplitudes $\boldsymbol{E}_0$ and $\boldsymbol{B}_0$ are constant and complex; $\boldsymbol{k}$ is the wave-vector and $\boldsymbol{\omega}$ is the frequency. The physical fields would correspond to the real part of the expression. We can put this in terms of the vector potential assuming $\phi = 0$ and using Eqns. (2.5) and (2.6).

$$\boldsymbol{E} = i\omega \boldsymbol{A}_0 e^{i\boldsymbol{k}\cdot\boldsymbol{x} - i\omega t}, \tag{2.24}$$

$$\boldsymbol{B} = i\boldsymbol{k} \times \boldsymbol{A}_0 e^{i\boldsymbol{k}\cdot\boldsymbol{x} - i\omega t}. \tag{2.25}$$

For the charge-free case, Gauss' law for the electric field yields a constraint

$$\boldsymbol{k} \cdot \boldsymbol{A}_0 = 0. \tag{2.26}$$

Faraday's law also yields a further constraint,

$$\boldsymbol{B}_0 = \frac{\boldsymbol{k}}{\omega} \times \boldsymbol{E}_0, \tag{2.27}$$

which show that *electromagnetic waves are transverse* to the direction of propagation and both the electric and magnetic field are in phase and mutually perpendicular.

As an electromagnetic wave travels, it carries energy. The energy flux density is given by the Poynting vector:

$$\boldsymbol{S} = \frac{1}{\mu_0}(\boldsymbol{E} \times \boldsymbol{B}), \tag{2.28}$$

where the energy flow is

$$\boldsymbol{S} = c\epsilon_0 |E|^2 \hat{\boldsymbol{n}}, \tag{2.29}$$

where $\hat{\boldsymbol{n}}$ is the direction of propagation. The intensity is the average power per unit area transported by the electromagnetic wave. In the vacuum, the intensity is:

$$I \equiv \langle S \rangle = \frac{1}{2} c\epsilon_0 |E|^2, \tag{2.30}$$

in terms of the vector potential where $E_0 = i\omega A_0$

$$I = \frac{\omega^2 |A|^2}{2c\mu_0}. \tag{2.31}$$

2.3.1 Particle-Wave Interaction

Before proceeding to more complicated concepts, it is adequate to introduce how a single particle interacts with an electromagnetic wave. Following Gibbon [9], we consider a non-relativistic electron which is under the influence of an EM plane wave traveling in the positive $x-$direction and has a vector potential of the form:

$$\boldsymbol{A} = (0, \delta a_0 \cos(kx - \omega t), (1 - \delta^2)^{1/2} a_0 \sin(kx - \omega t)), \tag{2.32}$$

where a_0 is the normalized amplitude (v/c) and δ is the polarization parameter and $\delta = \{\pm 1, 0\}$. We can use the Lorentz force law, Eqn. (2.20) and the energy equation

$$d_t(\gamma mc^2) = -e(\boldsymbol{v} \cdot \boldsymbol{E}), \tag{2.33}$$

to calculate the influence of the EM wave on the particle. Knowing that $\boldsymbol{F} = d\boldsymbol{p}/dt$, we can separate the perpendicular component:

$$d_t \boldsymbol{p}_\perp = (\partial_t + v_x \partial_x)\boldsymbol{A}. \tag{2.34}$$

We can integrate the equation above over time to obtain:

$$\boldsymbol{p}_\perp - \boldsymbol{A} = \boldsymbol{p}_{\perp,0}. \tag{2.35}$$

The longitudinal components of the momenta will yield

$$\gamma - p_x = \alpha, \tag{2.36}$$

where α is a constant of motion. Because $\gamma^2 = 1 + p_x^2/m^2c^2 + p_\perp^2/m^2c^2$, a relationship between the longitudinal and perpendicular components of the momenta is obtained:

$$2\alpha p_x = 1 - \alpha^2 + p_\perp^2. \tag{2.37}$$

In the average rest frame, we set the drift velocity $p_x = 0$, and obtain:

$$1 + \langle A^2 \rangle - \alpha^2 = 0. \tag{2.38}$$

We can also average over laser cycle to remove the rapidly varying terms , we get

$$\alpha = \sqrt{1 + \frac{a_0^2}{2}}. \tag{2.39}$$

The parameter alpha is found to be γ_0. We can substitute equation above to and obtain the components of the momenta

$$p_x = (2\delta^2 - 1)\frac{a_0^2}{4\gamma_0}\cos(2(kx - \omega t)), \tag{2.40}$$

$$p_y = \delta a_0 \cos(kx - \omega t), \tag{2.41}$$

$$p_z = (1 - \delta^2)^{1/2} a_0 \sin(kx - \omega t). \tag{2.42}$$

The trajectory of the electron can be obtained by integrating once more in time and will yield a “figure of eight” motion [9].

2.4 Ponderomotive Force

The consequence of EM fields interacting with particles is the *ponderomotive force* or *ponderomotive effect*. Ponderomotive effects are due to oscillating EM fields that have a spatial gradient that push electrons from high field areas to low field areas [10]. It is also referred to as field-gradient force [11]. The ponderomotive force has been derived extensively in literature [11, 12, 13, 14, 15, 16]. In this thesis, we will follow Gibbon's more tractable approach [9]. Let us consider the Lorentz force on an electron in terms of the vector potential (assuming $\phi = 0$):

$$\partial_t \boldsymbol{p} + (\boldsymbol{v} \cdot \boldsymbol{\nabla})\boldsymbol{p} = -\frac{e}{c}\left(\partial_t \boldsymbol{A} - \boldsymbol{v} \times (\boldsymbol{\nabla} \times \boldsymbol{A})\right). \tag{2.43}$$

The double product yields $\boldsymbol{v} \times (\boldsymbol{\nabla} \times \boldsymbol{A}) = \nabla(\boldsymbol{v} \cdot \boldsymbol{A}) - (\boldsymbol{v} \cdot \boldsymbol{\nabla})\boldsymbol{A}$. Combining the last term with the partial time derivative on the r.h.s., we obtain the total time derivative of the vector potential

$$\frac{d\boldsymbol{p}}{dt} = e\frac{d\boldsymbol{A}}{dt} - e\nabla(\boldsymbol{v} \cdot \boldsymbol{A}). \tag{2.44}$$

By inspecting eqn (2.44), we can see a separation of timescales. The first term of eqn. (2.44) drives fast oscillations

$$\frac{d\boldsymbol{p}_f}{dt} = e\frac{d\boldsymbol{A}}{dt}. \tag{2.45}$$

The effects of the second term, which occur on a slower timescale, are obtained by taking the average over one laser cycle, denoted as $\langle ... \rangle$:

$$\frac{d\boldsymbol{p}_s}{dt} = -q\langle \nabla(\boldsymbol{v} \cdot \boldsymbol{A})\rangle \tag{2.46}$$

Eqn. (2.46) can be rewritten by replacing the velocity with the momentum as $\boldsymbol{p} = \gamma m_e \boldsymbol{v}$ to the usual ponderomotive force expression by

$$\boldsymbol{F}_p = -mc^2 \nabla\langle\gamma\rangle \tag{2.47}$$

where $\gamma = (1 + p_s^2/(m^2c^2) + a_0^2/2)^{1/2}$. This expression, as initially stated, corresponds to the ponderomotive force affecting a single electron.

2.5 Laser Wakefield Acceleration

As a laser pulse propagates through a plasma, it excites a co-propagating plasma wave that trails the pulse. In the linear 3D regime, we can examine the wakefield generation using the cold fluid equations. Following Sprangle *et al* [17], we can calculate the plasma wave starting from Eqns. (2.4), (2.3) and using Eqn. (2.1),

$$\Box^2 \boldsymbol{E} = \frac{1}{c^2\epsilon_0}\partial_t \delta\boldsymbol{J} + \frac{e}{\epsilon_0}\nabla(\delta n), \tag{2.48}$$

where $\delta\boldsymbol{J}$ and δn are the plasma response current and number density. We can also obtain the velocity and density response using the linearised momentum and continuity equations

$$\partial_t \delta \boldsymbol{u} = -\frac{e}{m}\nabla\phi - \frac{1}{m}\boldsymbol{F}_{\text{pond.}}, \tag{2.49}$$

$$\partial_t \delta n = -n_0 \nabla \cdot \delta \boldsymbol{u}. \tag{2.50}$$

By taking the divergence of Eqn. (2.49) and taking the partial derivative with respect to time in Eqn. (2.50) substituting the former into the latter and dividing both sides by the background density n_0 and using the ponderomotive force, Eq. 2.47, in the linear limit $a \ll 1$ [18]

$$\left(\partial_t^2 + \omega_p^2\right)\frac{\delta n}{n_0} = c^2\nabla^2 a^2/2, \tag{2.51}$$

$$\left(\partial_t^2 + \omega_p^2\right)\phi = -\frac{\omega_p^2 a^2}{2}. \tag{2.52}$$

With ϕ being the electrostatic potential of wake in the limit $a^2 << 1$, and

$$\omega_p = \sqrt{\frac{e^2 n_0}{m_e \epsilon_0}} \tag{2.53}$$

is the plasma frequency. The causal solution of Eqn. (2.51) is:

$$\delta n/n_0 = (c^2/\omega_p)\int_{-\infty}^{t} dt' \sin[\omega_p(t-t')]\nabla^2 a^2(\boldsymbol{r},t')/2, \tag{2.54}$$

and the electric field of the wake is:

$$\boldsymbol{E}/E_0 = -c\int_0^t dt' \sin[\omega_p(t-t')]\nabla a^2(\boldsymbol{r},t')/2. \tag{2.55}$$

These two equations are valid for $E \ll E_0$, where $E_0 = m_e c\omega_p/e$. They describe plasma waves driven by the ponderomotive force, which oscillate at the plasma frequency ω_p after the driving force have passed. The solutions to Eqns (2.54) and (2.55) indicate that the most effective generation of wakefields will be when the driver's envelope scale length is on the order of the plasma wavelength [18]

$$\lambda_p = \frac{2\pi c}{\omega_p}. \tag{2.56}$$

Besides the axial (relative to the driver's propagation axis) wakefield E_z, transverse wakefields E_r and B_θ will be generated in the frame of reference of the driver and are related to the axial wakefield by the Panofsky-Wenzel theorem, $\partial_r E_z = \partial_{z-ct}(E_r - B_\theta)$ [18].

Plasmas can support large amplitude electrostatic waves with phase velocities near the speed of light [18]. The electric field of a plasma wave has the form

$$E_z = E_{\max} \sin[\omega_p(z/v_p - t)], \tag{2.57}$$

where v_p is the phase velocity. A particle, in the case an electron can ride the plasma wave staying in phase with the electric field. For a longitudinal propagating wave, an increase in initial amplitude can lead to amplitude distortion which can lead the elimination of the oscillation, or as it is described more commonly, *wave breaking.* Dawson [19] presented a very tangible example for a 1-D wave and derived the cold nonrelativistic wave breaking field as

$$E_{\text{WB}} = \frac{en_0}{\epsilon_0 k_p}, \tag{2.58}$$

For nonlinear relativistic plasma waves, the amplitude of the waves can exceed E_{WB}. The corrections have been calculated in the literature [18, 20]. Wave breaking has significant importance since it can lead to self-trapping and acceleration of electrons by the plasma wave [21].

For the plasma wakefield in 3D described above, the sinusoidal form of the electric field can continue in the linear regime, however, in the nonlinear regime, the structure departs greatly from the sinusoidal form described above. One effect of the nonlinearities is that the wave front of the plasma can be curved; another effect is that the laser intensity can be sufficiently high to expel all the electrons near the axis of propagation [18, 21]. The region where the electrons are expelled is called the “ion cavity” or “bubble” [21, 22]. Ions in this region can be considered to be immobile since their response length is assumed to be larger than the cavity radius [21]. The electrons form a narrow, high density sheath surrounding the cavity. The space charge of the ions pull back the electrons , which establishes a wake in the form of a closed bubble [23]. The shape of this bubble depends on the laser pulse shape and intensity. For properly matched parameters, it is spherical [23].

Electrons can be injected into the bubble and accelerate to very high energies over short distances. Several methods of particle injection have been discussed in literature, ranging, among others [15], from ponderomotive injection [18] to self-injection due to density gradients [24]. We will briefly discuss the latter case. Bulanov *et al.* presented the concept of injection using a density gradient with scale length long compared to the plasma wavelength, which will induce wave breaking. A decrease in the plasma density causes the plasma wavelength to increase, which leads the plasma wave fronts falling behind the laser. This decreases the wake phase velocity to trap background plasma electrons [18]. This mechanism has been proposed for injecting attosecond bunches [25]. As previously mentioned, the bubble can be considered as a spherical ion bubble surrounded by a thin high density electron sheath following the laser driver. A simplified calculation can be performed by assuming a spherical bubble shape, and using a quasistatic approximation in a Galilean reference frame moving with the laser pulse. The fields inside the bubble have been calculated in the literature [21, 26] Electron trajectories can be calculated using the fields calculated from the moving ion bubble [26, 27]. Some of the electrons are ejected, others continue to form further bubbles following the first, and others are ejected obliquely to the direction of propagation. These electrons are usually referred to as “side electrons” [28].

2.6 Plasma

The simplest description of plasma is that it is ionized gas [1]. A more accurate description can be found in Swanson’s book “Plasma Waves” [29]: “The plasma state is a characterization of matter where long-range electromagnetic interactions dominate the short-range interatomic or intermolecular forces among a large number of particles” [29]. A plasma corresponding to a mixture of ions and electrons is a collection of particles which their overall net charge is zero. However, we allow for local and/or periodic deviations from exact neutrality [29]. This is known as the quasineutrality condition. Electrons will oscillate due the restoring force of the ions and will oscillate at the *plasma frequency* ω_p. Since plasma is a collection of particles, it is natural to describe plasma using statisical mechanics. Classically, a microscopic description involves a point charges in phase space, for which we can write a microscopic distribution function depending on the location of each of the particles as:

$$N(\boldsymbol{r}_1, \boldsymbol{r}_2, ..., \boldsymbol{r}_N, \boldsymbol{v}_1, \boldsymbol{v}_2, ..., \boldsymbol{v}_N, t) = \prod_{j=1}^{N} \delta(\boldsymbol{r} - \boldsymbol{r}_j(t))\delta(\boldsymbol{v} - \boldsymbol{v}_j(t)). \tag{2.59}$$

The description using this distribution function and Maxwell's equations, albeit complete, can involve the solution to a large number of equations. Therefore, a more tractable way is to use a macroscopic distribution where the physical quantities are averaged over a microscopic distribution function $f(\boldsymbol{r}, \boldsymbol{v}, t)$, e.g., the particle density in configuration space, $n(\boldsymbol{r}, t)$, is

$$n(\boldsymbol{r}, t) = \int f(\boldsymbol{r}, \boldsymbol{v}, t) d^3\boldsymbol{v}, \tag{2.60}$$

where the distribution function' $f(\boldsymbol{r}, \boldsymbol{v}, t)$ arguments, position $\boldsymbol{r}$, velocity $\boldsymbol{v}$ and time t are 7-dimensional. The evolution of the distribution function is described by Vlasov-Boltzmann equation coupled to Maxwell's equations (2.1) to (2.4) [1, 29]

$$\partial_t f + \boldsymbol{v} \cdot \boldsymbol{\nabla} f + \frac{\boldsymbol{F}_{\text{Lorentz}}}{m} \cdot \boldsymbol{\nabla}_{\boldsymbol{v}} f = (\partial_t f)_{\text{coll.}} \,. \tag{2.61}$$

Where $\boldsymbol{\nabla_v}$ is the gradient in velocity space, and the term on the r.h.s is the collision term. The collision term accounts for the transfer of momentum from plasma particles via Coulomb forces. The collisions tend to relax the distribution function to thermal equilibrium [29]. However, for the purposes in this section, we will use the collisionless Vlasov equation

$$\partial_t f + \boldsymbol{v} \cdot \boldsymbol{\nabla} f + \frac{\boldsymbol{F}_{\text{Lorentz}}}{m} \cdot \boldsymbol{\nabla_v} f = 0. \tag{2.62}$$

This thesis focuses in the *fluid equations*, which follow from a moment expansion of the Vlasov equation. Following from Swanson, chapter 3 [29], the number density is:

$$n = \int f(\boldsymbol{r}, \boldsymbol{v}, t) d^3\boldsymbol{v}. \tag{2.63}$$

Since, $\boldsymbol{r}$ and $\boldsymbol{v}$ are independent variables, $f\boldsymbol{\nabla} \cdot \boldsymbol{v} = 0$ and $f\boldsymbol{\nabla_v} \cdot \boldsymbol{F} = 0$ due to the orthogonality between the cross product of $\boldsymbol{v}$ and $\boldsymbol{B}$ and $\boldsymbol{\nabla_v}$. We can introduce a function of velocity, namely $Q(\boldsymbol{v})$ and we define the moment process by an average of the velocity

$$\langle Q \rangle = \frac{1}{n} \int Q f d\boldsymbol{v}. \tag{2.64}$$

We multiply the collisionless Vlasov equation by Q and integrate over velocity

$$\partial_t \int Q f d\boldsymbol{v} + \boldsymbol{\nabla} \cdot \int Q \boldsymbol{v} f d\boldsymbol{v} + \frac{1}{m} \int Q \boldsymbol{\nabla_v} \cdot \boldsymbol{F} f d\boldsymbol{v} = 0. \tag{2.65}$$

The term containing the force $\boldsymbol{F}/m$ is simply the acceleration, $\boldsymbol{a}$. The third term on the l.h.s. can be re-written according to the product $\nabla_{\boldsymbol{v}} \cdot (Q\boldsymbol{a}f) = \boldsymbol{a}f \cdot \nabla_{\boldsymbol{v}} + Q\nabla_{\boldsymbol{v}} \cdot \boldsymbol{a}f$

and obtain, using the divergence theorem [30], $\int_{\mathcal{V}} \nabla \cdot \boldsymbol{h} d\boldsymbol{x} = \oint_{\mathcal{S}} \boldsymbol{h} \cdot \hat{\boldsymbol{n}} d^2x$,

$$\int Q\boldsymbol{\nabla}_{\boldsymbol{v}} \cdot \boldsymbol{a} f d\boldsymbol{v} = \oint_{\mathcal{S}_v} (Q\boldsymbol{a}f) \cdot d\boldsymbol{S}_v - \int f\boldsymbol{a} \cdot \boldsymbol{\nabla}_{\boldsymbol{v}} Q d\boldsymbol{v}. \tag{2.66}$$

We assume that the distribution disappears sufficiently fast as $v \to \infty$ so the surface integral vanishes. We then obtain:

$$\partial_t(n\langle Q\rangle) + \nabla \cdot (n\langle Q\boldsymbol{v}\rangle) - n\langle \boldsymbol{a} \cdot \boldsymbol{\nabla}_{\boldsymbol{v}} Q\rangle = 0. \tag{2.67}$$

To obtain the 0-th moment, we let $Q = 1$, which implies $\langle Q\rangle = 1$ and $\langle Q\boldsymbol{v}\rangle$, where $\langle \boldsymbol{v}\rangle = \boldsymbol{u}(\boldsymbol{r}, \boldsymbol{v}, t)$ is the mean velocity of the fluid element at position r and time t. The third term on the l.h.s. vanishes and we find the *continuity equation*

$$\partial_t n + \boldsymbol{\nabla} \cdot (n\boldsymbol{u}) = 0. \tag{2.68}$$

Taking the first moment, we can let $Q = m\boldsymbol{v}$ and let $\boldsymbol{v} = \boldsymbol{u} + \boldsymbol{w}$, where $\boldsymbol{w}$ measures the perturbation from the average velocity $\langle w\rangle = 0$, we now obtain $\langle Q\rangle = m\boldsymbol{u}$, $\langle Q\boldsymbol{u}\rangle = nm\boldsymbol{u}\boldsymbol{u} + nm\langle \boldsymbol{w}\boldsymbol{w}\rangle$, $\langle \boldsymbol{a} \cdot \boldsymbol{\nabla}_{\boldsymbol{v}} Q\rangle = m\langle a\rangle = q\left(\boldsymbol{E} + \boldsymbol{u} \times \boldsymbol{B}\right)$. Putting everything together, we obtain the *momentum equation*

$$m\left(\partial_t \boldsymbol{u} + (\boldsymbol{u} \cdot \boldsymbol{\nabla})\boldsymbol{u}\right) + m\nabla \cdot \langle \boldsymbol{w}\boldsymbol{w}\rangle - q\left(\boldsymbol{E} + \boldsymbol{u} \times \boldsymbol{B}\right) = 0. \tag{2.69}$$

$nm\nabla \cdot \langle \boldsymbol{w}\boldsymbol{w}\rangle$ is known as the *stress tensor*. Assuming a cold plasma, the small fluctuations in the velocity are negligible and the momentum equation takes the following form

$$nm\left(\partial_t \boldsymbol{u} + (\boldsymbol{u}\cdot\boldsymbol{\nabla})\boldsymbol{u}\right) - qn\left(\boldsymbol{E} + \boldsymbol{u}\times\boldsymbol{B}\right) = 0 \tag{2.70}$$

Further moments can be taken to obtain the energy-momentum stress flux, etc. The moments are usually taken as

$$F^{(\alpha)} = \int v^{\alpha} f(\boldsymbol{v}, t) d^3\boldsymbol{v}, \tag{2.71}$$

where the superscript α corresponds to the order. The hierarchy of moments is terminated by assuming a thermodynamic process.

A plethora of waves with different properties determined by the interaction of electromagnetic waves and free charges can exist and propagate in a plasma. Linear waves are characterised by their frequency and wavenumber, which are linked by a *dispersion relation*. There are different ways to obtain these dispersion relations, which will be studied in more detail in the next chapter.

2.7 Particle-In-Cell simulations

The nature of plasmas being a collection of many particles often leads to analytical model simplifications. Albeit the analytical models can be excellent, there is a need to validate through numerical modelling. A widely-used tool for modelling plasmas and laser-plasma interactions are particle-in-cell (PIC) codes. In PIC codes, the particle distributions are represented by discrete macroparticles, each of which correspond to a, possibly large, number of plasma particles. In each time step, the charges and currents of the macroparticles are deposited on the points of a grid and used to update the EM fields. Then, the fields are interpolated to the positions of the macroparticles and used to update their momenta.

PIC codes numerically integrate Vlasov-Maxwell's equations with respect to time using a finite-difference time-domain (FDTD) method [31, 32]. The FDTD is standard in most PIC codes to solve Maxwell's equations numerically [33]. The most common FDTD schemes use a "Yee" staggered grid [32, 33] where continuous space-time is discretized. Maxwell's equations are then discretized by using central-difference approximations methods. To assure stability and that the electromagnetic field does not change significantly, the Courant-Friedrichs-Lewy (CFL) condition has to be satisfied [32]. The electric and magnetic fields specified on a Yee staggered grid means that the centered second order accurate derivatives are easily implemented [33], e.g.,

$$(\partial_x E_y)_{i+\frac{1}{2},j,k} = \frac{E_{y_{i+1,j,k}} - E_{y_{i,j,k}}}{\Delta x}, \tag{2.72}$$

where Δx is the distance between cells in the $x-$direction, and the subscripts i, j, k correspond to the grid points, as stated in Yee [32] $(i, j, k) = (i\Delta x, j\Delta y, k\Delta z)$. A "leap-frog" method is used, which solves the equations of motions at interleaved times [31]. When the fields have been calculated, the particle position and momentum are updated using a particle "pusher" which numerically integrates the relativistic equations of motion under the Lorentz force for each macroparticle in the simulation. Most PIC codes use the Boris rotation algorithm [33]. Some other PIC codes use a Vay pusher since the Boris pusher is not Lorentz-invariant.

PIC codes are vulnerable to artefacts that yield unphysical phenomena, which can ruin the investigation such numerical instabilities and numerical heating [31]. The latter corresponds to the grid adding an artificial temperature to the particles [31, 33]. The temperature addition can be attributed to unphysical "random" force fluctuations of the grid upon the particles [31, 34] According to Abe *et al*, the force fluctuations are due to a non-physical force due to the grid [34]. Self-heating is related to the Debye length is resolved by the grid size, it is also related to number of particles per cell [33].

In this thesis, we will use three different PIC codes, namely, `EPOCH` [33], `FBPIC \cite{lehe_spectral_2`
Whilst `EPOCH` and `OSIRIS` are in cartesian geometry, `FBPIC` uses a cylindrical geometry with azimuthal Fourier mode decomposition of the electromagnetic field components. The `EPOCH` simulations are in 2D, FBPIC are in quasi-3D, and `OSIRIS` is in full 3D.

2.8 Summary

In this chapter, we have introduced the main concepts for the later chapters of this thesis. We have introduced electrodynamics and the ansatz of plane waves. We have calculated the interaction between electromagnetic plane waves and particles using the Lorentz force law and derived the equations of motion. Having discussed particle-wave interaction and plasma, we introduced the ponderomotive force and the laser wakefield acceleration. We discussed mechanisms for injecting plasma electrons into the wakefield. Later, we discussed plasma using a statistical distribution functions, which are governed by the Vlasov-Maxwell equations. By taking moments, we obtained a fluid description of the plasma. Finally, we introduced particle-in-cell codes, that are commonly used to numerically verify analytical predictions. In the next chapter, we will delve further into plasma waves and plasma instabilities.

Chapter 3

Plasma Streaming Instabilities

3.1 Introduction

Investigation on astrophysical phenomena [36] such as supernovae [37], gamma ray bursts [4, 38], coronal mass ejectors [39, 40], and the recent onset of new development of technologies including, but not limited to, inertial confinement fusion (ICF) [4], tokamaks [41, 42, 43], and LWFA, has lead to an increase in the investigations of instabilities [4]. In this chapter, we introduce the main concepts of plasma instabilities, precisely, plasma streaming instabilities. We introduce waves in plasmas, the general process of studying waves in plasmas, and then continue with instabilities and their properties, unstable growth, and the two main types of instabilities. The effects of different plasma properties on streaming instabilities by discussing relativistic plasmas, warm plasmas and inhomogeneous plasmas are discussed. In each section, we introduce basic derivations and properties of the instabilities. In this thesis, we focus on streaming instabilities, such as the two-stream instability, current filamentation instability and a combination of both.

3.2 Waves in Plasma

Plasma is a collection of electrons and ions where the overall charge of the system is zero but due to Coulomb interaction, periodic deviations from exact neutrality occur naturally. This is known as quasineutrality [1, 29]. The motion of plasma usually results in waves [29]. Laboratory plasmas can be heated and probed by waves, can be disturbed using intense lasers [5], so the study of wave propagation is paramount in plasma physics. The usual approach to studying plasma waves in the linear regime is to obtain an equation relating the angular frequency, ω, to the wavenumber, k, which is known as the dispersion relation. The dispersion relation can be obtained from the continuity, momentum, and Maxwell's equations [1, 8, 29]

$$\partial_t n = -\nabla \cdot (n\boldsymbol{u}), \tag{3.1}$$

$$(\partial_t + \boldsymbol{u} \cdot \boldsymbol{\nabla})\boldsymbol{p} = q\left(\boldsymbol{E} + \boldsymbol{u} \times \boldsymbol{B}\right) - \nabla \boldsymbol{P}/n, \tag{3.2}$$

$$\nabla \cdot \boldsymbol{E} = \frac{\rho}{\epsilon_0}, \tag{3.3}$$

$$\nabla \cdot \boldsymbol{B} = 0, \tag{3.4}$$

$$\nabla \times \boldsymbol{E} = -\partial_t \boldsymbol{B}, \tag{3.5}$$

$$\nabla \times \boldsymbol{B} = \frac{1}{c^2}\partial_t \boldsymbol{E} + \mu_0 \boldsymbol{J}. \tag{3.6}$$

A common approach to describe waves in plasmas is by linearisation using perturbation theory [1, 29, 44]. We can apply perturbation theory where an equilibrium solution is expanded to a first order [45] where $\tilde{\psi}/\bar{\psi} \ll 1$, ψ corresponds to any of the quantities describing the plasma or electromagnetic fields, the tilde denotes perturbation, and bar equilibrium. In a linear system, the perturbations can be assumed to be harmonic, oscillating along the equilibrium solution and can be represented by the superposition of the equilibrium and the perturbation as:

$$\psi = \bar{\psi} + \tilde{\psi} \tag{3.7}$$

We first need to find the response of the plasma to an electric field perturbation, i.e, the *dielectric tensor*. Combining it with Maxwell's equations yields a description of wave propagation. Let us consider a homogeneous, non-relativistic, collisionless, charge and current neutral plasma, i.e., $\sum_j q_j \bar{n}_j = 0$ and $\sum_j q_j \bar{n}_j \bar{\boldsymbol{u}}_j = 0$ and $\bar{\boldsymbol{E}} = \bar{\boldsymbol{B}} = 0$, where the subscript j denotes the species. The continuity and momentum equations can be linearized and since the equilibrium solutions are assumed to be spatially homogeneous and time-independent, assuming harmonic dependence $\exp(ik_z - i\omega t)$. The differential operators multiplied with the perturbed components, assuming a constant amplitude, can be replaced as: $\boldsymbol{\nabla} \rightarrow i\boldsymbol{k}, \partial_t = -i\omega$. The continuity and momentum equations take the following forms:

$$i\omega \tilde{n}_j = i\boldsymbol{k} \cdot \left(\tilde{n}_j \bar{\boldsymbol{u}}_j + \bar{n}_j \tilde{\boldsymbol{u}}_j \right), \tag{3.8}$$

$$i \left(\bar{\boldsymbol{u}}_j \cdot \boldsymbol{k} - \omega \right) \tilde{\boldsymbol{u}}_j = \frac{q_j}{m_j} \left(\tilde{\boldsymbol{E}} + \bar{\boldsymbol{u}}_j \times \tilde{\boldsymbol{B}} \right) - \nabla P_j/(n_0 m_j), \tag{3.9}$$

where m_j is the mass of species j. From Faraday's and Ampère's equation, one obtains:

$$i\boldsymbol{k} \times \tilde{\boldsymbol{E}} = i\omega \tilde{\boldsymbol{B}}, \tag{3.10}$$

$$i\boldsymbol{k} \times \tilde{\boldsymbol{B}} = -\frac{i\omega}{c^2}\tilde{\boldsymbol{E}} + \mu_0 \sum_j \tilde{\boldsymbol{J}}_j, \tag{3.11}$$

One can substitute Eq. (3.10) into Eq. (3.11) to eliminate $\tilde{\boldsymbol{B}}$.

$$i\boldsymbol{k} \times \left(\boldsymbol{k} \times \tilde{\boldsymbol{E}}\right) = -\frac{i\omega^2}{c^2}\tilde{\boldsymbol{E}} + \omega\mu_0 \sum_j \tilde{\boldsymbol{J}}_j. \tag{3.12}$$

The current density can be expressed as: $\tilde{\boldsymbol{J}}_j = q_j \left(\tilde{\boldsymbol{u}}_j \bar{n}_j + \bar{\boldsymbol{u}}_j \tilde{n}_j\right)$. We can rearrange Eqn. (3.12):

$$k^2\tilde{\boldsymbol{E}} - \boldsymbol{k}(\boldsymbol{k} \cdot \tilde{\boldsymbol{E}}) = \frac{\omega^2}{c^2}\left(\boldsymbol{I} + \frac{i}{\epsilon_0 \omega}\underline{\boldsymbol{\sigma}}\right)\tilde{\boldsymbol{E}}, \tag{3.13}$$

where $\underline{\boldsymbol{\sigma}}$ is the *conductivity tensor* [1]. We can simplify and define the dielectric tensor as:

$$\underline{\boldsymbol{\epsilon}} = \epsilon_0 \left(\boldsymbol{I} + \frac{i}{\epsilon_0 \omega}\underline{\boldsymbol{\sigma}}\right). \tag{3.14}$$

Eqn. (3.13) can be written in the form:

$$\underline{\boldsymbol{\chi}} \cdot \tilde{\boldsymbol{E}} = 0, \tag{3.15}$$

with

$$\underline{\boldsymbol{\chi}} = \omega^2 \mu_0 \underline{\boldsymbol{\epsilon}} + \boldsymbol{k} \otimes \boldsymbol{k} - k^2 \boldsymbol{I}, \tag{3.16}$$

where the symbol $\otimes$ denotes the dyadic product. The dispersion relation is then derived from the determinant of the tensor $\underline{\boldsymbol{\chi}}$ being equal to zero.

As an example, we consider an unmagnetized plasma consisting of electrons neutralized by ions that are homogeneous, $\bar{\boldsymbol{u}} = 0$, with a small temperature $\bar{T} \neq 0$. For a wave propagating in z-direction, the wave vector is $\boldsymbol{k} = k_z \hat{e}_z$. We want to find the wave number k_z. Assuming an adiabatic equation of state, the pressure perturbation can be related to $\tilde{n}_e$ by $\tilde{p}_j = 3Tk_B\tilde{n}_j$ and no $\boldsymbol{B}$ field. The linearized continuity and momentum equations take the following form:

$$\begin{aligned}
\tilde{n} &= \frac{\bar{n}}{\omega}\boldsymbol{k} \cdot \tilde{\boldsymbol{u}}, \\
\tilde{\boldsymbol{u}} &= -\frac{ie}{m_e\omega}\tilde{\boldsymbol{E}} + \frac{3k_BT}{\omega n_0 m_e}\tilde{n}\boldsymbol{k}.
\end{aligned}$$

We can find the dispersion relation for $\boldsymbol{k} \parallel \bar{\boldsymbol{u}}$ using Gauss's law and replacing $\tilde{n}$. This result is the Bohm-Gross dispersion relation [1, 46]

$$\omega^2 = \omega_p^2 + 3v_t^2k^2, \tag{3.17}$$

where $\omega_p = \sqrt{ne^2/(m_e\epsilon_0)}$ is the plasma frequency and $v_t = \sqrt{k_BT/m_e}$ is the thermal velocity. This dispersion relation corresponds to an electrostatic Langmuir wave.

Equation 3.17 is an approximation only valid for $kv_t/\omega_p \ll 1$ and is strongly modified by kinetic effects. The Langmuir wave is heavily Landau damped for $kv_t/\omega_p > 0.3$. For low mode numbers k, the wave phase velocity can be arbitrarily large; in contrast, the group velocity tends to 0 as $k \to 0$, meaning that no information or energy propagates

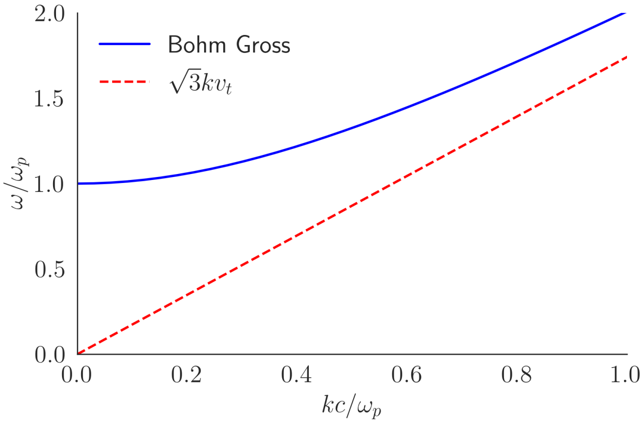

Figure 3.1: Bohm-Gross dispersion relation (solid blue) and the line which the Bohm-Gross dispersion relation asymptotically approaches as $k \to \infty$ (dashed red).

[1]. The oscillations at low k can be referred to as plasma oscillations [1].

Waves in plasmas can be generally studied by solving for the frequency in the secular equation. Such approach allows for a plethora (or as Swanson describes: "zoo") of waves ocurrying in magnetized [1, 29], non-neutral [47], inhomogeneous [29, 48, 49], warm [4, 50], relativistic [4], and combinations thereof [48, 51, 52]. However, plasma waves can be subject to positive feedback leading to growth of the amplitude of oscillation and then on disruption of the plasma. Energy from the particles can be transferred to the fields [1, 29].

3.3 Instabilities

In plasma physics literature, there are many examples of instabilities [4, 29, 53, 54, 55, 56, 57]. An instability occurs when a propagating wave evolves in time into a growing wave in time or space [29]. Whenever the dispersion relation, $D(\omega, k) = 0$, has either complex solutions ω for real k, or vice versa, the wave $\exp(i\boldsymbol{k}\cdot\boldsymbol{x} - i\omega t)$ can be described as stable or unstable, depending on whether the wave grows or decays in time. The usual nomenclature for an unstable wave growing in time, is if for some real k with $\omega = \omega_{\rm re} + i\omega_{\rm im}$, the frequency has a positive imaginary part. Plasma physics literature usually classifies instabilities into two different types: convective and absolute instabilities [29, 57, 58]. An absolute instability is an instability that leads to growth at every point in space. A convective instability occurs for a growing disturbance propagating in space. Such a disturbance can grow at a fixed point in space, but may decay in time [29, 57, 58] after it has propagated on.

The following discussion of instabilities follows Briggs [57] and Swanson [29]. We can introduce a localized source to have an explicit interpretation.

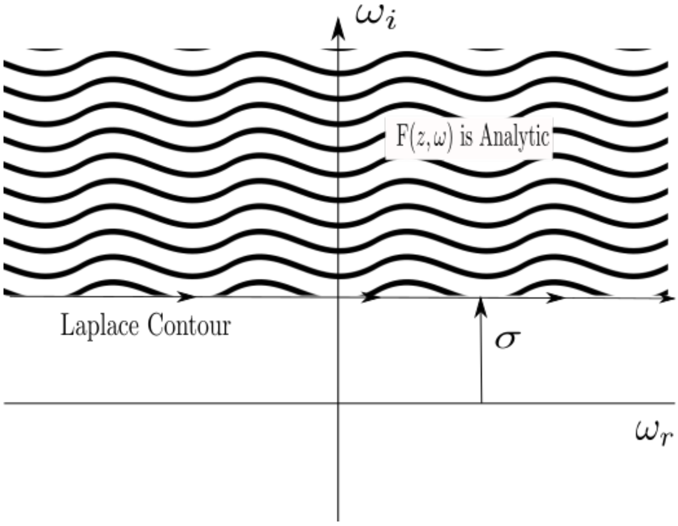

Figure 3.2: Analytic region of $F(z,\omega)$

The system can be assumed to be infinite and uniform in the z direction but have a bounded source as $g(z) = \Theta(z-a)\Theta(a-z)$, where Θ is the Heaviside function. Using

Fourier transform in space, we obtain:

$$g(k) = \int_{-\infty}^{\infty} dz g(z) \exp(-ikz) = \frac{2}{k} \sin(ka). \tag{3.18}$$

Laplace transforms are used to ensure that the source vanished for $t < 0$. We assume a steady-state source of the form:

$$f(t) = \exp(-i\omega_0 t), \tag{3.19}$$

with real frequency ω_0. Its Laplace transform ($F(s) = \int_0^\infty f(t)e^{-st}dt$) then is:

$$f'(\omega) = \frac{1}{\omega - \omega_0}. \tag{3.20}$$

The response of the plasma to the source can be represented in terms of Green's functions, or in terms of transform of the Green's functions $G(k, \omega)$ as:

$$\psi(z,t) = \int_{-\infty+i\sigma}^{\infty+i\sigma} \frac{d\omega}{2\pi} \int_{-\infty}^{\infty} \frac{dk}{2\pi} G(k,\omega) g(k) f(\omega) \exp(ikz - i\omega) \tag{3.21}$$

Eqn. (3.21) can be rewritten as:

$$\psi(z,t) = \int_{-\infty+i\sigma}^{\infty+i\sigma} F(z,\omega) f(\omega) \exp(-i\omega t) \frac{d\omega}{2\pi}, \tag{3.22}$$

with

$$F(z,\omega) = \int_{-\infty}^{\infty} G(k,\omega) g(k) \exp(ikz) \frac{dk}{2\pi}, \tag{3.23}$$

$F(z,\omega)$ is analytic in a region as shown in Fig. 3.2 since σ is chosen to extend the path above all the singularities. Since source is bounded between $-a$ and a, the response outside the region has to be in terms of normal modes of the system. The roots of the dispersion relation $D(\omega,k)=0$ represent poles in the Green function $G(k,\omega)$ since $G(k,\omega) \propto 1/D(k,\omega)$. Since $g(k)\exp(ikz) \to 0$ as $k \to i\infty$ for $z > a$, it is possible to close a Fourier contour above. Using the residue theorem,

$$F(z,\omega) = \oint_C G(k,\omega) g(k) \exp(ikz) \frac{dk}{2\pi} = 2\pi i \sum_{n_+} \text{Res} \frac{g(k)}{G^{-1}(k,\omega)} \tag{3.24}$$

we can then take the limit as $k \to k_{n_p}$. Furthermore, we can take the derivative of $G^{-1}(k,\omega)$ with respect to k, to obtain the residues.

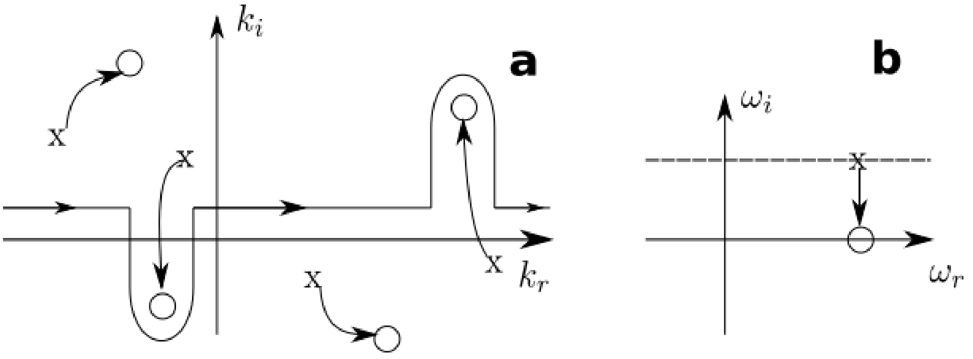

Figure 3.3: (**a**) contour C for the continuation of the motion of the poles of $G(\omega,k)$. (**b**) Movement of the Laplace contour resulting in the motion of the poles in $G(\omega,k)$

Finally, $F(z,\omega)$ can be expressed as:

$$F(z,\omega) = \sum_{n_p} \frac{ig[k_{n_p}(\omega)]}{[\partial_k G^{-1}(k,\omega)]_{k=k_{n_p}}} e^{ik_{n_p}z}. \tag{3.25}$$

The sum is over the roots of the dispersion relation which lie in the upper half k-plane for some frequency ω lying on the Laplace contour as shown in Fig. 3.3.

It is advantageous to deform the contour by varying the imaginary part of ω, ω_i, while keeping the real part fixed. Then, the poles of the dispersion relation will describe trajectories in the k-plane. If these poles cross the real $k-$axis, the analytic continuation of $F(z, \omega)$ has to be defined in terms of:

$$\tilde{F}(z, \omega) = \int_C G(k, \omega) g(k) e^{ikz} \frac{dk}{2\pi}, \tag{3.26}$$

the contour C is deformed ensuring that all poles that were below the contour remain below and the poles originally above stay above. This translates that the sum of eqn. (3.25) is over the roots that were originally above the real k-axis when $\omega_i = \sigma$. If

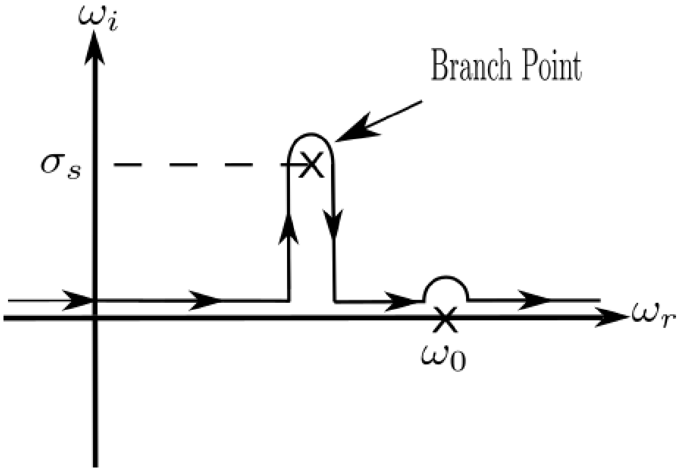

Figure 3.4: Laplace contour with an absolute instability

there are two poles that merge, one coming from below and the other from above, the contour C can no longer pass between the poles. This corresponds to a *saddle point* of the dispersion relation so that $d_k\omega = 0$ at $\omega = \omega_s$. Since $G^{-1}(\omega, k) \propto D(\omega, k) = 0$, we can use the chain rule to obtain:

$$\frac{dD}{dk} = \left(\frac{dD}{d\omega}\right)\frac{d\omega}{dk} + \frac{\partial D}{\partial k} = 0, \tag{3.27}$$

which leads to

$$\frac{\partial D}{\partial k} = 0. \tag{3.28}$$

Hence, the inverse Green's function can then be expanded about the saddle point to obtain:

$$G^{-1}(k,\omega) \simeq \left.\frac{\partial G^{-1}}{\partial \omega}\right|_{\omega_s}(\omega-\omega_s) + \frac{1}{2}\left.\frac{\partial^2 G^{-1}}{\partial k^2}\right|_{k_s}(k-k_s)^2. \tag{3.29}$$

Hence, substituting into Eqn. (3.25) we obtain

$$\tilde{F}(z,\omega) = \pm\frac{ig(k)e^{ikz}}{\partial_k\left(\partial_\omega G^{-1}\big|_{\omega_s}(\omega-\omega_s) + \frac{1}{2}\partial_k^2 G^{-1}\big|_{k_s}(k-k_s)^2\right)}. \tag{3.30}$$

Knowing that $\partial_k G^{-1} = 0$, we can solve for k. Focussing on the denominator we can find:

$$\partial_\omega G^{-1}\big|_{\omega_s}(\omega-\omega_s) = -\frac{1}{2}\partial_k^2 G^{-1}\big|_{k_s}(k-k_s)^2, \tag{3.31}$$

$$k_\pm = k_s \pm \frac{ip}{q}\sqrt{\omega-\omega_s}, \tag{3.32}$$

where the subscript ± is for $z > a$ and $z < -a$ respectively and where

$$p^2 = \partial_\omega G^{-1}\big|_{\omega_s},$$

$$q^2 = \frac{1}{2}\partial_k^2 G^{-1}\big|_{k_s},$$

Then, Eqn. (3.30) takes the form:

$$\tilde{F}(z,\omega) = \pm \frac{ig(k_\pm)e^{ik_\pm z}}{q^2(k_\pm - k_\mp)} \simeq \frac{g(k_s)e^{ik_s z}}{2pq\sqrt{\omega - \omega_s}}. \tag{3.33}$$

From Eqn. (3.33) we note there is a branch point at $\omega = \omega_s$. The entire upper half $\omega-$plane has to be explored for the largest singularity since it will yield the fastest growing mode and will dominate above other singularities. The time asymptotic response is evaluated as:

$$\psi(z,t) \simeq \frac{g(k_s)f(\omega_s)e^{i(k_s z\ -\omega_s t)}}{pq} \int_{-\infty}^{\infty} \frac{e^{i(\omega_s - \omega)t}}{\sqrt{\omega - \omega_s}} \frac{d\omega}{2\pi},$$

$$\psi(z,t) \simeq \frac{g(k_s)f(\omega_s)e^{i(k_s z - \omega_s t)}}{2pq\sqrt{\pi i t}}. \tag{3.34}$$

The absolute instability is characterized by the positive imaginary part of ω_s corresponding to temporal growth everywhere.

3.3.1 Two-stream instability

The two-stream instability (TSI) was first observed by Bohm and Gross when they presented a kinetic theory of unstable perturbations along the direction of propagation [46]. The instability occurs for counterstreaming particle beams interacting with each other. The small perturbations within each particle beam lead to out-of-phase oscillations parallel to the direction of propagation which can drive strong oscillations and ultimately yield particle bunching [1, 4, 44] which can also be observed as phase space holes [4]. The energy from the particles that are bunched up is dissipated into the plasma waves [1]. Because the affected wave vector is parallel to the electric field, this instability is electrostatic [1]. The two-stream instability gathered attention in early experiments in gas discharged fluctuations [4] and has also been studied in the quantum regime [59, 60].

Dispersion Relation

As an illustrative example, we consider two counterstreaming, non relativistic, homogeneous electron beams. The beams are propagating as $\bar{\boldsymbol{u}}_1 = -\bar{\boldsymbol{u}}_2 = u_0\hat{e}_z$ and have the same equilibrium electron number density n_0, where $\bar{n}_1 = \bar{n}_2 = n_0$. To satisfy quasineutrality, the ion density is equal to the addition of both electron species. Since we assume a harmonic perturbation, we can substitute $\nabla = ik\hat{e}_z, \partial_t = -i\omega$. We can obtain an expression for the velocity perturbation from the momentum equation:

$$\tilde{\boldsymbol{u}}_j = -\frac{e}{m_e\Omega_j}\tilde{\boldsymbol{E}}, \tag{3.35}$$

where $\Omega_j = \omega - \bar{\boldsymbol{u}}_j \cdot \boldsymbol{k}$. Substituting Eqn. (3.35) into the Eqn. (3.1) and then substituting into Eqn. (3.3) (with a little bit of elimination and algebra) yields the dispersion relation:

$$1 - \omega_p^2 \left[\frac{1}{\Omega_1^2} + \frac{1}{\Omega_2^2}\right] = 0 \tag{3.36}$$

presents poles at $\omega = \pm ku$, for the region $-ku < \omega < ku$.

Growth Rates

From the dispersion relation (3.36) one can derive the growth rate as the positive imaginary part of the frequency. The equation is of fourth order in ω. However, for the chosen symmetric case, it is quadratic in ω^2, with a positive and a negative root, yielding respectively real and purely imaginary solutions for the frequency. The imaginary frequencies correspond to a purely growing and a decaying mode. The unstable mode is given by:

$$\Gamma_{\text{TSI}} = \left[\left(\mathcal{A}^2 - k^4u^4 + 2k^2u^2\omega_p^2\right)^{1/2} - \mathcal{A}\right]^{1/2}, \tag{3.37}$$

where $\mathcal{A} = 2\omega_p^2 + 2k^2u^2$. It can be immediately observed that the instability will be present as long as the term $uk < \sqrt{2}\omega_p$.

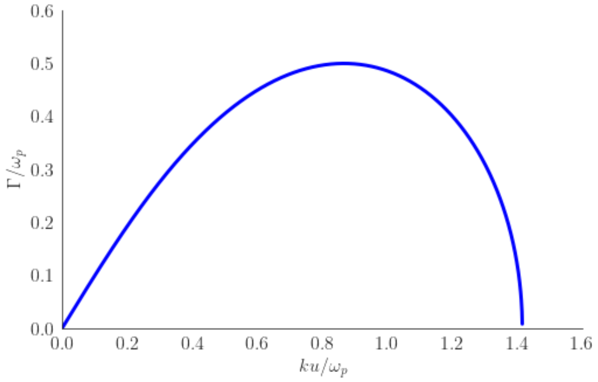

Figure 3.5: Growth rate of the two-stream instability

The growth rate of the two-stream instability is shown in Fig. 3.5. The two-stream instability has a finite range of wavenumbers and has a maximum growth rate.

3.3.2 Current filamentation instability

Waves transverse to the propagation direction can also be susceptible to unstable growth [4]. Weibel in his seminal paper demonstrated that modulations can grow perpendicular to the direction of propagation due to thermal anisotropies [61]. Later, Fried expanded from Weibel's paper using the analogy of momentum anisotropies that can be understood as two counterstreaming beams [62]. As the particle populations overlap, the particles of both species interact via their corresponding microscopic currents. Comoving particles will attract, whilst repelling the counter-streaming particles. The magnetic field then grows due to the rearrangement of the counterstreaming particles and will confine the electrons into filaments by pinching them. This is known as magnetic trapping [4, 63].

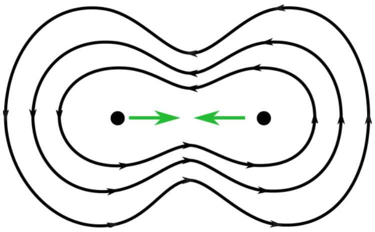

Figure 3.6: Cartoon demonstrating two co-moving particles and their magnetic field lines. The green lines represent their direction of propagation which they are attracting to each other.

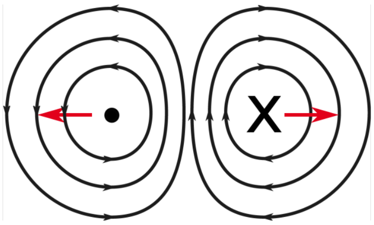

Figure 3.7: Cartoon demonstrating two counter-streaming particles and their magnetic field lines. The red arrows demonstrate the direction of propagation which they are repelling to each other.

Figure 3.6 and Fig. 3.7 show how would particles either attract or repel each other. This feedback loop is perpetuated as long as the two species overlap and interact with each other. In literature, the Weibel and CFI terms are used almost interchangeably [4]. There are occasions that “pure” Weibel modes can couple to the current filamentation modes [64]. In comparison with the TSI, for particle beams with similar densities and mildly relativistic speeds the CFI has larger growth rates [4]. Bret *et al.* [4] mention that the the CFI has been subject to a considerable research due to its ubiquity in novel laboratory experiments such as ICF and space plasma [4].

Dispersion relation

Similarily to the TSI, the CFI dispersion relation and ultimately the growth rates, can be obtained with a similar approach, where the two electron populations counter propagate with $\bar{\boldsymbol{u}}_1 = -\bar{\boldsymbol{u}}_2 = u_0\hat{e}_z$. We follow from the same assumptions as in the previous subsection, but here we investigate wave vectors transverse to the direction of propagation $\boldsymbol{k} \perp \boldsymbol{u}$; we shall use $k_y\hat{e}_y$. The momentum equation in this case encompasses the perturbed magnetic field, and takes the following form:

$$\tilde{\boldsymbol{u}}_j = -\frac{ie}{m_e\omega}\left(\tilde{\boldsymbol{E}} + \frac{\bar{\boldsymbol{u}}_j}{\omega} \times \left(\boldsymbol{k} \times \tilde{\boldsymbol{E}}\right)\right). \tag{3.38}$$

Eqn. (3.38), can be substituted into the continuity equation. After solving the continuity equation for the number density perturbation, one finds an expression for the current density $\tilde{\boldsymbol{J}} = -e\sum_j \left(\bar{\boldsymbol{u}}_j\tilde{n}_j + n_0\tilde{\boldsymbol{u}}_j\right)$, so it can be substituted into Maxwell-Ampere's equation to yield:

$$k^2\tilde{\boldsymbol{E}} - k^2\tilde{E}_y\hat{e}_y = \frac{\omega^2}{c^2}\tilde{\boldsymbol{E}} - 2\frac{\omega_p^2}{c^2}\left[\frac{k^2u^2}{\omega^2}\tilde{E}_z\hat{e}_z + \tilde{\boldsymbol{E}}\right]. \tag{3.39}$$

One can immediately recognize that Eqn. (3.39) can lead to different solutions depending on the direction of the electric field. By choosing E parallel to $\hat{e}_x$

$$\omega^2 = c^2k^2 + 2\omega_p^2 \tag{3.40}$$

which is the usual dispersion relation of plasma oscillations. The factor of 2 in front of the plasma frequency in the equation above corresponds to two electron populations.

For $\boldsymbol{E} \parallel \hat{e}_z$ we obtain:

$$\omega^2 = k^2c^2 + 2\omega_p^2\left(1 + \frac{k^2u^2}{\omega^2}\right). \tag{3.41}$$

This is the dispersion relation for the CFI.

Growth rate

Similar to the TSI dispersion, it is quadratic in ω^2, with two real solutions, one of which is negative. This implies a positive imaginary root for the frequency corresponding to the instability. The growth rate is then:

$$\Gamma_{\text{cfi}} = \left[\left(A^2/4 + 2k^2u^2\omega_p^2\right)^{1/2} - A/2\right]^{1/2}, \tag{3.42}$$

where $A = 2\omega_p^2 + c^2k^2$. According to Eqn. (3.42), the CFI exists for a seemingly infinite range of wavenumbers with a large growth rate that implies, compared with the TSI, that CFI should be more common because it is rather unstable "infinite" range of wavenumbers as seen in Fig. 3.8. However, this infinite range is unphysical. Thermal effects limit the range of wavenumbers that yield the instability and can suppress the

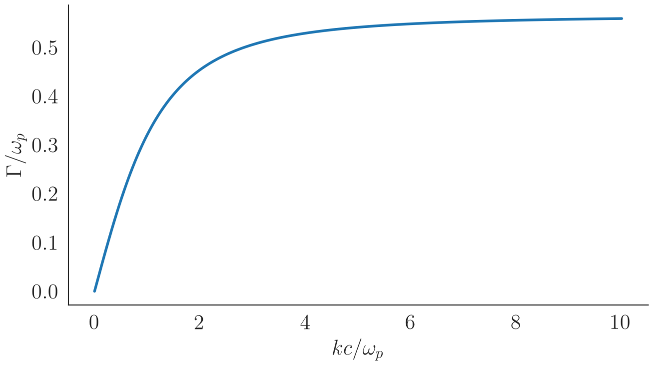

Figure 3.8: Growth rate for the current filamentation instability for $u = 0.4c$

growth rates [65].

3.3.3 Oblique instabilities

Since wave vectors are not limited to be either parallel or perpendicular to the direction of propagation, oblique modes are also possible [4, 54, 55]. Oblique modes are also known as two-stream/filamentation (TSF) branches since they combine elements of both the TSI and CFI [4]. It has been pointed out that coupling between the TSI and CFI should be analysed [4, 56]. Oblique modes have been found to dominate in the case of cold and diluted relativistic electron beams [66]. Analyzing the oblique angles yields several advantages over restricting to certain wave vector direction. Studying oblique wave vectors can yield a robust description of the unstable modes over all $\boldsymbol{k}$ space [56, 66]. Different initial conditions of the plasma can lead to different dominating modes [55]. Magnetization of the plasma can also lead to regions where the TSI can dominate in a larger range over CFI and TSFI modes [55].

To generalise the preceding description we choose a wave vector oblique to the streaming velocities (which remain along $\hat{e}_z$), $\boldsymbol{k} = k_y\hat{e}_y + k_z\hat{e}_z$ i.e., $\nabla \rightarrow i\boldsymbol{k}$. The continuity and momentum equations then take the following form:

$$\tilde{n}_j = \frac{n_0}{\Omega_j}\boldsymbol{k}\cdot\tilde{\boldsymbol{u}}_j, \tag{3.43}$$

$$\tilde{\boldsymbol{u}}_j = -\frac{ie}{m_e\Omega_j}\left[\tilde{\boldsymbol{E}} + \bar{\boldsymbol{u}}_j \times \left(\boldsymbol{k}\times\tilde{\boldsymbol{E}}\right)/\omega\right], \tag{3.44}$$

where we have used that $\tilde{\boldsymbol{B}} = \boldsymbol{k} \times \tilde{\boldsymbol{E}}/\omega$. We can factor out the perturbed electric field from Eq. 3.44 following the steps:

$$\tilde{\boldsymbol{u}}_j = -\frac{ie}{m_e\Omega_j}\left[\tilde{\boldsymbol{E}} + \frac{\boldsymbol{k}}{\omega}(\boldsymbol{u}_j \cdot \tilde{\boldsymbol{E}}) - \frac{\tilde{\boldsymbol{E}}}{\omega}(\boldsymbol{u} \cdot \boldsymbol{k})\right], \tag{3.45}$$

$$\tilde{\boldsymbol{u}}_j = -\frac{ie}{m_e\Omega_j}\left[\left(1 - \frac{\boldsymbol{u}_j \cdot \boldsymbol{k}}{\omega}\right)\tilde{\boldsymbol{E}} + \frac{\boldsymbol{k}}{\omega}(\boldsymbol{u}_j \cdot \tilde{\boldsymbol{E}})\right]. \tag{3.46}$$

We can multiply Ω_j and factor out ω:

$$\tilde{\boldsymbol{u}}_j = -\frac{ie}{m_e\omega}\left[\frac{1}{\Omega_j}\left(\omega - \boldsymbol{u}_j \cdot \boldsymbol{k}\right)\tilde{\boldsymbol{E}} + \frac{\boldsymbol{k}}{\Omega_j}(\boldsymbol{u}_j \cdot \tilde{\boldsymbol{E}})\right]. \tag{3.47}$$

Since $\Omega_j = \omega - \boldsymbol{u}_j \cdot \boldsymbol{k}$ it will divide out with the first in the r.h.s, and then we can factor out $\tilde{\boldsymbol{E}}$:

$$\tilde{\boldsymbol{u}}_j = -\frac{ie}{m_e\omega}\left[\tilde{\boldsymbol{E}} + \frac{\boldsymbol{k}}{\Omega_j}(\boldsymbol{u}_j \cdot \tilde{\boldsymbol{E}})\right], \tag{3.48}$$

$$\tilde{\boldsymbol{u}}_j = -\frac{ie}{m_e\omega}\left[\underline{\mathbf{1}} + \frac{\boldsymbol{k} \otimes \boldsymbol{u}_j}{\Omega_j}\right] \cdot \tilde{\boldsymbol{E}}. \tag{3.49}$$

Substituting Eq. 3.49 into Eq. 3.43 one obtains:

$$\tilde{n}_j = -\frac{n_0}{\Omega_j}\boldsymbol{k} \cdot \left\{\frac{ie\omega}{m_e}\left[\underline{\mathbf{1}} + \frac{\boldsymbol{k} \otimes \boldsymbol{u}_j}{\Omega_j}\right] \cdot \tilde{\boldsymbol{E}}\right\} \tag{3.50}$$

Replacing the perturbed density and velocity into the current density and following the same steps as in the previous subsections, the conductivity tensor now takes the following form:

$$\underline{\boldsymbol{\sigma}} = \sum_j \frac{i\omega_p^2\epsilon_0}{\omega}\left(\underline{\mathbf{1}} + \frac{\boldsymbol{u}_j \otimes \boldsymbol{k}}{\Omega_j}\right) \cdot \left(\underline{\mathbf{1}} + \frac{\boldsymbol{k} \otimes \boldsymbol{u}_j}{\Omega_j}\right). \tag{3.51}$$

We can express the equation ultimately as in Eqn. (3.16) and obtain the dispersion relation by obtaining the determinant of the matrix $\underline{\boldsymbol{\chi}}$. By adding the contributions for both particles populations, we can build the dielectric tensor:

$$\underline{\boldsymbol{\epsilon}} = \epsilon_0(\underline{\boldsymbol{I}} + i\underline{\boldsymbol{\sigma}}/(\epsilon_0\omega)), \tag{3.52}$$

with the components of $\underline{\boldsymbol{\sigma}}$ being:

$$\begin{aligned}
\sigma_{xx} = \sigma_{yy} &= \frac{2i\omega_p^2\epsilon_0}{\omega}, \\
\sigma_{yz} = \sigma_{zy} &= \frac{ik_y u_0 \omega_p^2 \epsilon_0}{\omega}\left(\frac{1}{\Omega_1} - \frac{1}{\Omega_2}\right), \\
\sigma_{zz} &= \frac{i\omega_p^2\epsilon_0}{\omega}\left[2 + 2uk_z\left(\frac{1}{\Omega_1} - \frac{1}{\Omega_2}\right) + u^2k^2\left(\frac{1}{\Omega_1^2} + \frac{1}{\Omega_2^2}\right)\right].
\end{aligned}$$

When substituting into the secular equation the determinant factorises

$$\det(\chi) = 0. \tag{3.53}$$

One factor yields the dispersion relation for a transverse electromagnetic wave in a plasma

$$(k_y^2 + k_z^2) - \omega^2\mu_0\epsilon_{xx} = 0, \tag{3.54}$$

while the dispersion relation we are interested in follows from:

$$\begin{vmatrix} \omega^2\mu_0\epsilon_{yy} - k_z^2 & \omega^2\mu_0\epsilon_{yz} + k_z k_y \\ \omega^2\mu_0\epsilon_{zy} + k_z k_y & \omega^2\mu_0\epsilon_{zz} - k_y^2 \end{vmatrix} = 0. \tag{3.55}$$

3.3.4 Growth Rates, Oblique Instabilites

Solving the dispersion relation (3.55) for the angular frequency, is an algebraically intensive task that yields to use of numerical codes. Using Python's library for symbolic manipulation `SymPy` [67], we can solve for an algebraic expression of the growth rates. It can be seen that the growth rate of the oblique instability tends to the CFI growth rate as $k_z \to 0$ and to the TSI growth rate as $k_y \to 0$. For wavenumbers that are not entirely perpendicular or parallel to propagation, Fig. (3.9)

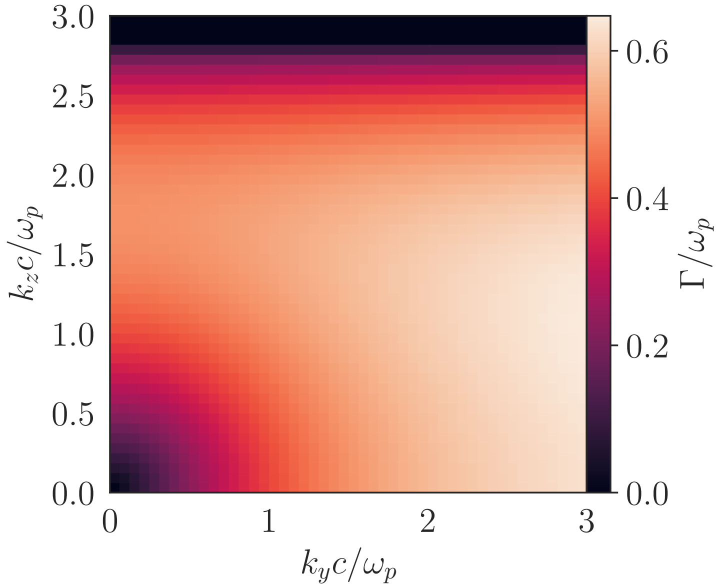

Figure 3.9: Growth rate heatmap of oblique instabilities

3.4 Streaming Instabilities in relativistic plasma

Diverging from the insightful approximation for a non-relativistic cold plasma, the need to consider relativistic effects becomes apparent for space and laboratory plasma. The inclusion of relativistic effects makes the spectrum of instabilities in plasmas richer [55, 68] and can also have a stabilizing influence [53].

3.4.1 Dispersion relations, TSI, CFI, Oblique instability

Expanding from the previous section, we now account for relativistic mean velocities ($\bar{u}/c \approx 1$) and the Lorentz factor $\gamma = (1-\beta^2)^{-1/2}$, where $\beta = \bar{u}/c$. To derive the dispersion relations and ultimately the growth rates of the TSI and CFI, the steps are mostly the same, except when solving for the velocity perturbation where $\tilde{\boldsymbol{p}}_j = \gamma m_e \tilde{\boldsymbol{u}}_j + \tilde{\gamma} m_e \bar{\boldsymbol{u}}_j$. The momentum equation for arbitrary wave vectors is:

$$(-i\omega + i\bar{\boldsymbol{u}} \cdot \boldsymbol{k}) \cdot \tilde{\boldsymbol{p}}_j = -e\left(\tilde{\boldsymbol{E}} + \bar{\boldsymbol{u}} \times \tilde{\boldsymbol{B}}\right). \tag{3.56}$$

In the equation above, $\tilde{\boldsymbol{p}}_j = \bar{\gamma} m_e \tilde{\boldsymbol{u}}_j + \tilde{\gamma} m_e \bar{\boldsymbol{u}}_j$. We can obtain $\tilde{\gamma} \approx \bar{\gamma}^3 \tilde{\boldsymbol{u}}_j \cdot \bar{\boldsymbol{u}}_j / c^2$ and follow the derivation:

$$(-i\omega + i\bar{\boldsymbol{u}} \cdot \boldsymbol{k}) \cdot \left(\bar{\gamma} m_e \tilde{\boldsymbol{u}}_j + \frac{m_e \bar{\gamma}^3 \tilde{\boldsymbol{u}}_j \cdot \bar{\boldsymbol{u}}_j}{c^2} \bar{\boldsymbol{u}}_j\right) = -e\left(\tilde{\boldsymbol{E}} + \bar{\boldsymbol{u}} \times \tilde{\boldsymbol{B}}\right), \tag{3.57}$$

$$\Omega_j m_e \left(\bar{\gamma} \tilde{\boldsymbol{u}}_j + \frac{\bar{\gamma}^3 \tilde{\boldsymbol{u}}_j \cdot \bar{\boldsymbol{u}}_j}{c^2} \bar{\boldsymbol{u}}_j\right) = -ie\left(\tilde{\boldsymbol{E}} + \bar{\boldsymbol{u}}_j \times (\boldsymbol{k} \times \tilde{\boldsymbol{E}})/\omega\right), \tag{3.58}$$

where we can factor out the perturbed velocity from the inner product as: $(\tilde{\boldsymbol{u}}_j \cdot \bar{\boldsymbol{u}}_j)\bar{\boldsymbol{u}}_j = (\bar{\boldsymbol{u}}_j \otimes \bar{\boldsymbol{u}}_j)\tilde{\boldsymbol{u}}_j$ and obtain the momentum equation with relativistic effects:

$$\left(\bar{\gamma}\underline{\mathbf{1}} + \frac{\bar{\gamma}^3}{c^2}\bar{\boldsymbol{u}}_j \otimes \bar{\boldsymbol{u}}_j\right) \cdot \tilde{\boldsymbol{u}}_j = -\frac{ie}{m_e \Omega_j}\left(\tilde{\boldsymbol{E}} + \bar{\boldsymbol{u}}_j \times (\boldsymbol{k} \times \tilde{\boldsymbol{E}})/\omega\right). \tag{3.59}$$

Whilst solving for the TSI dispersion relations, the term multiplying the velocity perturbation can be approximated as $\approx \bar{\gamma}^3$. Then, Eqn. (3.59) takes the form:

$$\tilde{u}_j = -\frac{ie}{\bar{\gamma}^3 m_e \Omega_j}\tilde{\boldsymbol{E}}. \tag{3.60}$$

We can then substitute into eqn. (3.3) where then, relativistically corrected dispersion relation for the TSI takes the familiar form:

$$1 - \frac{\omega_p^2}{\bar{\gamma}^3}\left[\frac{1}{\Omega_1^2} + \frac{1}{\Omega_2^2}\right] = 0. \tag{3.61}$$

The growth rates are obtained similarly as in the previous section. The growth rate with the relativistic correction for the TSI is then:

$$\Gamma_{\mathrm{TSI}} = \left[\left(\mathcal{B}^2 - k^4u^4 + 2\omega_p^2 k^2 u^2/\bar{\gamma}^3\right)^{1/2} - \mathcal{B}\right]^{1/2}, \tag{3.62}$$

where $\mathcal{B} = (\omega_p^2/\bar{\gamma}^3 + u^2k^2)$. To obtain the dispersion relation for the CFI, we use $\boldsymbol{k} = k_y\hat{e}_y$ which is perpendicular to the direction of propagation. Then, eqn. (3.59) can take the following forms depending on its direction:

$$\tilde{u}_{j,y} = -\frac{ie}{\bar{\gamma} m_e \Omega_j}\left(\tilde{E}_y + \frac{\bar{u}_j k_y}{\omega}\tilde{E}_z\right), \tag{3.63}$$

$$\tilde{u}_{j,z} = -\frac{ie}{\bar{\gamma}^3 m_e}\tilde{E}_z. \tag{3.64}$$

And inserting eqn. (3.64) into the current density and adding the contributions of both electron species we obtain:

$$\tilde{\boldsymbol{J}} = 2\frac{i\bar{n}e^2}{m_e\bar{\gamma}^3\omega}\tilde{E}_z + 2\frac{i\bar{n}e^2\bar{u}^2 k_y^2}{\omega^3\bar{\gamma}}\tilde{E}_z. \tag{3.65}$$

We use Eqn. (3.65) and substitute into Eqn. (3.6). With a little algebra and dividing both side by $\tilde{E}_z$, we obtain the expression for the dispersion relation of the CFI with relativistic corrections

$$\omega^2 = k^2c^2 + 2\omega_p^2\left(\frac{1}{\bar{\gamma}^3} + \frac{\bar{u}^2k^2}{\omega^2\bar{\gamma}}\right). \tag{3.66}$$

Similarly, we can obtain the growth rate of the instability by solving for ω.

$$\Gamma_{\text{CFI}} = \left(\sqrt{\mathcal{C}^2/4 + 2\omega_p^2k^2\bar{u}^2/\gamma} - \mathcal{C}/2\right)^{1/2}, \tag{3.67}$$

where $\mathcal{C} = c^2k^2 + 2\omega_p^2/\bar{\gamma}^3$. We can see that the relativistic terms have a direct impact on the growth rate of the instabilities. It can be inferred that the faster the particles are, the smaller the growth rate is.

As observed in Fig. 3.5, the growth rate for the TSI has a similar dependence to the cold, non-relativistic case, where for increasing k, it rises to a maximum and then

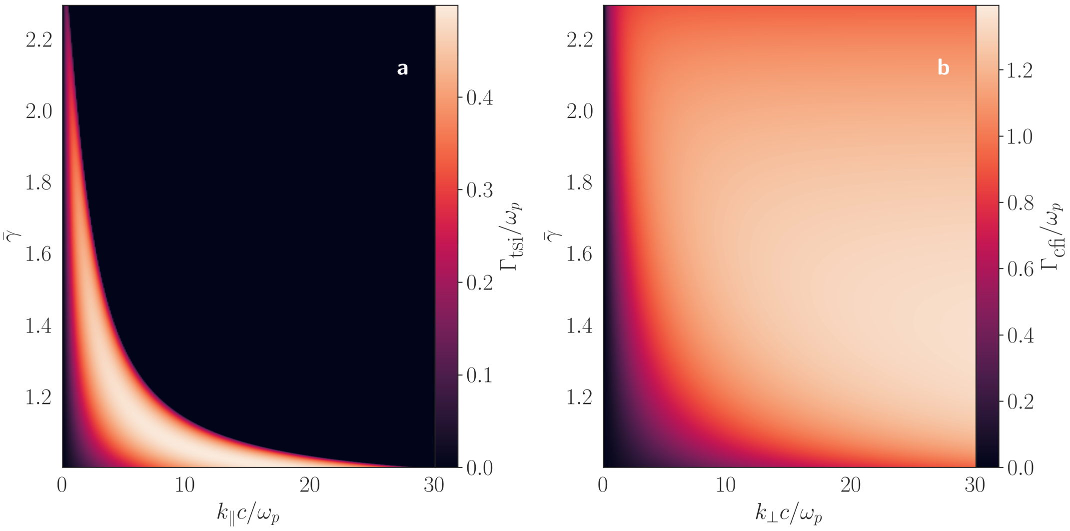

Figure 3.10: Growth rate for the two-stream instability (**a**) and the current filamentation instability (**b**) as a function of k and $\bar{\gamma}$.

disappears. However, the relativistic effects reduces the k range and decreases the maximum growth rate impact the instability growth rate as higher velocities. For the CFI, the growth rates continue increasing similarily as in the non-relativistic approach, and demonstrate a "plateau", where the relativistic effects have not decreased the growth rate. As the velocity increases, the inverse proportionality to the Lorentz factor has a considerable effect and decreases the growth rates.

As for the case of arbitrarily oriented wave numbers, we can also derive its dispersion relation. Following from Eqn. (3.59), by solving for $\tilde{\boldsymbol{u}}_j$:

$$\tilde{\boldsymbol{u}}_j = \frac{-ie}{\bar{\gamma} m \omega} \left(\underline{\mathbf{1}} - \frac{\boldsymbol{u}_j \otimes \boldsymbol{u}_j}{c^2} \right) \cdot \left(\underline{\mathbf{1}} + \frac{\boldsymbol{k} \otimes \boldsymbol{u}_j}{\Omega_j} \right) \cdot \tilde{\boldsymbol{E}} \tag{3.68}$$

We then substitute into the perturbed number density, Eq. 3.43:

$$\tilde{n}_j = \frac{n_0}{\Omega_j}\boldsymbol{k}\cdot\left\{\frac{-ie}{\bar{\gamma}m\omega}\left(\underline{\mathbf{1}} - \frac{\boldsymbol{u}_j\otimes\boldsymbol{u}_j}{c^2}\right)\cdot\left(\underline{\mathbf{1}} + \frac{\boldsymbol{k}\otimes\boldsymbol{u}_j}{\Omega_j}\right)\cdot\tilde{\boldsymbol{E}}\right\} \tag{3.69}$$

and we then can substitute both into the current density and build up the dielectric tensor from:

$$\underline{\boldsymbol{\sigma}}_j = i\frac{\omega_p^2\epsilon_0}{\bar{\gamma}\omega}\left(\underline{\mathbf{1}} + \frac{\boldsymbol{u}_j\otimes\boldsymbol{k}}{\Omega_j}\right)\cdot\left(\underline{\mathbf{1}} + \frac{\boldsymbol{K}_j\otimes\boldsymbol{u}_j}{\Omega_j}\right), \tag{3.70}$$

where $\boldsymbol{K}_j = \boldsymbol{k} - \boldsymbol{u}_j\omega/c^2$. By taking the dot product of the two terms in backets of Eqn. (3.70) and replacing $\underline{\boldsymbol{\sigma}}$ into the dielectric tensor, we can get an equation of the form (3.16), we can obtain the entries for the tensor $\underline{\boldsymbol{\chi}}$.

$$\underline{\boldsymbol{\chi}} = \begin{pmatrix} \omega^2\mu_0\epsilon_{xx} - (k_y^2 + k_z^2) & 0 & 0 \\ 0 & \omega^2\mu_0\epsilon_{yy} - k_z^2 & \omega^2\mu_0\epsilon_{yz} + k_zk_y \\ 0 & \omega^2\mu_0\epsilon_{zy} + k_zk_y & \omega^2\mu_0\epsilon_{zz} - k_y^2 \end{pmatrix}, \tag{3.71}$$

with

$$\begin{aligned}
\epsilon_{xx} &= \epsilon_{yy} = \epsilon_0 - \epsilon_0\frac{2\omega_p^2}{\bar{\gamma}\omega^2}, \\
\epsilon_{yz} &= \epsilon_{zy} = -\epsilon_0\frac{k_yu_0\omega_p^2}{\bar{\gamma}\omega^2}\left(\frac{1}{\Omega_1} - \frac{1}{\Omega_2}\right), \\
\epsilon_{zz} &= \epsilon_0 - \epsilon_0\frac{\omega_p^2}{\bar{\gamma}\omega^2}\left[2 + 2uk_z\left(\frac{1}{\Omega_1} - \frac{1}{\Omega_2}\right) + u^2(k^2 + \frac{\omega^2}{c^2})\left(\frac{1}{\Omega_1^2} + \frac{1}{\Omega_2^2}\right)\right].
\end{aligned}$$

the dispersion relation is obtained from the secular equation (3.53). The growth rates are obtained similarly to the previous section using SymPy.

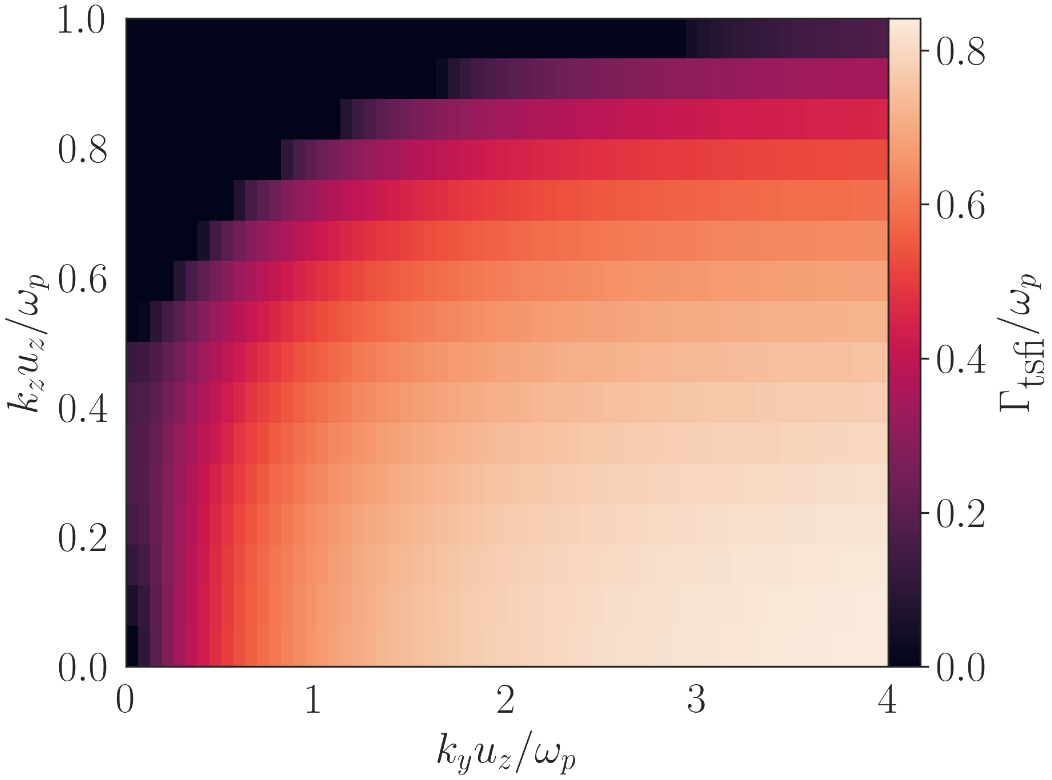

Figure 3.11: Growth rates for the TSFI modes for $\bar{\gamma} = 2$

Fig. 3.11 shows that current filamentation modes are dominant in weakly relativistic velocities.

3.5 Thermal effects on streaming instabilities

In this chapter, we have been focusing mostly on cold plasma, neglecting the pressure term in the momentum equation. Finite plasma temperature can have an array of different effects on the instabilities: it can increase the growth rate of an instability due to cumulative effects of two istabilities [50], lead to the development of new instabilities like the Weibel instability [61], or suppress instabilities [65]. Kinetic effects can be considered using the Vlasov-Maxwell equations [1]. We can still, however, use the fluid approach to investigate plasma if the momentum distribution can be approximated using the lowest order moments. The fluid description can miss kinetic effects that could be described by the Vlasov-Maxwell description. A covariant theory of warm plasma using an invariant measure of thermal momentum spread can be found in Refs. [51, 69, 70, 71].

For an estimate of the effects of finite plasma temperature on the instabilities we approximate the distribution and hence the pressure as isotropic in the laboratory frame. The pressure term on the right hand side of Eqn. (3.2) can be approximated assuming an adiabatic equation of state, as $\tilde{P}_j = 3\tilde{n}_j k_B T$. Substituting for $\tilde{n}_j$ using the continuity equation, the momentum equation then takes the following shape:

$$\tilde{\boldsymbol{u}}_j = -\frac{ie}{m_e \Omega_j}\left(\tilde{\boldsymbol{E}} + \bar{\boldsymbol{u}}_j \times (\boldsymbol{k} \times \tilde{\boldsymbol{E}})/\omega\right) + \frac{3k_B T \boldsymbol{k} \cdot \tilde{\boldsymbol{u}}_j}{m_e \Omega_j^2}\boldsymbol{k}. \tag{3.72}$$

For $\boldsymbol{E} \parallel \boldsymbol{k}$, corresponding to the TSI, the eqn. (3.72) simplifies to

$$\tilde{\boldsymbol{u}}_j = -\frac{ie}{m_e \Omega_j}\tilde{\boldsymbol{E}} + \frac{3k_B T k^2}{m_e \Omega_j^2}\tilde{\boldsymbol{u}}_j. \tag{3.73}$$

Following the same steps in deriving the dispersion relations, we obtain the TSI dispersion relation including thermal effects

$$1 = \omega_p^2 \left(\frac{1}{\Omega_1^2 - k^2 v_t^2} + \frac{1}{\Omega_2^2 - k^2 v_t^2}\right). \tag{3.74}$$

where $v_t^2 = 3k_B T/m_e$. We similarily obtain the dispersion relation for the CFI including thermal effects:

$$\omega^2 = c^2k^2 + 2\omega_p^2 \left(1 + \frac{k^2u^2}{\omega^2 - k^2v_t^2}\right). \tag{3.75}$$

Solving for the growth rates yield:

$$\Gamma_{\text{TSI}} = \left[(\mathcal{C}/4 - \mathcal{D})^{1/2} - \mathcal{C}/2\right]^{1/2}, \tag{3.76}$$

$$\Gamma_{\text{CFI}} = \left((\mathcal{E} - \mathcal{F})^{1/2}/2 - \mathcal{E}\right]^{1/2}, \tag{3.77}$$

where $\mathcal{C} = \omega_p^2 + k^2u^2 + v_t^2k^2, \mathcal{D} = -k^4(u^2 - v_t^2)^2 + k^2\omega_p^2(v_t^2 - 2u^2), \mathcal{E} = k^2c^2 + 2\omega_p^2 + k^2v_t^2, \mathcal{F} = k^2(c^2k^2v_t^2 + 2\omega_p^2(v_t^2 - u^2))$. As observed from the growth rates, the thermal velocity spread will reduce the growth in both cases. A thermal spread parallel to the direction of particle propagation can lead to growth [65]. The coupling of the CFI and Weibel modes is plausible [50, 72], this coupling can lead to both instabilities enhancing unstable growth. For a negative anisotropy, the Weibel instability does not exists and the cumulative growth is decreased [50]. The CFI and TSI growth rates illustrated in Fig. 3.12 as frame (**a**) and (**b**) respectively. The heatmaps in Fig. 3.12, (**b**) the range of wavenumbers yielding unstable growth drastically decreases as the temperature is increased.

Naturally, oblique modes will be influenced by a finite temperature [4, 73]. The finite temperature can yield a dominating branch with properties closer to the TSI than the CFI [73]. However, an anisotropic thermal distribution can have different effects depending the direction of the anisotropy [73]; a thermal anisotropy perpendicular to

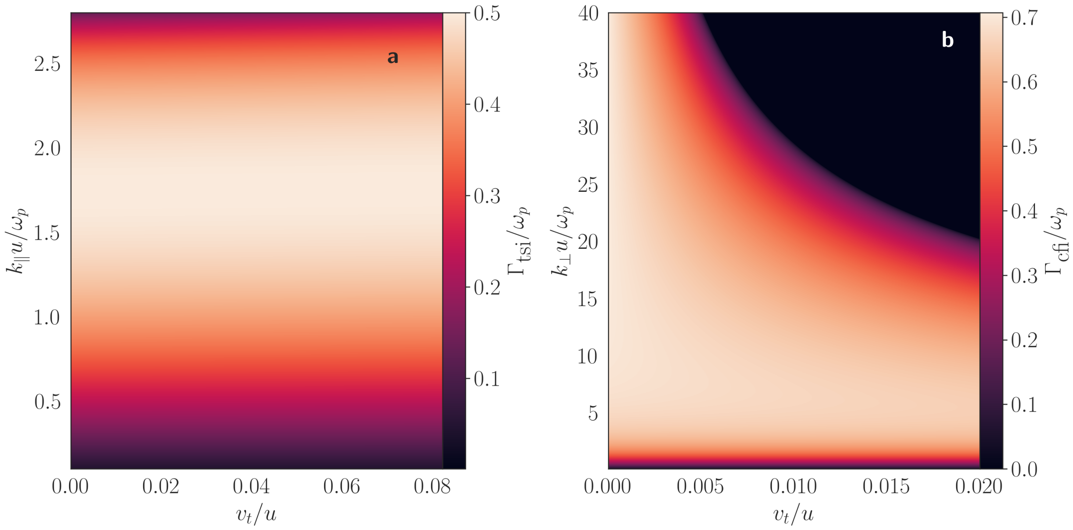

Figure 3.12: Growth rate for (**a**) the two-stream instability and (**b**) the current filamentation instability as a function of k and v_t.

propagation can diminish the CFI growth rates whilst in thermal anisotropy parallel to the propagation can yield a coupling with "pure" Weibel modes [65]. The derivation for the dispersion relation for arbitrary (excluding Weibel) modes follows from Eqn. (3.1). We can adapt it to this analysis and find:

$$\underline{\boldsymbol{\nu}}_j \cdot \tilde{\boldsymbol{u}}_j = -\frac{ie}{m_e\omega}\left(\underline{\boldsymbol{1}} + \frac{\boldsymbol{k}\otimes\bar{\boldsymbol{u}}_j}{\Omega_j}\right)\tilde{\boldsymbol{E}}, \tag{3.78}$$

where $\underline{\boldsymbol{\nu}}_j = \underline{\boldsymbol{1}} - v_t^2\boldsymbol{k}\otimes\boldsymbol{k}/\Omega_j^2$. The perturbed velocity is obtained by multiplying with the inverse of the tensor. The inverse of $\underline{\boldsymbol{\nu}}$ is:

$$\underline{\boldsymbol{\nu}}_j^{-1} = \begin{pmatrix} 1 & 0 & 0 \\ 0 & \frac{1-k_z^2V_j^2}{1-k^2V_j^2} & \frac{k_yk_zV_j^2}{1-k^2V_j^2} \\ 0 & \frac{k_yk_zV_j^2}{1-k^2V_j^2} & \frac{1-k_y^2}{1-k^2V_j^2} \end{pmatrix}, \tag{3.79}$$

with $k^2 = k_y^2 + k_z^2$ and $V_j^2 = v_t^2/\Omega_j^2$. For $T = 0$, one has $\underline{\boldsymbol{\nu}}_j^{-1} = \underline{\mathbf{1}}$. Furthermore, we can assemble the conductivity tensor, which will have the form:

$$\underline{\boldsymbol{\sigma}}_j = \frac{i\omega_p^2\epsilon_0}{\omega}\left(\underline{\mathbf{1}} + \frac{\bar{\boldsymbol{u}}_j \otimes \boldsymbol{k}}{\Omega_j}\right)\underline{\boldsymbol{\nu}}_j^{-1} \cdot \left(\underline{\mathbf{1}} + \frac{\boldsymbol{k} \otimes \bar{\boldsymbol{u}}_j}{\Omega_j}\right). \tag{3.80}$$

Similarly, as before, the conductivity tensors for both species are added to dielectric tensor, with components:

$$\epsilon_{xx} = \epsilon_0 - \epsilon_0\frac{\omega_p^2}{\omega^2}, \tag{3.81}$$

$$\epsilon_{yy} = \epsilon_0 - \epsilon_0\frac{\omega_p^2}{\omega^2}\left(\nu_{1,yy}^{-1} + \nu_{2,yy}^{-1}\right), \tag{3.82}$$

$$\epsilon_{yz} = \epsilon_{zy} = \epsilon_0\frac{\omega_p^2}{\omega^2}\left(k_y u\left(\frac{\nu_{1,yy}^{-1}}{\Omega_1} - \frac{\nu_{2,yy}^{-1}}{\Omega_2}\right) + \nu_{1,yz}^{-1} + \nu_{2,yz}^{-1} + k_z u\left(\frac{\nu_{1,yz}^{-1}}{\Omega_1} - \frac{\nu_{2,yz}^{-1}}{\Omega_2}\right)\right), \tag{3.83}$$

$$\begin{aligned}\epsilon_{zz} = \epsilon_0 - \epsilon_0\frac{\omega_p^2}{\omega^2}&\left(u^2k_y^2\left(\frac{\nu_{yy_1}^{-1}}{\Omega_1^2} + \frac{\nu_{yy_2}^{-1}}{\Omega_2^2}\right) + u^2k_z^2\left(\frac{\nu_{zz_1}^{-1}}{\Omega_1^2} + \frac{\nu_{zz_2}^{-1}}{\Omega_2^2}\right) + 2k_yk_zu^2\left(\frac{\nu_{yz_1}^{-1}}{\Omega_1^2} + \frac{\nu_{yz_2}^{-1}}{\Omega_2^2}\right)\right) \\ - \epsilon_0\frac{\omega_p^2}{\omega^2}&\left(2k_yu\left(\frac{\nu_{yz_1}^{-1}}{\Omega_1} - \frac{\nu_{yz_2}^{-1}}{\Omega_2}\right) + 2k_zu\left(\frac{\nu_{zz_1}^{-1}}{\Omega_1} - \frac{\nu_{zz_2}^{-1}}{\Omega_2}\right) + \nu_{zz_1}^{-1} + \nu_{zz_2}^{-1}\right).\end{aligned} \tag{3.84}$$

The remaining components of the dielectric tensor are zero. By setting the temperature $T = 0$, these components reduce to those in section 3.3. Similarily as before, we need to set the determinant of the tensor χ, defined in Eqn. (3.53), equal to zero. One of the solutions, $\chi_{xx} = 0$, yields the dispersion relation of a transverse electromagnetic wave in a plasma, and the dispersion relation for oblique modes in a thermal plasma can be obtained from $(\omega^2\epsilon_{yy} - c^2k_z^2)(\omega^2\epsilon_{zz} - c^2k_y^2) - (\omega^2\epsilon_{yz} + c^2k_zk_y)(\omega^2\epsilon_{zy} + c^2k_zk_y) = 0$.

3.6 Streaming instabilities in inhomogeneous media

Plasma is not usually homogeneous [29]. Inhomogeneities in plasma are abundant, including spatially varying densities [48, 49], velocities [74], temperatures [75, 76], and magnetic fields. For the purposes of this thesis, we solely focus on inhomogeneities in the number density of plasma. Inhomogeneities in plasma have been extensively studied both theoretically [49] and experimentally [77]. In the theoretical descriptions, inhomogeneous densities have mostly been approached using a Wentzel-Kramers-Brillouin (WKB) approximation in the perturbed component [29, 49, 74, 78], which can yield a generalised dispersion relation. Other authors have used a variational method to derive the electromagnetic response of waves in plasma [79]. Assuming plasma with an inhomogeneity along $\hat{e}_x$, in the approach used in Refs. [29, 49] would have the following form:

$$\tilde{\psi} = \psi_0 \exp(i \int dx' k(x') + ik_y y + ik_z z - i\omega t). \tag{3.85}$$

The derivation of a general dispersion relation for a magnetized inhomogeneous (and to that extent, a homogeneous) plasma is an arduous task [48, 49]. In the kinetic approach, the magnetization of the plasma requires the cyclotron motion to be considered and thus the trajectories of particles must be taken into account in the derivations. The final result is a very complicated general dielectric tensor consisting of integro-differential equations due to the Vlasov-Maxwell's equations, which has to be simplified to perform a meaningful analysis [48, 49]. Here, we consider plasma with an inhomogeneous density profile in $\hat{e}_z$, $\bar{n}(z)$, and keep all the previous assumptions of a cold, non-relativistic plasma as in subsection 1.3. Using the WKB approximation, the perturbations adopt the form $\tilde{\psi}(y,z,t) = \psi_0(z)\exp(ik_y y + i\int k_z(z)dz - i\omega t)$. Since the amplitude of the perturbation depends on the inhomogeneity, we can solve this problem differently as presented in literature examples [49]. We will develop a set of coupled linear ordinary differential equations, which we solve as an eigenvalue problem. Starting from the equilibrium number density, we can observe that having an inhomogeneous density profile leads to an inhomogeneous mean velocity profile:

$$\partial_t \bar{n} + \nabla \cdot (\bar{\boldsymbol{u}}_\pm \bar{n}) = 0, \tag{3.86}$$

$$\bar{\boldsymbol{u}}_\pm \cdot \nabla \bar{n} + \bar{n} \nabla \cdot \bar{\boldsymbol{u}}_\pm = 0, \tag{3.87}$$

$$\bar{\boldsymbol{u}}_\pm \cdot \nabla \bar{n} = -\bar{n} \nabla \cdot \bar{\boldsymbol{u}}_\pm, \tag{3.88}$$

$$\frac{1}{\bar{n}} d_z \bar{n} = \frac{1}{\bar{u}_\pm} \partial_z \bar{u}_\pm. \tag{3.89}$$

We can obtain the differential equation for the perturbed number density perturbation becomes:

$$\partial_z \tilde{n}_j = \frac{i\omega - d_z \bar{u}_j}{\bar{u}_j} \tilde{n}_j - \frac{ik_y \bar{n}}{\bar{u}_j} \tilde{u}_{j,y} - \frac{\tilde{u}_{j,z}}{\bar{u}_j} d_z \bar{n} - \frac{\bar{n}}{\bar{u}_j} \partial_z \tilde{u}_{j,z}. \tag{3.90}$$

From Faraday's law we obtain:

$$\partial_z \tilde{E}_y = -i\omega \tilde{B}_x + ik_y \tilde{E}_z \tag{3.91}$$

Using Eqn. (3.91), the components of the velocity perturbation satisfy

$$\partial_z \tilde{u}_{j,y} = -\frac{e}{m\bar{u}_j}\left(\tilde{E}_y - \bar{u}_j \tilde{B}_x\right) + \frac{i\omega}{\bar{u}_j}\tilde{u}_{j,y}, \tag{3.92}$$

$$\partial_z \tilde{u}_{j,z} = -\frac{e}{m\bar{u}_j}\tilde{E}_z + \frac{i\omega}{\bar{u}_j}\tilde{u}_{j,z}. \tag{3.93}$$

Gauss's law yields:

$$\partial_z \tilde{E}_z = -\frac{e}{\epsilon_0}\sum_j \tilde{n}_j - ik_y \tilde{E}_y, \tag{3.94}$$

and from Ampère's law:

$$\partial_z \tilde{B}_x = \frac{i\omega}{c^2}\tilde{E}_y + \frac{e}{\epsilon_0 c^2}\sum_j \bar{n}_j \tilde{u}_{j,y}. \tag{3.95}$$

We can separate the z-derivative of the denstiy and velocity perturbations by substituting Eq. (3.93) into Eq. (3.90) and obtain:

$$d_z \tilde{n}_j = \frac{i\omega - d_z \bar{u}_j}{\bar{u}_j}\tilde{n}_j - \frac{ik_y \bar{n}}{\bar{u}_j}\tilde{u}_{j,y} - \frac{\tilde{u}_{j,z}}{\bar{u}_j} d_z \bar{n} - \frac{\bar{n}}{\bar{u}_j}\left(-\frac{e}{m\bar{u}_j}\tilde{E}_y + \frac{i\omega}{\bar{u}_j}\tilde{u}_{j,z}\right). \tag{3.96}$$

We now have a set of coupled linear ordinary differential equations that can be expressed as:

$$\boldsymbol{X}' = \underline{\boldsymbol{\Lambda}}\boldsymbol{X}. \tag{3.97}$$

Here $\boldsymbol{X}$ is a vector containing the perturbation components, the apostrophe $'$ denotes the spatial derivative with respect to z, and $\underline{\boldsymbol{\Lambda}}$ is the matrix containing the coefficients multiplying the perturbed components. We make the variables dimensionless by dividing the equation by an arbitrary scale length z_0. We introduce the dimensionless variable as:

$\zeta = z/z_0$. Furthermore, we make the number density, velocity and field perturbations dimensionless as: $\tilde{\mathcal{N}}_j = \tilde{n}_j/\bar{n}, \tilde{\mathcal{U}}_j = \tilde{\boldsymbol{u}}_j/\bar{u}, \tilde{\mathcal{E}}_\alpha = ez_0/(m_e\bar{u}^2)\tilde{E}_\alpha, \tilde{\mathcal{B}}_\alpha = ez_0/(m_e\bar{u})\tilde{B}_x$, where $\alpha = y, z$. By extension, the plasma frequency in dimensionless units is $\Omega_p = z_0\omega_p/\bar{u}$; the angular frequency in dimensionless units is $\Omega = z_0\omega/\bar{u}$; the dimensionless wave number is $\kappa_y = k_y/\bar{u}$, and the ratio between mean velocity and the speed of light $\beta = \bar{u}/c$. Equations (3.91), (3.92), (3.93, (3.94), (3.95) and eqn. (3.96) can be written as:

$$\partial_\zeta \tilde{\mathcal{E}}_y = -i\Omega\tilde{\mathcal{B}}_x + i\kappa\tilde{\mathcal{E}}_z, \tag{3.98}$$

$$\partial_\zeta \tilde{\mathcal{U}}_{j,y} = -\tilde{\mathcal{E}}_y + \tilde{\mathcal{B}}_x + i\Omega\tilde{\mathcal{U}}_{j,y}, \tag{3.99}$$

$$\partial_\zeta \tilde{\mathcal{U}}_{j,\zeta} = -\tilde{\mathcal{E}}_\zeta + i\Omega\tilde{\mathcal{U}}_{j,\zeta}, \tag{3.100}$$

$$\partial_\zeta \tilde{\mathcal{E}}_\zeta = -\Omega_p \sum_j \tilde{\mathcal{N}}_j - i\kappa\tilde{\mathcal{E}}_y, \tag{3.101}$$

$$\partial_\zeta \tilde{\mathcal{B}}_x = i\beta^2\tilde{\mathcal{E}}_y + \Omega_p^2\beta^2 \sum_j \tilde{\mathcal{U}}_{j,y}, \tag{3.102}$$

$$\partial_\zeta \tilde{\mathcal{N}}_j = (i\Omega_j + d_\zeta\bar{\mathcal{U}})\tilde{\mathcal{N}}_j - i\kappa_y\tilde{\mathcal{U}}_{j,y} - \tilde{\mathcal{U}}_{j,z} d_\zeta\bar{\mathcal{N}} + \tilde{\mathcal{E}}_y - i\Omega e\mathcal{U}_{j,z}. \tag{3.103}$$

We put these equations in the same form as in Eqn. (3.97) and show them in matrix form:

$$\begin{pmatrix} i\Omega - d_\zeta\mathcal{U} & i\kappa_y - i\Omega & -d_\zeta\bar{\mathcal{N}} & 0 & 0 & 0 & 1 & 0 & 0 \\ 0 & i\Omega & 0 & 0 & 0 & 0 & -1 & 0 & 1 \\ 0 & 0 & i\Omega & 0 & 0 & 0 & 0 & -1 & 0 \\ 0 & 0 & 0 & -i\Omega + d_\zeta\bar{\mathcal{U}} & i\kappa_y + i\Omega & d_\zeta\bar{\mathcal{N}} & 1 & 0 & 0 \\ 0 & 0 & 0 & 0 & -i\Omega & 0 & 1 & 0 & 1 \\ 0 & 0 & 0 & 0 & 0 & -i\Omega & 0 & 1 & 0 \\ 0 & 0 & 0 & 0 & 0 & 0 & 0 & i\kappa_y & -i\Omega \\ -\Omega_p^2 & 0 & 0 & -\Omega_p^2 & 0 & 0 & 0 & -i\kappa_y & 0 \\ 0 & \Omega_p^2\beta^2 & 0 & 0 & \Omega_p^2\beta^2 & 0 & -i\beta^2 & 0 & 0 \end{pmatrix} \cdot \begin{pmatrix} \tilde{\mathcal{N}}_1 \\ \tilde{\mathcal{U}}_{1,y} \\ \tilde{\mathcal{U}}_{1,\zeta} \\ \tilde{\mathcal{N}}_2 \\ \tilde{\mathcal{U}}_{2,y} \\ \tilde{\mathcal{U}}_{2,\zeta} \\ \tilde{\mathcal{E}}_y \\ \tilde{\mathcal{E}}_z \\ \tilde{\mathcal{B}}_x \end{pmatrix} = \begin{pmatrix} d_\zeta\tilde{\mathcal{N}}_1 \\ d_\zeta\tilde{\mathcal{U}}_{1,y} \\ d_\zeta\tilde{\mathcal{U}}_{1,z} \\ d_\zeta\tilde{\mathcal{N}}_2 \\ d_\zeta\tilde{\mathcal{U}}_{2,y} \\ d_\zeta\tilde{\mathcal{U}}_{2,z} \\ d_\zeta\tilde{\mathcal{E}}_y \\ d_\zeta\tilde{\mathcal{E}}_z \\ d_\zeta\tilde{\mathcal{B}}_x \end{pmatrix} \tag{3.104}$$

Eqn. (3.104) can be solved by obtaining its correspondent eigenvalues, which can yield k_z as $k_z = i\lambda$. Furthermore, the analysis will have to define an equilibrium number density distribution. In this situation, we can use a Gaussian distribution of the form $\bar{n} = n_0 \exp(-(z - z_0)^2/2c^2)$ where c is arbitrary. The velocity will have a Gaussian distribution as well: $\bar{u}_j = u_{0,j} \exp(-(z - z_0)^2/2c^2)$. Since for a chosen frequency this procedure yields spatially varying complex wave numbers, it is not straightforward to obtain the complex frequency corresponding to real wave numbers so that its imaginary part can immediately be interpreted as a growth rate. Therefore, as described in section 1.3, it is required to investigate for saddle points in the mapping of the frequency onto the complex wave number [29, 57]. To investigate the TSI, we can simply set $k_y = 0$, and determine k_z. For the CFI however, the perturbations will depend on both y ($\exp(ik_y y)$) and $z = 0$. This would make the distinction from oblique modes difficult. One way of distinguishing pure transverse modes would be by having purely imaginary k_z.

3.7 Summary

We have introduced the basic concepts of streaming instabilities in plasma. These are closely related to propagating waves, of which this medium supports a great variety. Using a fluid description of the plasma we have derived a dielectric tensor to describe its linear response to electromagnetic fields. This can be used in a secular equation to obtain dispersion relations for waves and instabilities in homogeneous plasma. We have derived the Bohm-Gross dispersion relation for longitudinal plasma waves and discussed its properties. We then discussed how unstable growth of waves is related to complex wavenumbers and frequencies introduced the distinction between convective and absolute instabilities. We focussed the discussion on instabilities arising from counterstreaming particle beams know as streaming instabilities, namely the two-stream instability, current filamentation instability and two-stream filametation/oblique instabilites. We derived their dispersion relations for cold uniform plasma with non-relativistic streaming speeds, discussed their properties, and compared them. We then widened the discussion by adding allowing for relativistic streaming speeds, finite temperature, and inhomogeneous density and discussed the effects on the instabilities. The concepts introduced in this chapter are the foundation for the results obtained in chapters 3 and 5.

Chapter 4

Side Electron Experiment

4.1 Introduction

Before proceeding to the final sections of the thesis, we will discuss an experiment that influenced the development of the theory corresponding of transverse ejection of electrons. This chapter reports are experiments in the paper: "Generation of ultra-high charge beams from a laser wakefield accelerator driven by a petawatt laser" by Antoine Matraillain that has been submitted for publication at the time of writing of the thesis. The author was not involved in the experiments and the data analysis of thereof, but was involved in discussions and development of the theoretical section of the paper.

4.2 Motivation and description of the experiment

In wakefield acceleration, only a fraction of plasma electrons are accelerated to high energies [80]. Non-injected electrons, which are particles that are not injected into the bubble, constitute by far the largest portion of plasma electrons, gain momentum from the laser pulse and form the sheath of the plasma bubble, are emitted obliquely in a well defined conically-shaped, low energy electron beam, in the forward direction, by a "sling-shot" action [81, 82, 83, 84, 85]. Relativistic electrons are emitted at angles of up to about 60° from the laser axis in the forward direction and a weakly relativistic beam is also emitted in the counter-propagation direction [83, 85]. The energy of side electrons is acquired from the ponderomotive force of the intense laser pulse. The oblique, forward emitted beam has a broad energy spectrum with a mean energy in the MeV range, a relatively high divergence ($\approx 10^{\circ}$) and relatively short duration (sub-ps in an angular segment) at the accelerator exit. Surprisingly, very high charge "side electron" beams of several nC has been observed by several groups [81, 82, 83, 85]. They have an energy-angle correlation with a slice energy spread of $\approx 10\,\%$[83]. Recently, higher energy, very high charge electron beams have also been generated in the forward direction, with relatively high efficiencies, using relatively long duration and high energy laser pulses [86].

The sheath electrons converging at the rear of the bubble, prior to being emitted as side electrons, form regions of very high local densities that can exceed $10^{22}\,\mathrm{cm}^{-3}$ in the sheath-crossing region at the back of the bubble, for ambient plasma densities of $10^{19}\,\mathrm{cm}^{-3}$. Counter-streaming beams have momenta of several $m_e c$, where m_e is the electron rest mass and c is the speed of light in vacuum. A more complete picture of the electron motion will help evaluate the overall efficiency of the accelerator, and how the laser energy is apportioned. Because the efficiency of producing side electrons can approach several tens of percent (conversion of laser energy to electron beam energy) it opens up the potential of using the beams for sterilisation [87], ultra-fast studies in condensed matter [88], pulsed radiolysis [89], dense matter imaging [90] and as energetic secondary sources of THz radiation [90, 91]. In addition, the study of converging charged particle beams is relevant to extreme astrophysical scenarios [36], such as supernovae [92], gamma-ray bursts [4, 38] and coronal mass ejection [39, 40, 93], and to inertial confinement fusion [4, 72, 94]. Another more practical reason for understanding the properties of side electrons is that they cause damage to equipment and components surrounding the LWFA, including capillaries, translation stages, gas jet controllers, optics, detectors etc., either directly, or by producing secondary radiation. Side electrons can carry off several tens of percent of the laser energy and create significant quantities of unwanted background radiation, which has a significant impact on use of petawatt lasers to drive LWFAs[83].

The emission of the side electron beam depends intimately on the evolution of the bubble and is closely connected to electron self-injection leading to high energy electron beams. Side electrons counter stream at the back of the bubble prior to being ejected, which creates ideal conditions for observing new plasma and beam instabilities.

The investigation of the production of side electron beams was undertaken using the 17 J CLPU VEGA petawatt laser in Salamanca [95, 96]. It was shown that side electrons can be produced with high efficiencies, in excess of tens of percent. It was also shown that $\approx 500\,\mathrm{nC}$, MeV level bunches can carry away about 1 J of the incident laser energy (6 J of laser energy is concentrated in the central laser spot of the 17 J, PW laser pulse). A fine ray-like spatial structure was observed to be imprinted onto the side electron beams, which we ascribe to filamentation and streaming instabilities that occurr when electrons counter-stream at the rear of the bubble. The experimental findings are compared with analytic models and PIC simulations.

4.3 Laser

The experiments were carried out using the 800 nm wavelength PW laser VEGA-3 [95] at the Centro de Láseres Pulsados (CLPU), in Salamanca, Spain. The laser pulse energy on target is 17.45 ($\pm$ 0.78) J, its beam diameter is 22 cm and it is linearly polarised. It is focused with a 2.5 m focal length off-axis parabolic (OAP) mirror to a 16.3 ($\pm$ 1.1) µm FWHM focal spot containing 29.3 ($\pm$ 0.1) % of the total laser energy. The laser pulse duration is measured using a Fastlite Wizzler$^{\text{TM}}$ to be 26.3 ($\pm$ 0.1) fs FWHM. This results in a maximal initial $a_0 = 3.89 \pm 0.41$.

4.4 Gas target

The gas target used is a 5 mm supersonic gas jet emanating from a nozzle, presenting a flat top-like profile with 250 µm gradients at a pressure of 40 bar. The gas used is a mixture of 99% He and 1% N_2, resulting in a background electron density of about $1.2 \times 10^{19}\,\text{cm}^{-3}$ at 2.4 mm above the nozzle exit.

A Lanex "Regular" is placed close to the interaction point to image the spatial distribution of the side electron beam in two different configurations. In the first, only half of the beam is imaged because of geometric constraints in the chamber, with the Lanex screen placed 65 mm from the source and 15 mm from the laser axis at a 32° angle from this axis. In the second configuration, a Lanex screen is placed orthogonal to the laser axis and 30 mm from the source, with an aperture that allows the laser to propagate though the screen. This enables imaging of the full side electron beam profile, as shown in Fig. 4.3**a**.

A sheet of HD-V2 Gafchromic film [97] is wrapped around the nozzle. Two apertures pierce the film to allow the laser pulse to propagate through. A single laser shot produces a side electron beam, irradiating the film. A sample of the film from the same batch was externally calibrated to determine the total incident charge. The total charge of the side electron beam is estimated by recording the dose deposited in HD-V2 Gafchromic film bent around the gas jet into a cylinder of 2.3 cm radius. Apertures in the film allow the passage of the laser and the on axis, narrow divergent electron beam. A 15 µm thick aluminium foil covering the inner and outer faces of the film prevents exposure due to reflected light. Each laser shot, with energies on target that can exceed 17 J produces a side electron beam, which is recorded and scanned. The film was scanned one week after irradiation using an EPSON 10000XL Pro Flat Bed Scanner, to produce a 48 bit RGB image. The dose distribution around the exit aperture recorded by the red channel is shown in Fig. 4.1 (**a**), which is processed using the protocol described in [98]. To reconstruct the dose distribution, a film calibration was performed at the National Physical Laboratory (NPL) by exposing HD-V2 from the same batch as used in experiments, to beams from a 12 MeV clinical linac depositing doses between 5 Gy and 1900 Gy.

The experimental dose distribution has been reproduced in numerical simulations using the Monte Carlo code Geant4 [99], which models the electron beam with a Gaussian transverse spatial profile interacting with an HD-V2 film for the same geometry as in the experiment. This is shown as a thick line in Fig. 4.1 (**b-d**), with the experimental data plotted as symbols. The beam divergence, energy and charge have been adjusted to produce a radial dose profile matching the experimental distribution. Results for the blue and green channel indicate a total charge of 500 ± 50nC. The charge estimated from the red channel is around 30 % higher, but this is likely due to errors due to saturation. The maximum dose measured experimentally is about 3 times higher than the maximum doses used for calibration at NPL. The dose-response curve has therefore been extrapolated. This extrapolation is likely to fail for the red channel, which is the most sensitive and the first to saturate.

Assuming 500 nC charge and an average energy of 1.3 MeV, the total energy carried by the electron beam (in the forward direction) is 650 mJ. This energy corresponds to 3.7 ± 0.5 % of the total laser energy or 12.7 ± 1.9 % of the laser energy in the focal spot, which shows that a significant portion of the energy is transferred to the side electron beam, and that it is important to take it into account when considering the efficiency of an LWFA.

4.5 Results

4.5.1 Side electron beam charge characterisation

Experimental results

The VEGA PW laser beam is focussed to a 13.8 µm radius spot (assuming a Gaussian focal spot radius at 1/e^2 intensity) where the normalised amplitude $a_0 = \sqrt{2I_L/(\epsilon_0 c)}(e/m_e c\omega_L)$ can be varied between 1.2 and 3.9, where e is the charge of an electron, ω_L and I_L are the laser frequency and intensity, respectively, and ϵ_0 is the vacuum permittivity. A 5 mm

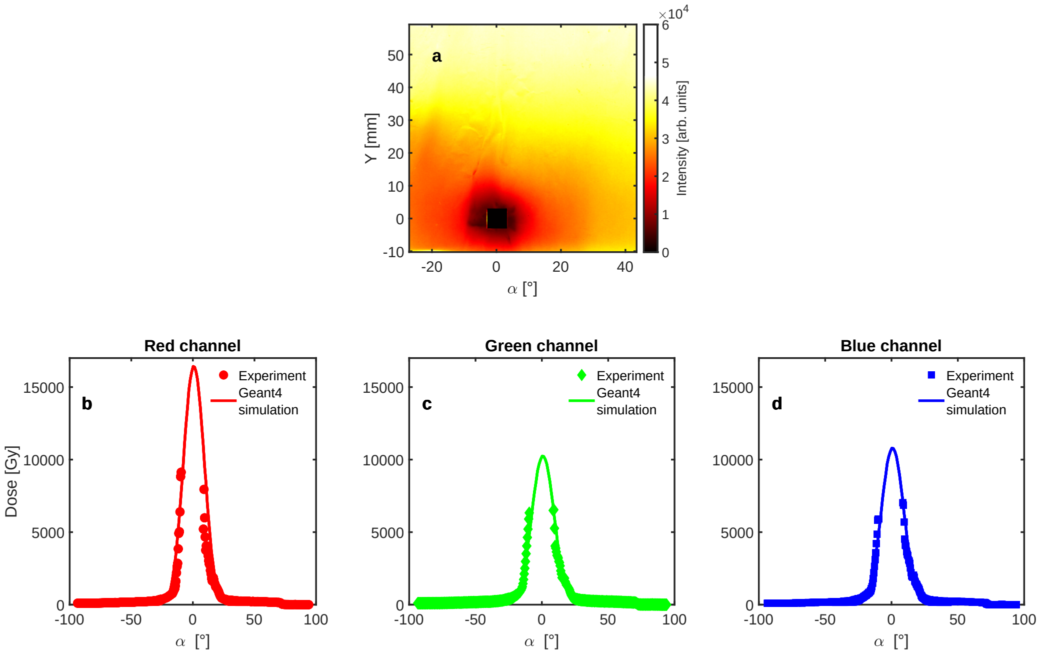

Figure 4.1: **a**, scanned HD-V2 Gafchromic film image. **b-d**, plots of the deposited dose as a function of the angle from the laser axis for the 3 channels, red, green and blue, respectively. The symbols represent the experimental data, while the line is for Geant4 simulations.

wide helium gas jet is used to produce plasma with a density of $n_e \approx 1.2 \times 10^{19}\,\mathrm{cm}^{-3}$.

4.6 Simulations to estimate the charge of side electron beams

The simulations in this section were performed and analysed by Dr. Enrico Brunetti.

Simulations were performed using the quasi-3D particle-in-cell code `FBPIC` [100] to investigate the gross properties of the side side electron beams emitted by a linearly-polarized 800 nm laser interacting with pre-ionized plasma of 5 mm length and electron density of 1.4 x $10^{19}\,\mathrm{cm}^{-3}$. The ions are considered immobile and the laser energy is varied from 1 J to 14 J. It was checked that enabling ion motion does not significantly change the simulation results. The transverse profile is Gaussian with a waist (radius at $1/e^2$ intensity) of 20 µm. The temporal profile is a $\cos^2$ function with a FWHM of 20 fs. As described in references [83, 85], side electron beams are generated when the ponderomotive force of the laser pushes plasma electrons away from the high-intensity region. These electrons stream backwards forming an ion-filled cavity ("bubble") trailing the laser pulse. A small fraction of these electrons are trapped inside the bubble and accelerate to high energy. The majority are ejected over a large angle, gaining an average energy of 1-2 MeV.

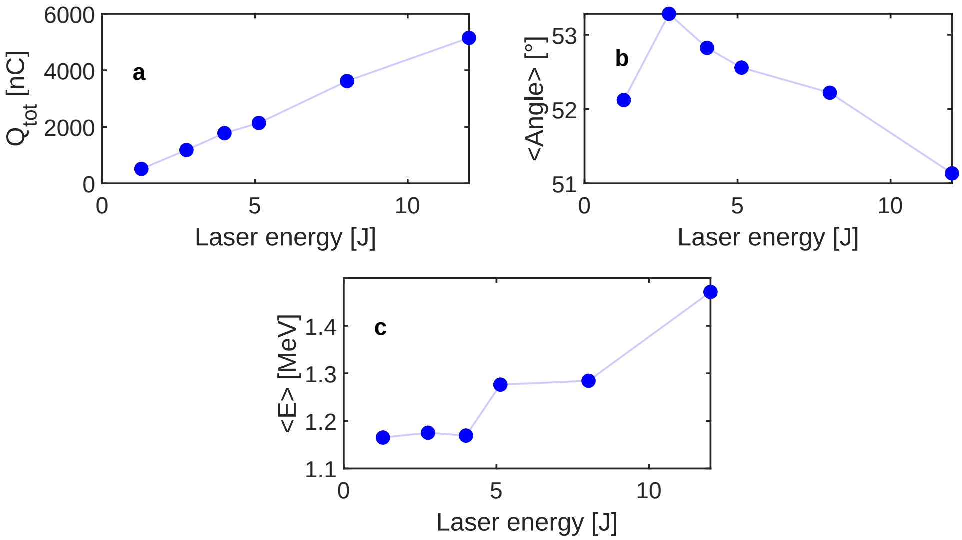

Figure 4.2: (**a**) Total charge emitted. (**b**) Average emission angle. (**c**) Average electron energy. The blue line is to guide the reader's eye.

Figure 4.2 **a** shows that the total charge contained within the side angle electron beam grow is predicted to linearly with laser energy, reaching values of several µC. The mean angle, shown in Fig. 4.2 (**b**), is approximately constant, at 51°-53°. The mean energy of the side electron beams, shown in Fig. 4.2 (**c**), also depends weakly on laser energy and is around 1-1.5 MeV. As reported in [83, 85] there is a dependence of energy on angle. Electrons that experience the fields inside the bubble for a longer period of time gain a higher longitudinal momentum and are therefore emitted closer to the laser axis. This is in good agreement with the experimental observations reported in the following section.

4.6.1 Side electron beam spatial structure

Experimental results

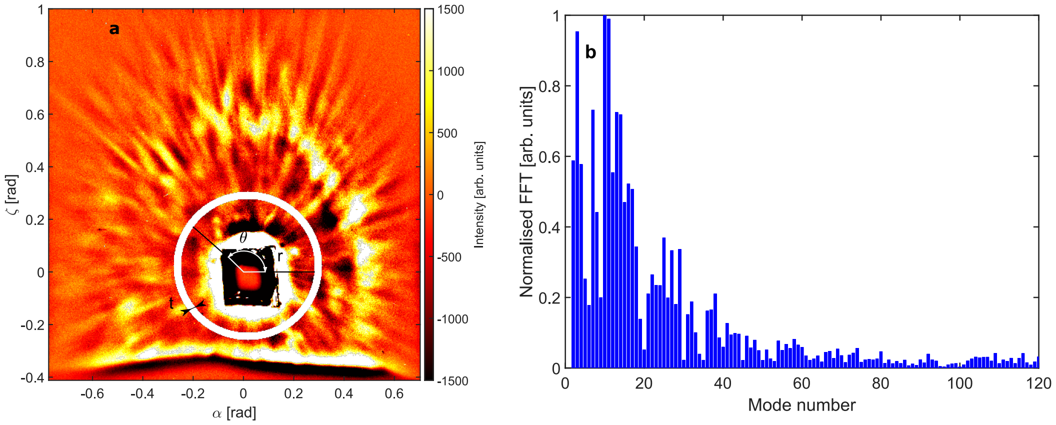

Figure 4.3: Typical angular profile of side electron beams measured on a Lanex screen positioned 30 mm from the accelerator. (**a**) A false colour image showing the 2D charge distribution where a Gaussian filter was applied and substracted from the raw image. (**b**) The Fourier Transform of the radially integrated charge distribution in the ring displayed in (**a**) as a function of the azimuthal mode number.

A typical image of the angular profile of the side electron beam is shown in Fig. 4.3 (**a**). This is measured on a Lanex screen placed 30 mm from the source. A hole in the centre of the screen allows passage of the laser beam and the forward high-energy electrons.

4.6.2 Modal decomposition

Radial, ray-like striations are observed across the entire beam. A Gaussian filter is applied to the image and then subtracted from it to minimise the effect of gross asymmetries due to the interaction and geometrical distortions, which emphasises the striations. A section of the image, corresponding to a ring of radius r and thickness t, marked in the figure, has been selected for analysis. A fast Fourier transform (FFT) is applied to the charge distribution averaged radially over the thickness t, which is shown in Fig. 4.3(**b**) as a function of the mode number l, describing a periodicity of $2\pi/l$. It is clear that most of the excited modes, with spectral intensity higher than 0.4, have low mode numbers (< 50). Mode numbers of interest here are above 10, given the typical periodicity of the striations of interest in this work.

The parameters r and t defining the region of interest have been varied to evaluate the robustness of the striation pattern, demonstrating that the mode distribution is independent of both parameters. In contrast, it is very sensitive to the position of the centre of the ring, which is carefully determined by identifying the point of convergence of several striations or rays.

The energy spectrum of the side electron beam is measured using two methods: a dipole magnet with a Lanex screen, and an array of thin aluminium sheets. The average energy is found to be slightly higher than 1 MeV and depends on the emission angle, which is consistent with previous observations [81, 82, 83, 85] and the PIC simulation results presented in the previous section.

The side electron beam is extremely robust and shows very little dependence on

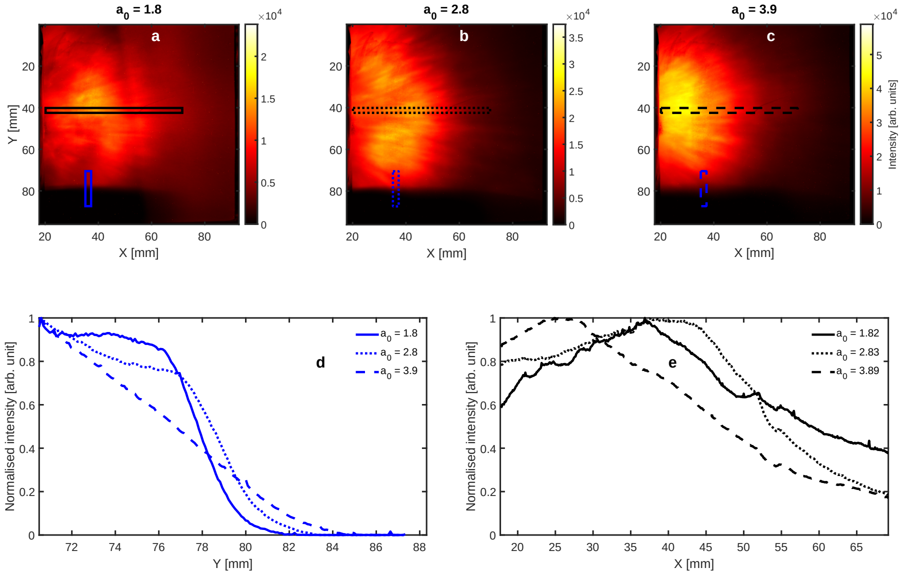

Figure 4.4: Spatial profile of half side electron beam obtained on a Lanex screen positioned 65 mm from the accelerator for different laser energies. (**a-c**) False colour images for a_0 of 1.8, 2.8 and 3.9, respectively. (**d**) Normalised charge distribution inside the vertical (blue) rectangle overlaid on images (**a-c**) summed horizontally. (**e**) Normalised charge distribution inside the horizontal (black) rectangle overlaid on images (**a-c**) summed vertically.

experimental parameters, such as longitudinal position of the nozzle with respect to the laser focal plane, or the pulse duration. In particular, side electron beams are produced even when no forward electrons are observed, in contrast to reference [84]. Nevertheless, the charge increases and the spatial distribution of the side electron beam evolves with the laser energy, as previously predicted [83]. This is shown in Fig. 4.4 (**a-c**) and (**e**). Figure 4.4 (**a-c**) presents false colour images of the Lanex screen, located 65 mm from the source, intercepting around half of the side electron beam profile during an energy scan.

The signal in the vertical blue rectangle on Fig. 4.4 (**a-c**) is summed horizontally, normalised and plotted in Fig. 4.4 (**d**). The bottom region on Fig. 4.4(**a - c**) is darker due to the shadow of the gas nozzle, which blocks part of the emitted side electron beam. From Fig. 4.4 (**d**), it can be observed that the 90–10 % of the distance (the distance required for the edge response to rise from 10 % to 90 %) value increases with the laser normalised intensity, from about 4 mm at the lowest intensity up to and longer than the accessible length (>15 mm) for the highest intensity, demonstrating an increase in the size of the electron source. This means that the side electron beam source length increases and can be understood by calculating the laser depletion length [101, 102] for these parameters, which varies from 0.84 to 2.5 mm between the two energies considered. This is also observed in the plasma channel top-view diagnostic and in PIC simulations.

The signal contained inside the horizontal black rectangle overlaid in Fig. 4.4 (**a-c**) is summed vertically, normalised and plotted in Fig. 4.4 (**e**). It shows that the charge distribution is close to a ring-like distribution at lower laser energies, and fills the cone at higher energies, as predicted in Yang et al., [83]. The striations are always observed, regardless of the experimental parameters.

The top and bottom panels in Fig. 4.5 show the averaged FFT and associated standard deviation of the normalised intensity in a ring, obtained with the same method used to generate Fig. 4.3 (**b**), for consecutive shots (> 5) and normalised laser vector amplitudes $a_0 = 1.8$ (Fig. 4.5, top panel) and $a_0 = 3.9$ (Fig. 4.5, bottom panel). This figure clearly shows that the modes excited in the region of interest ($l > 10$) are situated in the same region of the spectrum (around mode 15 ± 5). The effect of a longer source size on the striations has been investigated by comparing the modes excited as a function of the normalised intensity (during a laser energy scan). It was shown earlier in this section that increasing the energy lengthened the source size. One may expect

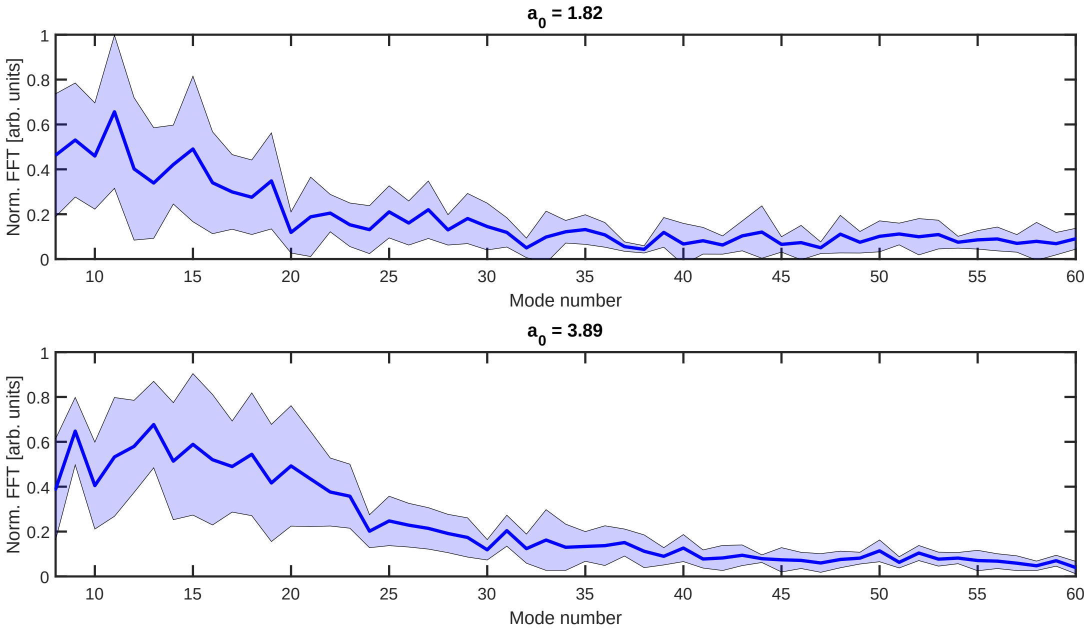

Figure 4.5: Azimuthal mode distribution obtained at different values of a_0. Averaged and standard deviation (blue area) FFT of the normalised intensity signal for consecutive shots at $a_0 = 1.8$ (in top panel) and $a_0 = 3.9$ (in bottom panel).

different modes excited during acceleration, hence blurring the striations at higher laser energy. However, this is not what is observed. The number of modes excited (for which the spectral intensity is above a given threshold) per shot is similar for higher energies and the mode number distribution does not vary dramatically. The fluctuations in the mode numbers excited can be explained by shot-to-shot variations of the electron sheath density as will be discussed in the following section. This demonstrates that the excited modes develop according to local conditions in a given region of the spectrum at the beginning of the interaction (with no evidence of repeatable modes shot-to-shot) and these modes are frozen in over the full length of interaction (similar number of modes are excited for different a_0 values).

4.7 Conclusion

In conclusion, we have demonstrated the production of extremely high charge ($>500 \pm 50\,\mathrm{nC}$) MeV electron beams, emitted with an efficiency exceeding 10%, from a LWFA driven by a few Joule PW-class laser. This corresponds to a current of the order of 50 kA. Striations are observed in the emitted electron beams, which are ascribed to streaming instabilities excited when counter-streaming electrons interact at the back of the LWFA bubble. High efficiency production of this type of electron beam may be useful for applications requiring high currents, such as pulsed radiolysis [89], and as energetic secondary sources of THz radiation [90, 91] due to the extremely high charge achieved with a single laser shot. The description of the particle dynamics and counter-streaming electron flows follow in the next chapters

Chapter 5

Current Filamentation Instability in a Converging Geometry

5.1 Introduction

Converging geometries are abundant in laboratory and space plasmas, include inertial confinement fusion [4, 36], gamma ray bursts [4, 38], coronal mass ejections [39, 93], and laser wakefield accelerators (LWFAs) [5, 103, 104, 105]. The LWFA accelerating structure is comprised of an electron-evacuated ion cavity, or “bubble” surrounded by a high-density sheath of electrons that stream around the bubble surface before converging and crossing at the back of the bubble. Most electrons converge and pass through a small region at the back of the bubble rather than being injected into it. After this, some electrons form subsequent bubbles whilst others are ejected transversely and lost as “side electrons" [106]. This chapter is partly based on the paper Iñigo Gamiz *et al* [107]. We are considering the region of the LWFA at the back of the bubble through which particles pass and investigate instabilities in counterstreaming plasmas in converging geometries. This chapter begins by introducing the geometry and the approach used to develop an analytical description of instabilites in a cold, relativistic, and inhomogeneous plasma. Then, the results of PIC simulations are presented and compared to the analytical theory. In the second part of this chapter, a finite temperature is introduced to the momentum equations to account for thermal effects. The growth rates are then studied as a function of temperature and mode number. PIC simulations using a fixed mode number and varying temperature as well as fixing a temperature and varying mode number are presented and the inferred growth rates from the simulations and the theoretical predictions are compared.

5.1.1 Fluid approach in a Converging Geometry

Electrons forming the sheath around a LWFA bubble return to its axis, pass through a small region close to the axis, and then move away from it [107]. This part of the bubble observed from a reference frame co-propagating with the back of the bubble, can be seen as constant streams of electrons propagating radially inwards and outwards. Therefore, we can simplify further by modelling the back of the bubble as a disk transverse to its axis where streams of particles converge and diverge. Because the streams overlap, they should be susceptible to streaming instabilities. Two-stream instability (TSI) in a converging geometry [108] have been investigated, but not until recently for the current filamentation instability (CFI) and oblique instabilities [107].

The fluid approaches for studying plasma is common. The continuity and momentum equations coupled with Maxwell's equations are used as a framework, which treats the plasma as a collection of charged fluid elements [1].

$$\partial_t n_j = -(\partial_r \hat{e}_r + r\partial_\theta \hat{e}_\theta) \cdot (n_j \boldsymbol{u}_j)\,, \tag{5.1}$$

$$(\partial_t + \boldsymbol{u}_j \cdot (\partial_r \hat{e}_r + r\partial_\theta \hat{e}_\theta))\boldsymbol{p}_j = q_j\,(\boldsymbol{E} + \boldsymbol{u}_j \times \boldsymbol{B}) - (\hat{e}_r \partial_r + i\ell \hat{e}_\theta)\boldsymbol{P}_j / n_j, \tag{5.2}$$

$$(\partial_r \hat{e}_r + r\partial_\theta \hat{e}_\theta) \cdot \boldsymbol{E} = \sum_{j=1}^{N} \frac{q_j n_j}{\epsilon_0}, \tag{5.3}$$

$$(\partial_r \hat{e}_r + r\partial_\theta \hat{e}_\theta) \cdot \boldsymbol{B} = 0, \tag{5.4}$$

$$(\partial_r \hat{e}_r + r\partial_\theta \hat{e}_\theta) \times \boldsymbol{E} = -\partial_t \boldsymbol{B}, \tag{5.5}$$

$$(\partial_r \hat{e}_r + r\partial_\theta \hat{e}_\theta) \times \boldsymbol{B} = \frac{1}{c^2}\partial_t \boldsymbol{E} + \mu_0 \sum_{j}^{N} q_j n_j \boldsymbol{u}_j, \tag{5.6}$$

where the subscript j corresponds to the particle species; n_j is the number density; $\boldsymbol{u}_j$ is velocity; $\boldsymbol{p}_j$ is momentum; q_j is the charge of the species; $\boldsymbol{E}$ is the electric field; $\boldsymbol{B}$ is the magnetic field; and $\boldsymbol{P}_j$ is the pressure tensor; r is the radial position; θ is azimuthal angle; μ_0 is the free-space permeability and c is the speed of light in vacuum. We assume a cold plasma and neglect the pressure tensor. For a perturbation analysis, small perturbation is added to the equilibrium state, and expanded to first (or sometimes higher) order in these perturbations. The linear equations for first-order perturbations can be Fourier-analysed by assuming harmonic time and space dependence if the equilibrium is stationary and homogeneous $\psi \approx \bar{\psi} + \tilde{\psi}$, where ψ is an arbitrary variable, the bar denotes the equilibrium component, the tilde denotes the perturbation and $|\tilde{\psi}|/|\bar{\psi}| \ll 1$ is assumed. Harmonic perturbations in a homogeneous system have the following form: $\tilde{\psi} = \psi_0 \exp(i\boldsymbol{k} \cdot \boldsymbol{x} - i\omega t)$, where ψ_0 is the amplitude, $\boldsymbol{k}$ is the wave vector, $\boldsymbol{x}$ is a position vector, ω is the angular frequency and t is time.

In the case of disk-like converging geometry, the equilibrium continuity equation implies that the radial flow of particles is inhomogeneous. For simplicity, we choose a radial flow with homogeneous speed, and consequently, the density is inhomogeneous:

$$\begin{aligned}
\partial_t \bar{n}_\pm &= -\nabla \cdot \bar{n}_\pm \bar{\boldsymbol{u}}_\pm, \\
0 &= \frac{\bar{u}_\pm}{r}\partial_r (r\bar{n}_\pm), \\
0 &= \partial_r (r\bar{n}_\pm), \\
\bar{n} &= \frac{n_{\pm,0} r_0}{r},
\end{aligned}$$

where $\bar{n}$ is the background plasma density; n_0 is the number density multiplied by reference radial position r_0, which can be chosen arbitrarily; r is radial position; and $\bar{u}$ is the radial velocity. The singularity as $r \to 0$ can be avoided by assuming a small thermal spread in the velocities of the converging electrons [107] so they do not converge on a single point. In this study, we avoid this region.

As a consequence of the inhomogeneous number density, the radial wave number will inherit the inhomogeneity. The number density, velocity and the fields can still be assumed to have a harmonic dependence in the azimuthal angle θ and frequency ω. An analytical approach to obtain an imaginary frequency will yield a 9th order differential equation that may yield some un-physical solutions due to the high order. Instead, a semi-analytical approach is adopted here in which the set of ordinary differential equations is treated as an eigenvalue problem. In this case, the local wavenumbers $k_r(r)$ are calculated for a fixed frequency. The local wavenumbers can yield a spatial growth rate. If we are sufficiently far away from the origin, the WKB appromation is applicable.

The perturbations will now take the form $\tilde{\psi}(r,\theta,t) = \psi_0 \exp(i\int k_r(r)dr + i\ell\theta - i\omega t)$, where ℓ is mode number. The continuity, momentum and Maxwell's equations can be linearised to obtain an approximate solution to the set of coupled, linear ordinary differential equations. We opted for a semi-analytical approach where a set of 9 coupled, linear ordinary differential equations is used to describe the instability and obtain its growth rates. The perturbed continuity equation takes the following form:

$$\frac{\mathrm{d}}{\mathrm{d}r}\tilde{n}_\pm = \frac{i\omega\tilde{n}_\pm}{\bar{u}_{\pm,r}} - \frac{1}{r}\tilde{n}_\pm - \frac{\bar{n}_\pm}{\bar{u}_{\pm,r}}\frac{\mathrm{d}}{\mathrm{d}r}\tilde{u}_{\pm,r} - \frac{\tilde{u}_{\pm,r}}{\bar{u}_{\pm,r}}\frac{\mathrm{d}}{\mathrm{d}r}\bar{n}_\pm - \frac{i\ell\bar{n}}{\bar{u}_{\pm,r}r}\tilde{u}_{\pm,\theta} - \frac{\bar{n}}{\bar{u}_{\pm,r}}\tilde{u}_{\pm,r}, \tag{5.7}$$

where the subscript ± corresponds to outflowing and inflowing electrons respectively. Similarly, one can obtain differential equations corresponding to the radial and azimuthal velocities.

$$\frac{\mathrm{d}}{\mathrm{d}r}\tilde{u}_{\pm,r} = -\frac{e\tilde{E}_r}{m\gamma^3} + \frac{i\omega}{\bar{u}_\pm}\tilde{u}_{\pm,r}, \tag{5.8}$$

$$\frac{\mathrm{d}}{\mathrm{d}r}\tilde{u}_{\pm,\theta} = \frac{1}{\gamma\bar{u}_\pm}\left(-e\tilde{E}_\theta + \bar{u}_\pm\tilde{B}_z\right) + \frac{i\omega}{u}\tilde{u}_{\pm,\theta}. \tag{5.9}$$

Here, γ is the relativistic Lorentz factor corresponding to the mean flow; m is the electron mass; and e is the electron charge. Eq. (5.8) can be substituted into Eq. (5.7) and remove the differential of the radial velocity to yield:

$$\frac{\mathrm{d}}{\mathrm{d}r}\tilde{n}_\pm = \frac{i\omega\tilde{n}_\pm}{\bar{u}_{\pm,r}} - \frac{1}{r}\tilde{n}_\pm - \frac{\bar{n}_\pm}{\bar{u}_{\pm,r}}\left(-\frac{e\tilde{E}_r}{m\gamma^3} + \frac{i\omega}{\bar{u}_\pm}\tilde{u}_{\pm,r}\right) - \frac{\tilde{u}_{\pm,r}}{\bar{u}_{\pm,r}}\partial_r\bar{n}_\pm - \frac{il\bar{n}}{\bar{u}_{\pm,r}r}\tilde{u}_{\pm,\theta} - \frac{\bar{n}}{\bar{u}_{\pm,r}}\tilde{u}_{\pm,r}. \tag{5.10}$$

Following from Gauss's law (Eq. (5.3)), one obtains a differential equation for the radial electric field:

$$\frac{\mathrm{d}}{\mathrm{d}r}\tilde{E}_r = -\frac{e}{\epsilon_0}(\tilde{n}_+ + \tilde{n}_-) - \frac{1}{r}\tilde{E}_r - \frac{il}{r}\tilde{E}_\theta. \tag{5.11}$$

From Faraday's law, Eq. (5.5), one obtains:

$$\frac{\mathrm{d}}{\mathrm{d}r}\tilde{E}_\theta = \frac{il}{r}\tilde{E}_r - \frac{1}{r}\tilde{E}_\theta + i\omega\tilde{B}_z. \tag{5.12}$$

And finally, from Ampère's law (Eq. (5.6)),

$$\frac{\mathrm{d}}{\mathrm{d}r}\tilde{B}_z = i\omega\tilde{E}_\theta + \frac{e\mu_0}{c^2}(\bar{n}_+\tilde{u}_+ + \bar{n}_-\tilde{u}_-). \tag{5.13}$$

From Ampère's law one also obtains a redundant equation:

$$\frac{il}{r}\tilde{B}_z = i\frac{\omega}{c^2}\tilde{E}_r - e\mu_0\left(\bar{n}(\tilde{u}_{+,r} + \tilde{u}_{-,r}) + u\left(\tilde{n}_+ - \tilde{n}_-\right)\right) \tag{5.14}$$

In this case, it can be ignored because it will not be of much use in our analysis method. By adding a scale length r_0 and introducing the dimensionless position $\xi = r/r_0$, the equations can be made dimensionless and take on the following form:

$$\frac{\mathrm{d}}{\mathrm{d}\xi}\mathcal{N}_\pm = \mp i\Omega\mathcal{N}_\pm - \frac{\mathcal{N}_\pm}{\xi} \mp \frac{\mathcal{E}_r}{\xi\gamma^3} \mp \frac{i\Omega\mathcal{U}_{\pm,r}}{\xi} - \frac{i\ell\mathcal{U}_{\pm,\theta}}{\xi^2}, \tag{5.15}$$

$$\frac{\mathrm{d}}{\mathrm{d}\xi}\mathcal{U}_{\pm,r} = \pm\frac{\mathcal{E}_r}{\gamma^3} \pm i\Omega\mathcal{U}_{\pm,r}, \tag{5.16}$$

$$\frac{\mathrm{d}}{\mathrm{d}\xi}\mathcal{U}_{\pm,\theta} = \frac{\mathcal{B}_z}{\gamma} \pm \frac{\mathcal{E}_\theta}{\gamma} \pm i\Omega\mathcal{U}_{\pm,\theta}, \tag{5.17}$$

$$\frac{\mathrm{d}}{\mathrm{d}\xi}\mathcal{E}_r = \Omega_{\mathrm{p}}^2(\mathcal{N}_- + \mathcal{N}_+) - \frac{\mathcal{E}_r}{\xi} + \frac{i\ell\mathcal{E}_\theta}{\xi}, \tag{5.18}$$

$$\frac{\mathrm{d}}{\mathrm{d}\xi}\mathcal{E}_\theta = \frac{i\ell\mathcal{E}_r}{\xi} - \frac{\mathcal{E}_\theta}{\xi} + i\Omega\mathcal{B}_z, \tag{5.19}$$

$$\frac{\mathrm{d}}{\mathrm{d}\xi}\mathcal{B}_z = i\Omega\beta^2\mathcal{E}_\theta + \frac{\Omega_{\mathrm{p}}^2\beta^2}{\xi}(\mathcal{U}_{+,\theta} + \mathcal{U}_{-,\theta}), \tag{5.20}$$

where $\mathcal{N}_\pm = \tilde{n}_\pm/n_0$; $\mathcal{U}_{\pm,\alpha} = \tilde{u}_{\pm,\alpha}/\bar{u}$; $\mathcal{E}_\alpha = er_0\tilde{E}_\alpha/(m\bar{u}^2)$; $\mathcal{B}_z = er_0\tilde{B}_z/(m\bar{u})$; $\Omega = r_0\omega/\bar{u}$; $\Omega_{\mathrm{p}}^2 = e^2n_0r_0^2/(\epsilon_0 m\bar{u}^2)$; the subscript $\alpha = r,\theta$. The set of equations from 5.15-5.20, can be re-written as:

$$X' - \Lambda X = 0, \tag{5.21}$$

where X contains the vector composed of the perturbations, X' is its derivative with respect to ξ and Λ is the matrix containing the coefficients multiplying the perturbations as in equations (5.15-5.20) .

5.1.2 Semi-analytical description

The eigenvalues and the radial wave numbers can be related by $k_r r_0 = -i\lambda$. The eigenvalues can be obtained numerically using the numerical python (`NumPy`) [109] library. Similarily as in the slab geometry (see the chapter 2), a plasma can become unstable if there are two real parts of both wavenumbers and frequencies that coalesce and two imaginary parts bifurcate [57]. However, the geometry in the inhomogeneous case adds spatial variations to the wave amplitude, as well as unstable growth due to the instability.

The TSI can be described using equations (5.15-5.20) by eliminating the azimuthal dependence ($\ell = 0$). The azimuthal velocity, azimuthal electric field and the magnetic field in $\hat{e}_z$ will vanish. The set of equations, with the used parameters, does not demonstrate any coalescence or bifurcation of the real and imaginary parts of the wave numbers implying that the TSI is not present. This may seem to contrast with Gratton and Gnavi [108]. However, their calculations include a singularity in the electric field at the origin, whilst ours avoid that region. We deem the presence of a singularity unrealistic and this difference may be the reason for the discrepancy between Gratton and Gnavi's and ours.

Besides the CFI and TSI, oblique instabilities [56] are possible for modes with non-zero ℓ, i.e., azimuthal variations of the perturbations, as well as in the direction of the streaming velocities. Such instabilities combine properties of both CFI and TSI and, for a homogeneous system, can grow at a particular angle. As the interaction of counter-propagating beams continues and the instability enters the nonlinear phase, the interplay between modes with similar growth rates can enhance a "dominant mode"[110].

Fig 5.1. shows the real and imaginary parts of the wave numbers k_r. The real wave numbers demonstrate outgoing waves ($\mathrm{Re}(k_r) > 0$) and ingoing waves ($\mathrm{Re}(k_r) < 0$) as well as non-propagating perturbations ($\mathrm{Re}(k_r) = 0$). The imaginary parts of k_r show decay ($\mathrm{Im}(k_r) > 0$) and growth ($\mathrm{Im}(k_r) < 0$) with increasing r. The blue region shows

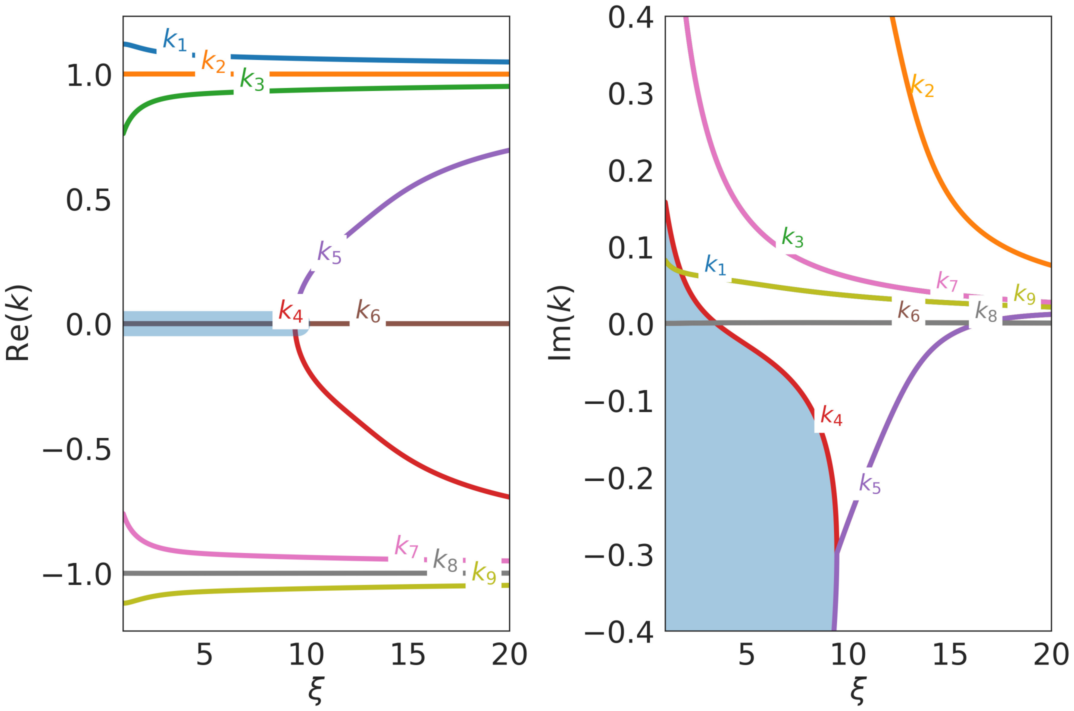

Figure 5.1: Real (left) and imaginary (right) parts of the complex wave number k_r as a function of position (ξ) with number density $\bar{n}(r_0) = 10^{19}\,\mathrm{cm}^{-3}$, $r_0 = 1\mu\mathrm{m}$, $\gamma = 2$, a fixed real frequency $\Omega = 1$, mode $\ell = 10$. Real and imaginary parts of each branch are shown in the same colour, and the region of instability is shaded

the radial range where the instability occurs. This implies that for these parameters the waves will propagate. As observed in the right panel of Fig. 5.1, there is a range for which the imaginary parts of both branches (4 and 5) are negative, which implies unstable growth. For $\xi > 10$, the two waves will continue to propagate and may exhibit some growth. However, they are not purely growing/unstable waves. As $\xi \to \infty$, the number density will decrease as $1/r$ leading to the decay.

5.1.3 Maximum temporal growth rates

Instabilities are best described by temporal rather than spatial growth rates. The imaginary part of the wave number can give a spatial growth rate, whilst the imaginary part of the frequency yields the temporal growth rate. In the inhomogeneous system considered here, a temporal growth rate cannot be directly determined. Briggs [57] demonstrates a way of obtaining the maximum temporal growth rate of an instability. The real and the imaginary parts of the wave numbers are mapped for varying frequencies and one investigates for any possible saddle points. The negative imaginary part of the frequency at the saddle point will then be the maximum temporal local growth rate.

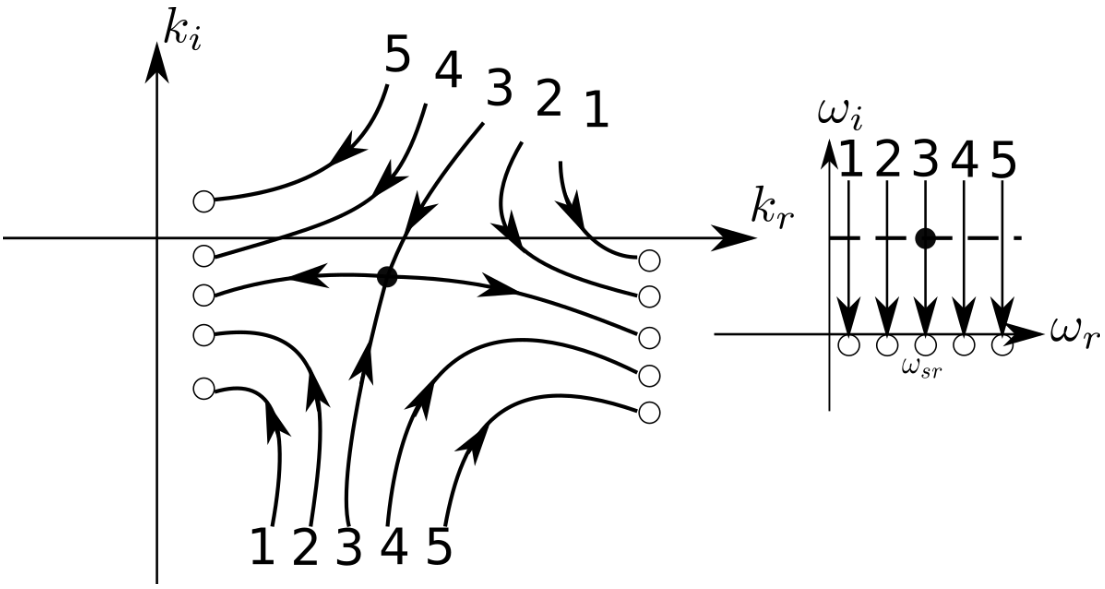

Figure 5.2: left panel corresponds to 5 different wave number mappings of their corresponding real and imaginary parts. The saddle point has been identified with a black dot. The right panel corresponds to the values of the frequency for a fixed real part and varying imaginary part.

From Fig. 5.2, one can observe where in k the local maximum temporal growth rate can be obtained. Fig. 5.1 can serve as a guide to investigate the unstable range and find growth rates by applying the mapping to wave numbers. Since the number density is explicitly dependent on position, one should investigate the range by iterating within the unstable range (for a fixed frequency), which is obtained from the analysis in Fig. 5.1. In this case, the range is $\xi = [1, 10]$. One starts by fixing the position and changing the frequencies. By mapping the complex frequency onto the real and imaginary parts of the radial wave numbers, one can find a saddle point [57]. In this analysis, a saddle point is found to be directly on the imaginary k_r axis implying that these modulations are purely in the azimuthal direction and this instability corresponds to the current filamentation instability. A saddle point with nonzero real part of k_r would correspond to an oblique instability as described above [107]. Since this is an inhomogeneous system with a radial dependence due to the geometry, the growth rate inherits a radial dependence. By following the same process presecribed above, we now iterate for radial positions.

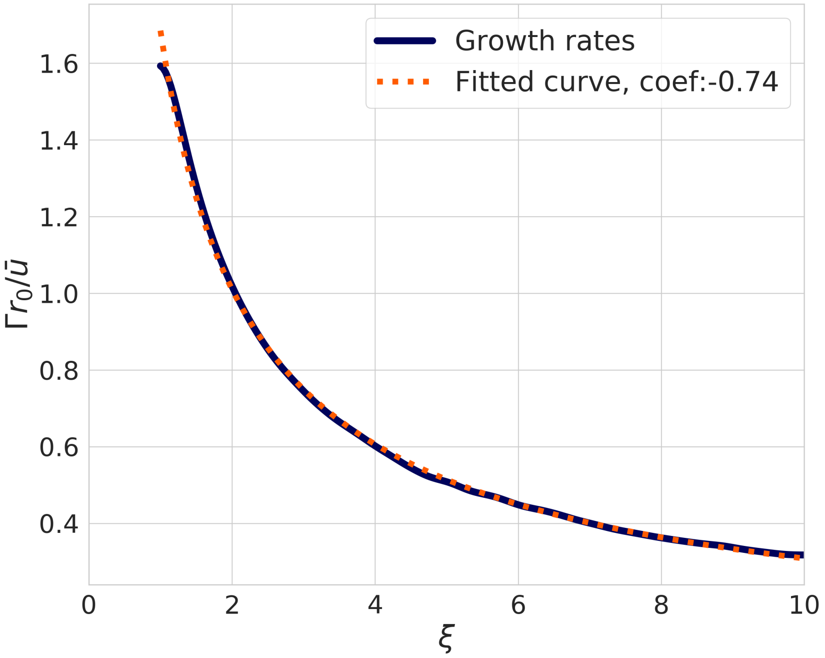

Figure 5.3: Maximum local temporal growth rates from the coalescing and bifurcating branches of k_r at varying radial positions (solid blue) and a fitted curve (dotted orange)

Fig. 5.3 clearly demonstrates a radial dependence of the temporal growth rate due to the inhomogeneous number density. By comparison, in the homogeneous slab geometry case, the growth rate is proportional to the plasma frequency. By extension, one can assume a direct contribution by the number density to the temporal growth rate in the inhomogeneous system described. However, as the local growth rate in this case is not proportional to the local plasma frequency, other effects must play a role.

5.1.4 Simulations

To demonstrate the validity of the analytical theory and the plausibility of streaming instabilities in a converging geometry, numerical simulations were performed. The PIC code `EPOCH` [33] is chosen to perform the simulations, which were set up to replicate the sheath at the back of the bubble. Due to numerical constraints, the simulation is restricted to two counter-streaming electron annuli. This results in considerable radial expansion of the bunches, which, in some cases, suppresses the instability. To counter this, for each annulus a homogeneous ion annulus is added co-propagating with their respective electron annuli. With neither ions nor initial fields, the electrons would oscillate around the neutralizing fields and would expand due to electrostatic repulsion. To seed the instability and investigate a clear signal, one of the annuli was given a sinusoidal modulation in the azimuthal direction with strength of 20%. Both annuli have the same number density at full overlap. To ensure both annuli have the same number density at full overlap, we set $n_+ = n_- A_- / A_+$ where $A_\pm$ are their areas, equal and opposite velocities corresponding to $\gamma = 2$, and an initial temperature of 0 eV. Both annuli have a width of 2.6 μm, and are separated from the outer of annulus 2 to the inner edge of annulus 1 by 5.6 μm. Initial electric and magnetic fields were added since `EPOCH` does not account for the initial fields for the premodulated annulus. The annuli have corresponding co-propagating ion annuli to avoid expansion and initial electric and magnetic fields are added explicitly since `EPOCH` assumes vanishing initial fields.

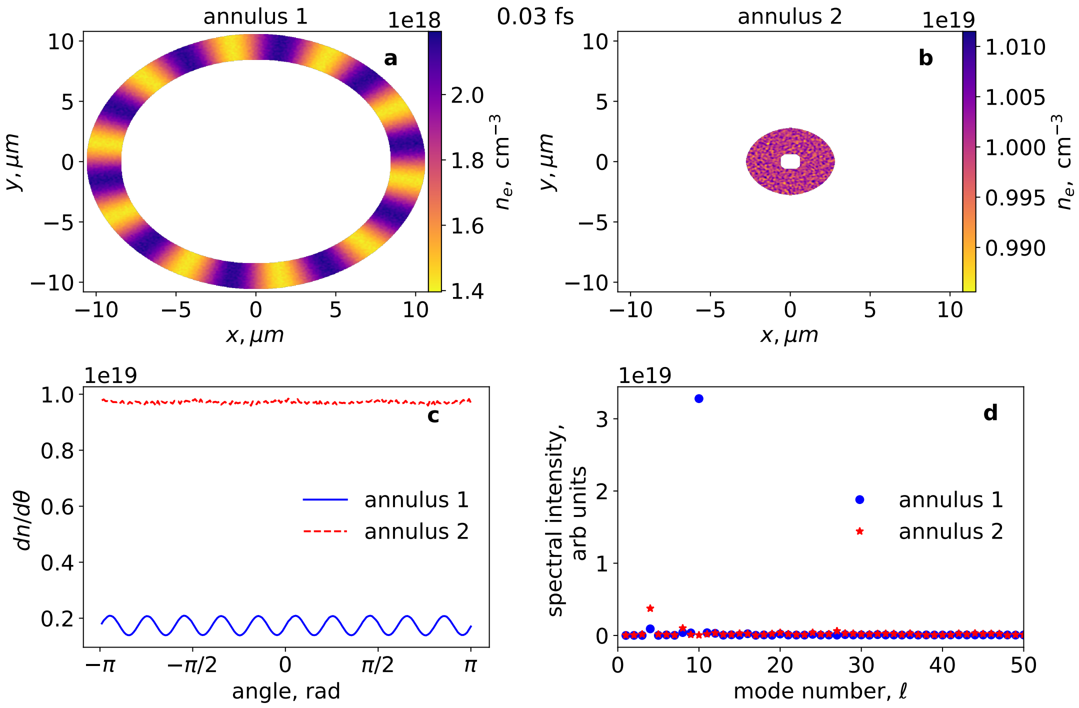

Figure 5.4: Initial number density for the initially modulated annulus (**a**), number density of the initially unmodulated annulus (**b**), azimuthal dependence of number density (**c**), and spectral amplitude (**d**).

Fig. 5.4 shows the initial setup of the simulation. In the following timesteps, the annuli approach each other without interacting. As the annuli begin to overlap, there is no discernible distinction to the initial fast Fourier transforms of the azimuthal dependence of the number density (signals), but as they fully overlap, a modulation develops in the initially unmodulated bunch. The spectral intensity of the azimuthal number density demonstrates a faster growth at full overlap and a slowing down after full overlap in annulus 2. Annulus 1 demonstrates a decrease in the decay rate and the rate continues to decay as the annulus shrinks. The decay in the spectral intensity can be attributed to electrons repelling each other due to the area of the annulus shrinking. Thus, the electrons would most likely repel and decrease the modulation depth.

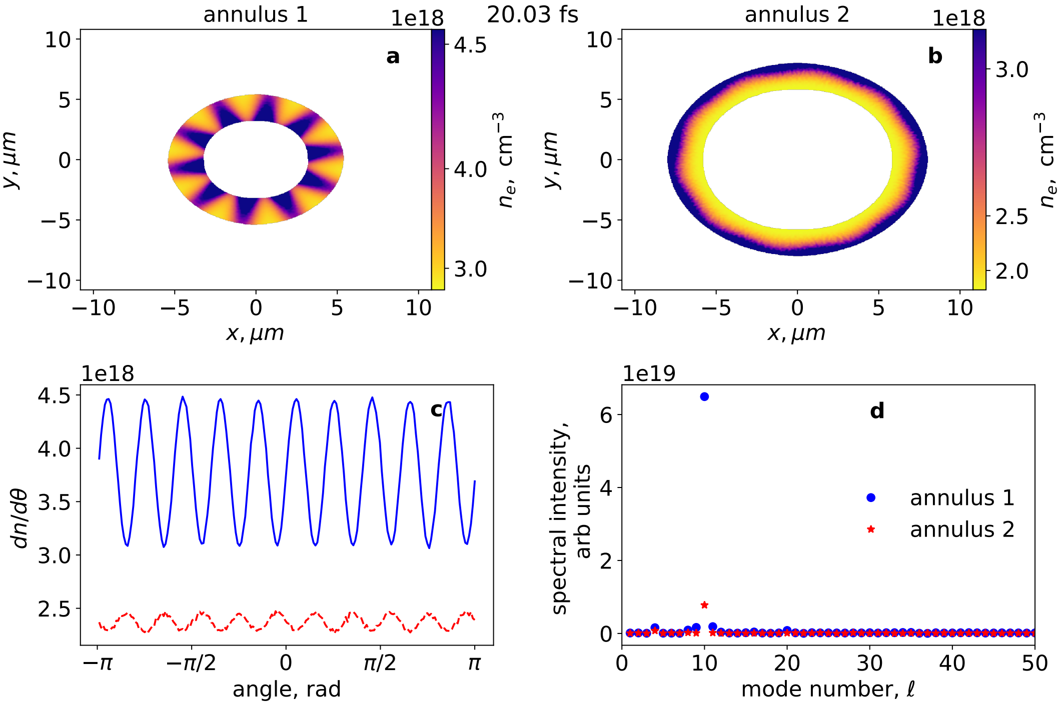

Figure 5.5: As Fig. 5.4, but at time 20.03 fs.

Fig. 5.5 clearly shows a modulation present in annulus 2 and the modulation still present in annulus 1. 20.03 fs is after the complete overlap and interaction of both annuli. The azimuthal number density of annulus 2 is π out of phase with the modulation from annulus 1 and their corresponding spectral intensities demonstrate a peak at $\ell = 10$. To discard any artificial growth, simulations using a single annulus are performed and compared with the results for interacting annuli. In the case for the unmodulated annulus, no modulations developed.

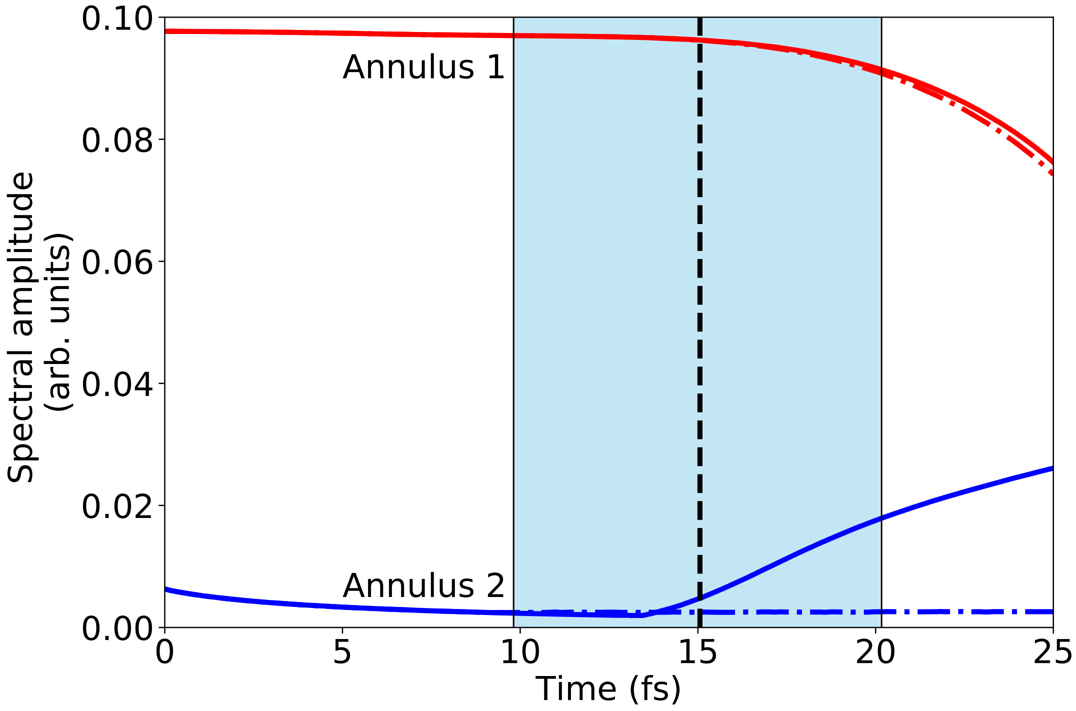

Figure 5.6: Evolution of the spectral amplitude at $\ell = 10$ for annulus 1 (red) and annulus 2 (blue). The solid lines correspond to the simulation with interaction and the dot-dashed to the single annulus simulations. The light blue shade corresponds to the period of interaction of both annuli with the black dashed line being the timestep at full overlap.

As Fig. 5.6 shows, for annulus 1, the decay rate is decreased when there is interaction but is still dominated by the repulsion of the electrons as the annulus shrinks.

The current filamentation instability can couple to “pure” (temperature driven) Weibel unstable modes [64]. In order to avoid any confusion and to check for numerical heating, the temperature of the bunches determined from the simulation data, using a definition by Schroeder et al. [51] to be 30 meV. At this temperature, the annuli can be considered cold, and coupling to “pure” Weibel instabilities are unlikely.

Simulations where the initially modulated ring are moving outward were also performed and demonstrated to have a simular outcome. Again, the modulation is present in the initially homogeneous ring after interaction. Equally, in a number of simulations for larger mode numbers, the modulation develops in the initially unmodulated annulus.

5.1.5 Discussion

Having determined the growth rates using the semi-analytical theory and the simulations, the next step is to compare them. To calculate the total growth rate, a simple assumption is that the modulations in each ring drive the growth in the other one. This is described by the equation [107]

$$\frac{d}{dt}(S_+ + S_-) = \Gamma(S_+ + S_-), \tag{5.22}$$

where $S_\pm$ corresponds to the signal for the respective annuli and Γ is the growth rate.

Fig. 5.7 shows a comparison of the growth from the semi-analytical predictions, a local approximation for the current filamentation, and the simulations. The local approximation uses the equation for the growth rate for the CFI in a cold relativistic homogeneous plasma [111]

$$\Gamma_{\mathrm{CFI}} = \left[\left(\frac{\mathcal{C}^2}{4} + \frac{2u^2k^2\omega_p^2}{\gamma}\right)^{1/2} - \frac{\mathcal{C}}{2}\right]^{1/2}, \tag{5.23}$$

where $\mathcal{C} = \left(2\omega_p^2/\gamma^3 + k^2c^2\right)$. In Eq. 5.23 the plasma frequency and wave number are replaced by their local values, $\omega_p = \sqrt{e^2\bar{n}(r)/(m\epsilon_0)}$ and $k = 2\pi\ell/r$. The red triangles correspond to further simulations at larger r and obtained at the respective positions of full overlap, and the dot-dashed line is a fit to these points. The fitted curve nicely demonstrates the scaling dependence on the number density that corre-

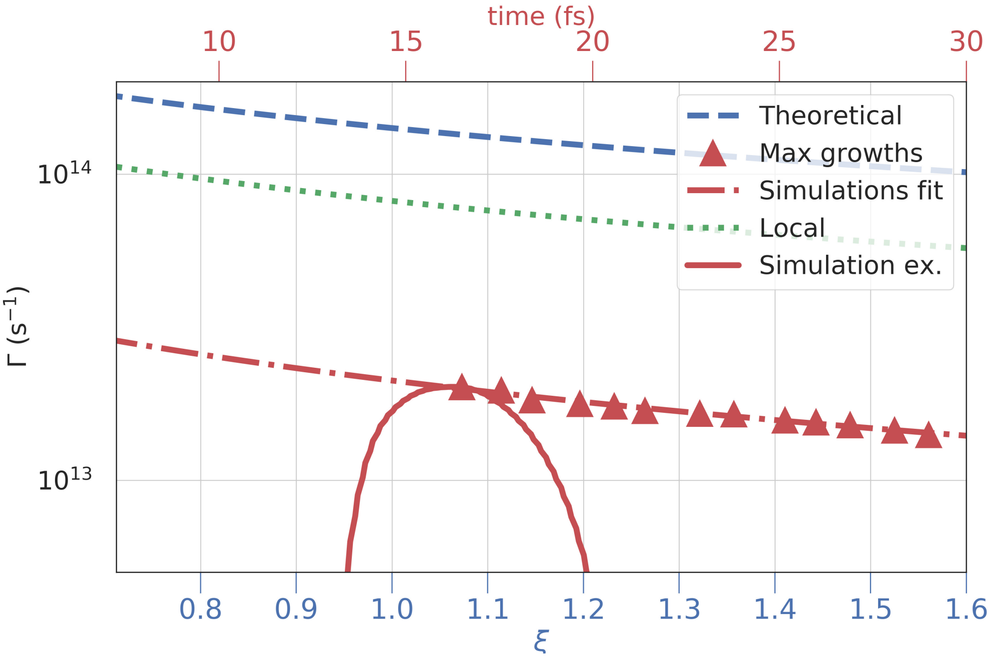

Figure 5.7: The predicted local maximum temporal growth rate (dashed) compared with the growth rates of a simulation of full overlap at $r_0 = 5.6\,\mu$m (solid), the maximum growth rates of simulations with overlap at different positions (triangles) and the local approximation (dots). The dot dashed line represents a fit to the growth rates from simulations at different complete overlap positions.

sponds to $\Gamma_{\text{sim}} \propto \xi^{-0.88}$, where the theoretical predictions have a scaling dependence of $\Gamma_{\text{s-a}} \propto \xi^{-0.7}$. The local growth rate has a scaling dependency of $\Gamma_{\text{local}} \propto \xi^{-0.75}$.

A comparison was made to observe if resonance between the local growth rate of the TSI and the CFI could occur, i.e., the growth would be the same at the same position. However, the growth rates do not overlap at any time during the interaction of the bunches, thus discarding possibility of resonance between TSI and CFI.

The semi-analytical theory does prescribe an upper limit to the growth rate. Equation 5.22 does not consider inertial effects occurring in the interactions. The inertial effects are seen that the largest growth Fig 5.7 shows how there is a delay between the response of the annuli and overlap. Simulations with larger rings may yield a closer agreement between the semi-analytically predicted growth rates as the annuli would interact for a longer period of time. However, the growth rates predicted by our semi-analytical model agree almost one order of magnitude to the growth rate inferred from the simulations. Both growth rates exhibit similar scaling dependences due to the number density's spatial dependence on radial position.

5.2 Warm Background Plasma

5.2.1 Semi-analytical approach

Although a cold plasma approximation appears reasonable, in reality, plasma can have an initial temperature. As described in chapter 3, section 5, Jia *et al.*[65] demonstrate in their paper that a temperature in the background plasma has an effect on the growth rates of the current filamentation instability [65]. Warm plasmas are ubiquitous in space and laboratories, ranging from stars, to inertial and magnetic confinement fusion. In the current filamentation instability, a transverse momentum spread can completely suppress the instability [4, 65].

Naturally, the cold plasma approach we have used in the previous section of the chapter can be expanded by adding a non-zero pressure term in the momentum equation,

$$(\partial_t + \boldsymbol{u} \cdot \boldsymbol{\nabla})\tilde{\boldsymbol{p}} = -e(\tilde{\boldsymbol{E}} + \boldsymbol{u}_{0,\pm} \times \boldsymbol{B}) - \nabla \tilde{P}_{\pm}/\bar{n}. \tag{5.24}$$

Approximating the perturbed pressure $\tilde{P}_{\pm}$ as isotropic, its gradient can be expressed (in two dimensions) as $\nabla \tilde{P} = 2k_B T \nabla \tilde{n}_{\pm}$, where T is temperature. The approach described in the previous chapter can be utilized to obtain a set of coupled, linear, ordinary differential equations. The new set of equations adopt the following form:

$$\frac{\mathrm{d}}{\mathrm{d}\xi}\mathcal{N}\pm = \left(\pm i\Omega - \frac{1}{\xi}\right)\frac{\mathcal{N}_\pm}{\mathcal{P}} \mp \frac{i\ell}{\mathcal{P}\xi^2}\mathcal{U}_{\theta,\pm} + \frac{1}{\mathcal{P}\xi}\left(\frac{\mathcal{E}_r}{\gamma^3} - i\Omega\mathcal{U}_{r,\pm}\right), \tag{5.25}$$

$$\frac{\mathrm{d}}{\mathrm{d}\xi}\mathcal{U}_{r,\pm} = \mp\frac{\mathcal{E}_r}{\gamma^3} \pm i\Omega\mathcal{U}_{r,\pm} \mp \frac{\mathcal{T}\xi}{\gamma^3\mathcal{P}}\left[\left(\pm i\Omega - \frac{1}{\xi}\right)\mathcal{N}_\pm \mp \frac{i\ell}{\xi^2}\mathcal{U}_{\theta,\pm} + \frac{1}{\xi}\left(\frac{\mathcal{E}_r}{\gamma^3} - i\Omega\mathcal{U}_{r,\pm}\right)\right], \tag{5.26}$$

$$\frac{\mathrm{d}}{\mathrm{d}\xi}\mathcal{U}_{\theta,\pm} = \mp\frac{\mathcal{E}_\theta}{\gamma} + \frac{\mathcal{B}_z}{\gamma} \mp i\ell\mathcal{T}\mathcal{N}_\pm \pm i\Omega\mathcal{U}_{\theta,\pm}, \tag{5.27}$$

$$\frac{\mathrm{d}}{\mathrm{d}\xi}\mathcal{E}_r = -\Omega_p^2(\mathcal{N}_+ + \mathcal{N}_-) - \frac{i\ell\mathcal{E}_\theta}{\xi} - \frac{\mathcal{E}_r}{\xi}, \tag{5.28}$$

$$\frac{\mathrm{d}}{\mathrm{d}\xi}\mathcal{E}_\theta = i\Omega\mathcal{B}_z + \frac{i\ell}{\xi}\mathcal{E}_r - \frac{\mathcal{E}_\theta}{\xi}, \tag{5.29}$$

$$\frac{\mathrm{d}}{\mathrm{d}\xi}\mathcal{B}_z = i\Omega\beta^2\mathcal{E}_\theta + \frac{\beta^2\Omega_p^2}{\xi}\left(\mathcal{U}_{\theta,+} + \mathcal{U}_{\theta,-}\right). \tag{5.30}$$

Where $\mathcal{T} = 2k_BT/(u^2m_e)$ and $\mathcal{P} = 1-\mathcal{T}/\gamma^3$. The thermal velocity can be identified as $\sqrt{k_BT/m_e}$. At $T = 0$, the equations (5.25) to (5.30) reduce back to equations (5.15) to (5.20). The equations can also be written in the form of equation 5.21, and furthermore for $\ell = 0$, this should yield a description of the TSI for a warm plasma. The eigenvalues for this set of equations are obtained in the way described in the previous section. They also exhibit coalescence and bifurcation of the real and imaginary parts of the wavenumber k_r. Repeating the same process as before, the maximum temporal growth rate can be obtained by mapping the real and imaginary parts of the wave numbers to complex frequencies.

In the homogeneous case with a finite temperature, the range of wavenumbers that yield an instability decreases, which implies that the range of modes also decreases, as $k = 2\pi\ell/r_0$. Electrons with a higher temperature will not filament into structures with high mode numbers, since they are more difficult in confine to a small region. Electrons with sufficiently high temperature will be able to escape the pinching effect of the magnetic fields, while for lower modes, the magnetic fields are strong enough to restrain the electrons from escaping the filaments due to the larger volume. The pinching magnetic field grows with the filament size, while the pressure gradient grows with the decrease of the filament size. The growth rate of the instability in warm plasma can be calculated in a similar way to the case of cold plasma (see chapter 3, section 5).

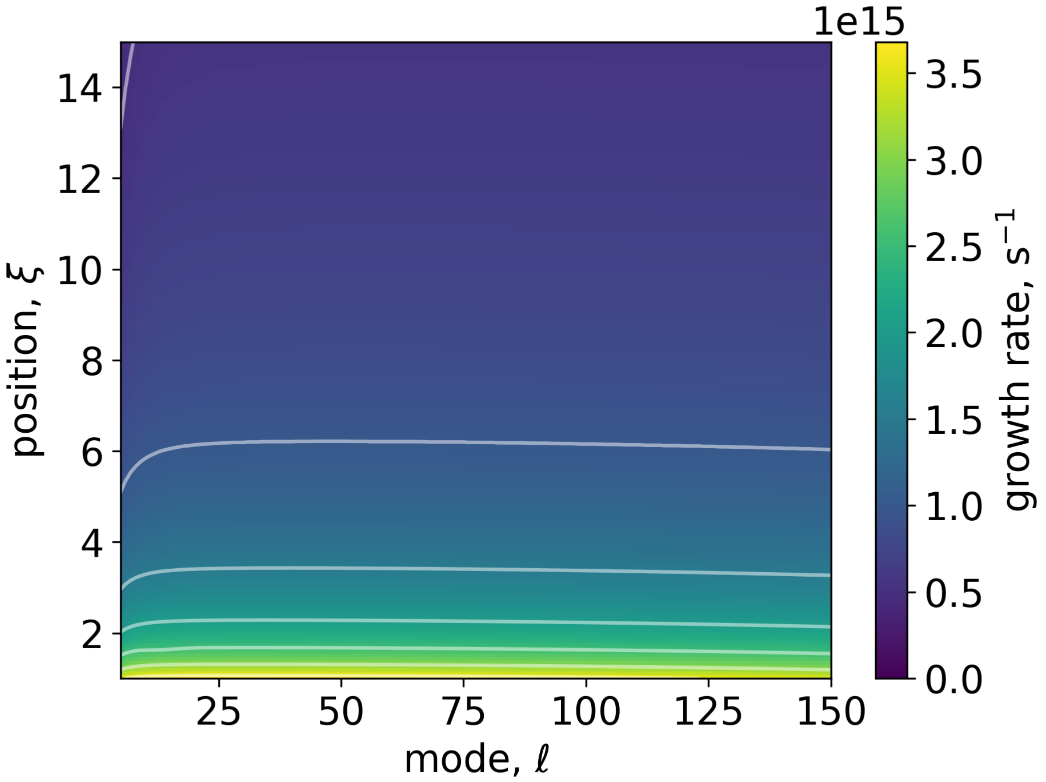

Figure 5.8: Growth rate as a function of position ξ and mode number ℓ for a temperature of 1000 eV.

The growth rate as a function of position and mode number shown in Fig. 5.8 decreases for larger ξ, and decreases for larger mode numbers. In the context of the back of the LWFA bubble, this implies that if instabilities do occur, they would be strongest near the axis due to the larger number density, and will most likely imprint a lower mode number into the azimuthal filaments in the particles ejected as side electrons. At low temperatures, the coalescence and bifurcation of the real and imaginary parts demonstrate similarities to the cold case but as the temperature increases, the growth rate decreases. As in the slab geometry case, one would expect that as the plasma temperature increases, the growth rates decrease more drastically. However, the model has a shortcoming at large temperatures where the saddle point disappears at a large temperature without the growth rate tending to zero.

5.2.2 Simulations

Temperature dependence

Simulations have been performed using `EPOCH` to compare with the above theoretical analysis. These simulations are set up with different initial temperatures to study the effects of temperature in the CFI. The simulations use the same initial parameters as in the previous section, but with a larger number density of $n = 3 \times 10^{19}\,\mathrm{cm}^{-3}$ at full overlap. However, in these simulations, a range of temperatures is used, where we will show the simulations for 100 eV, 1 keV, and 10 keV. As the simulations progress, each demonstrates a different outcome. The initial setup is the same as for Fig. 5.4 because the temperature effects have no immediate observable effect at the beginning of the simulation.

Figurs 5.9-5.11 demostrate the outcome of the simulations with an initial finite temperature. As the simulations progressed, each demonstrates a different outcome. For

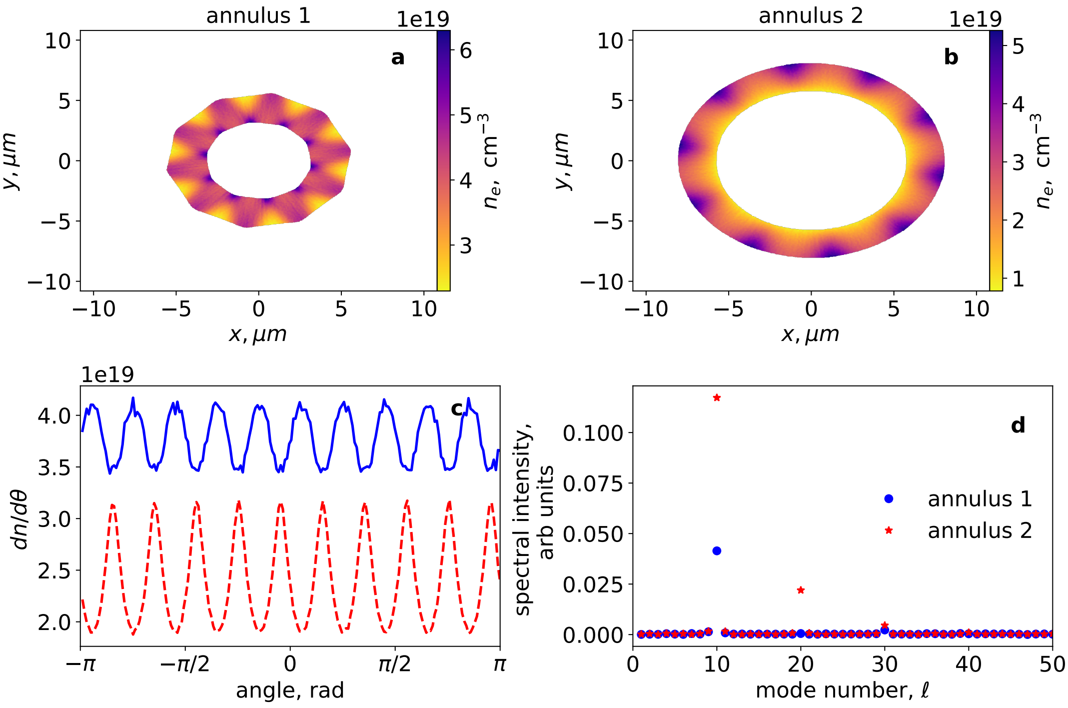

Figure 5.9: Same layout as Fig. 5.4 but with an initial temperature of 100 eV at the initial timestep of the simulation

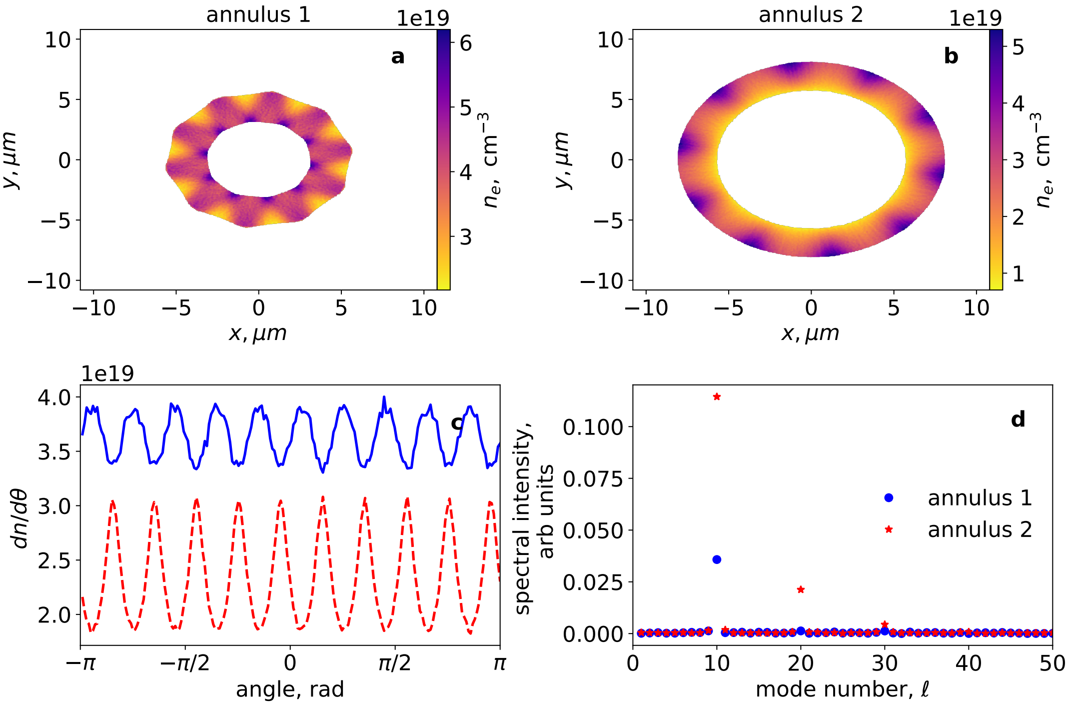

Figure 5.10: Same layout as Fig. 5.4 but with an initial temperature of 1 KeV at the initial timestep of the simulation

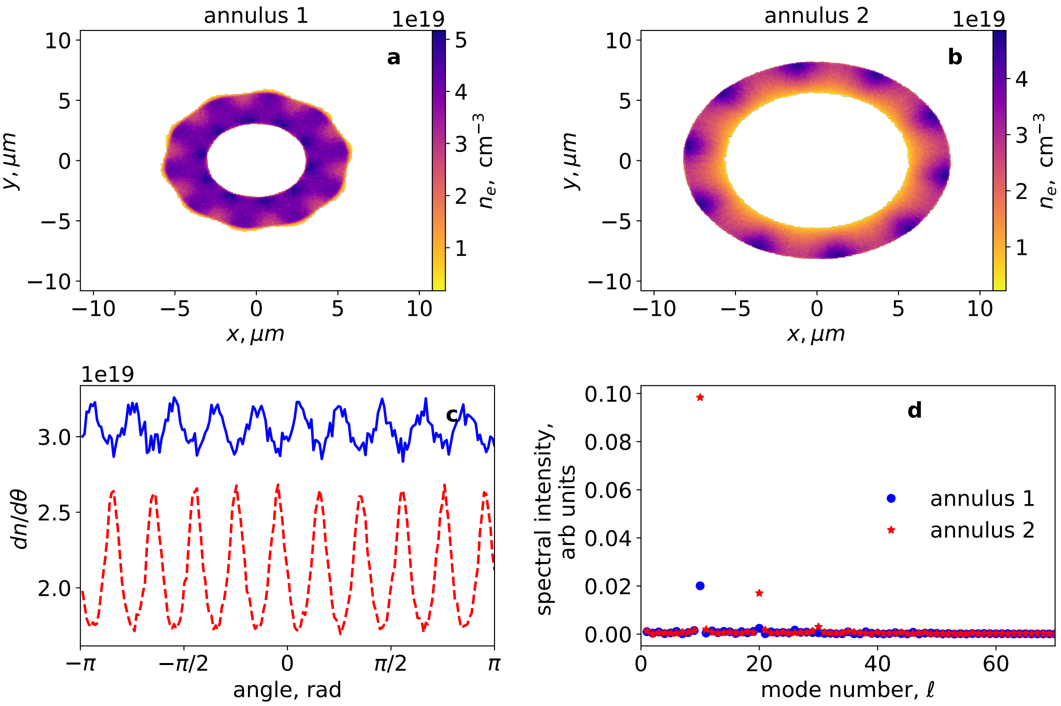

Figure 5.11: Same layout as Fig. 5.4 but with an initial temperature of 10 keV at the initial timestep of the simulation

the colder simulations, the instability develops as for the cold case presented previously. For the 1 keV case, the instability developes slower than in the 100 eV case (smaller growth rate). At 10 keV, the electron annuli still demonstrate some growth but on closer inspection demonstrates that the annuli have expanded and the initial modulation has been suppressed.

Mode Dependence

Since the mode number determines the scale of the modulations in a similar way to a transverse wave number, and in a homogeneous system with finite temperature, the dependence of the temporal growth rate on the wave number shows a maximum mode number, or range of modes can be expected to yield the largest growths. `EPOCH` simulations are performed for a fixed temperature in both electron species and varying the mode numbers. Intervals of 5 are chosen unless that number is a multiple of 4 to avoid an artificial growth caused by the Cartesian grid. We use the same setup as before. The fields in this case impose a limitation because they have a r^ℓ dependence and the upper limit using `EPOCH` is proved to be $\ell = 59$. Similarly, as in the previous subsection, a number density of $n = 3 \times 10^{19}\,\mathrm{cm}^{-3}$ at full overlap is used and an initial temperature of 1 KeV is used

Figures. 5.12 to 5.17 show the initial and final timesteps of the simulations for the initial modulations $\ell = 15, 25$ and $\ell = 50$. In the initial timesteps, the different modes are observed in the initially modulated annulus. As in the previous sections, the annuli are designed to counterstream and represent a small section of a much larger stream of electrons counterflowing in a converging geometry.

The instability begins to develop as the counterstreaming annuli overlap. In the case for lower mode numbers, the instability develops quickly and has its maximum growth rate soon after fully overlapping due to the inertial effects. As they have fully overlapped and begin to exit one another, the growth rate decreases and the instability ceases to exist. The case $\ell = 15$ exhibits the largest growth rate of the three represented simulations. From the simulations, larger mode numbers took longer to initiate developing the instability.

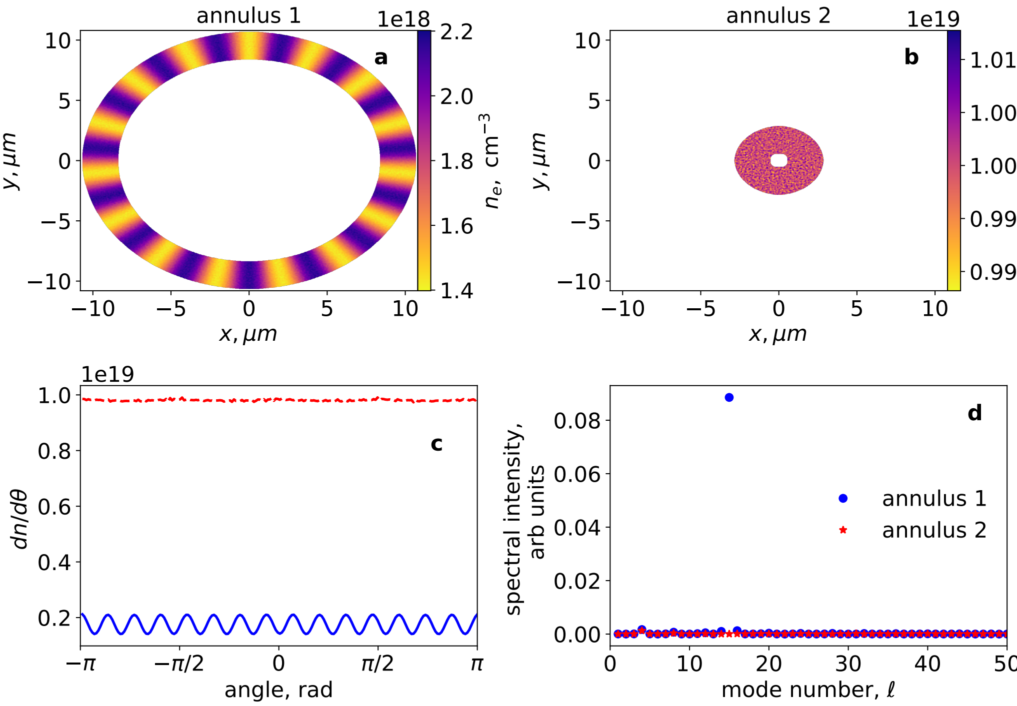

Figure 5.12: Same layout as Fig. 5.4 but for an initially modulated annulus with mode number $\ell = 15$ at the initial timestep of the simulation

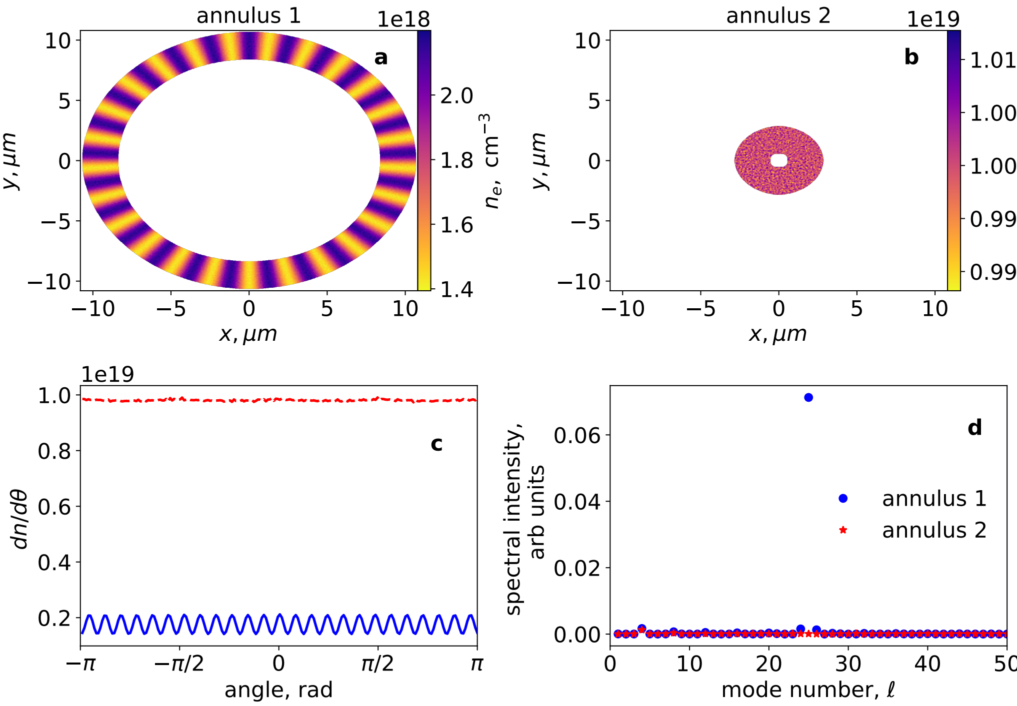

Figure 5.13: Same layout as Fig. 5.4 but for an initially modulated annulus with mode number $\ell = 25$ at the initial timestep of the simulation

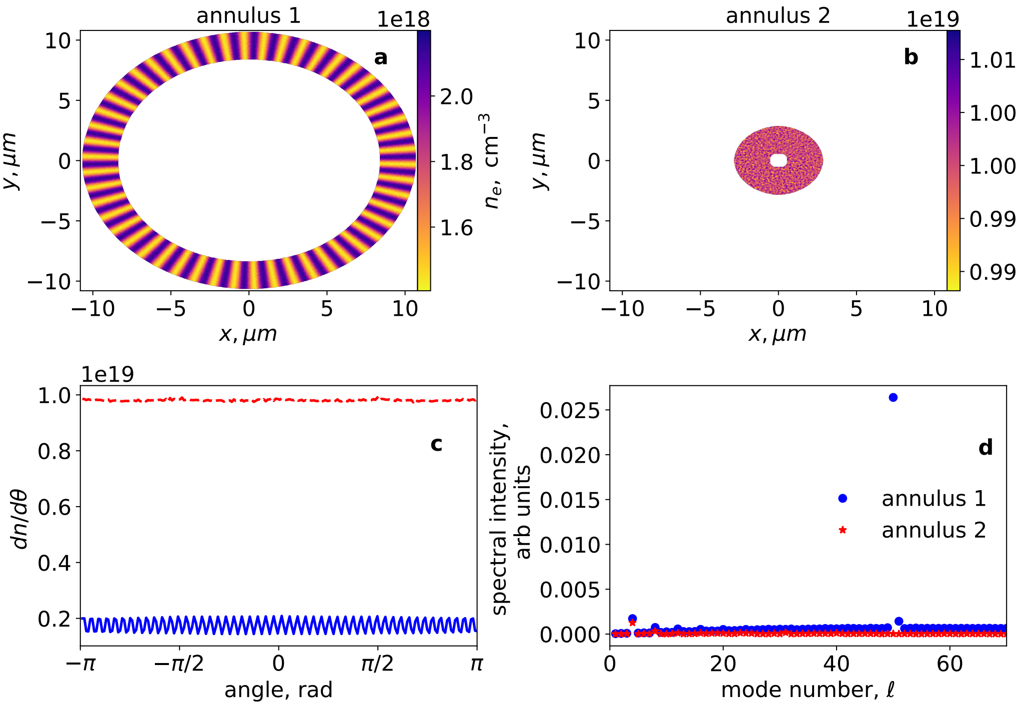

Figure 5.14: Same layout as Fig. 5.4 but for an initially modulated annulus with mode number $\ell = 50$ at the initial timestep of the simulation

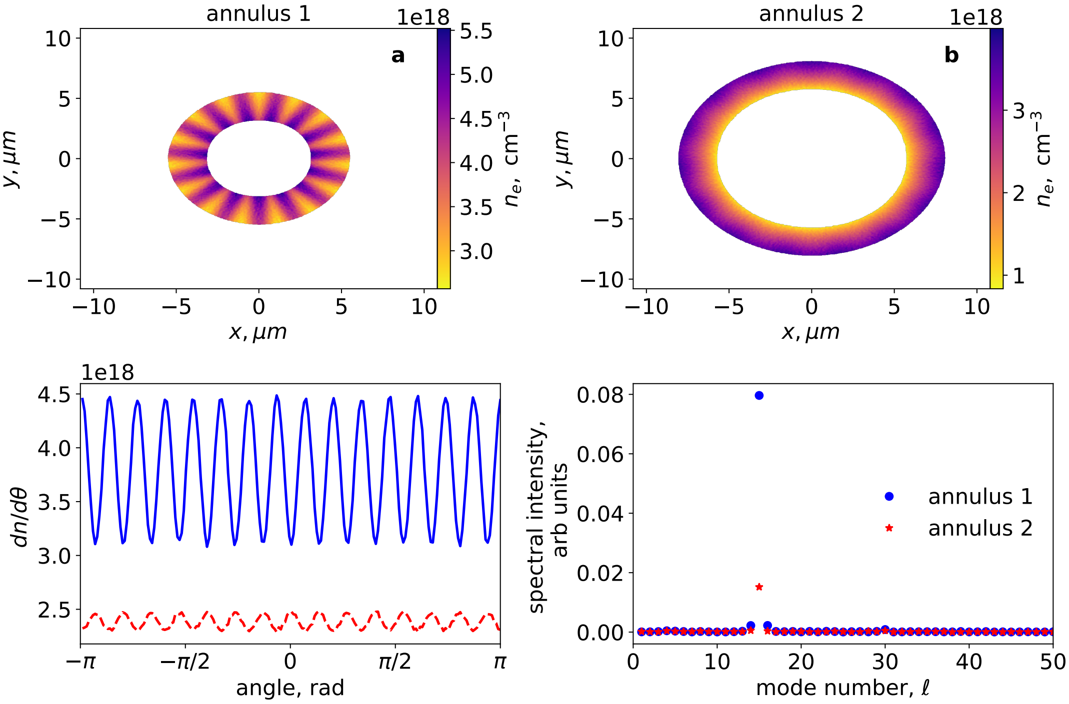

Figure 5.15: Same layout as Fig. 5.12 but at timestep = 20 fs.

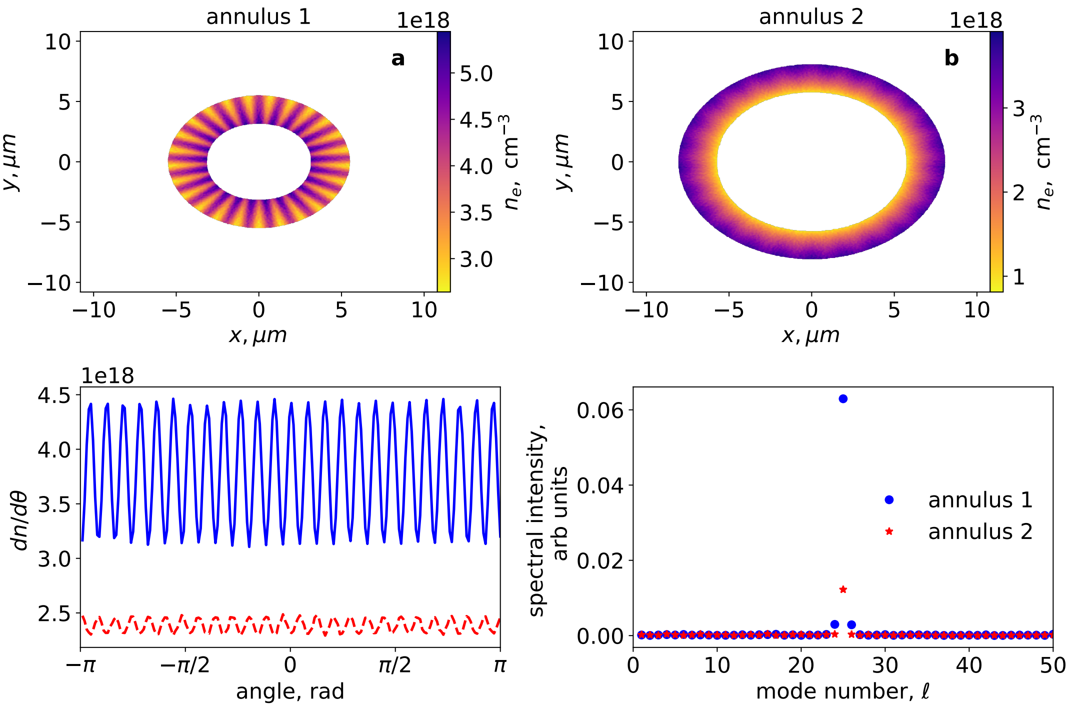

Figure 5.16: Same layout as Fig. 5.13 but at timestep = 20 fs.

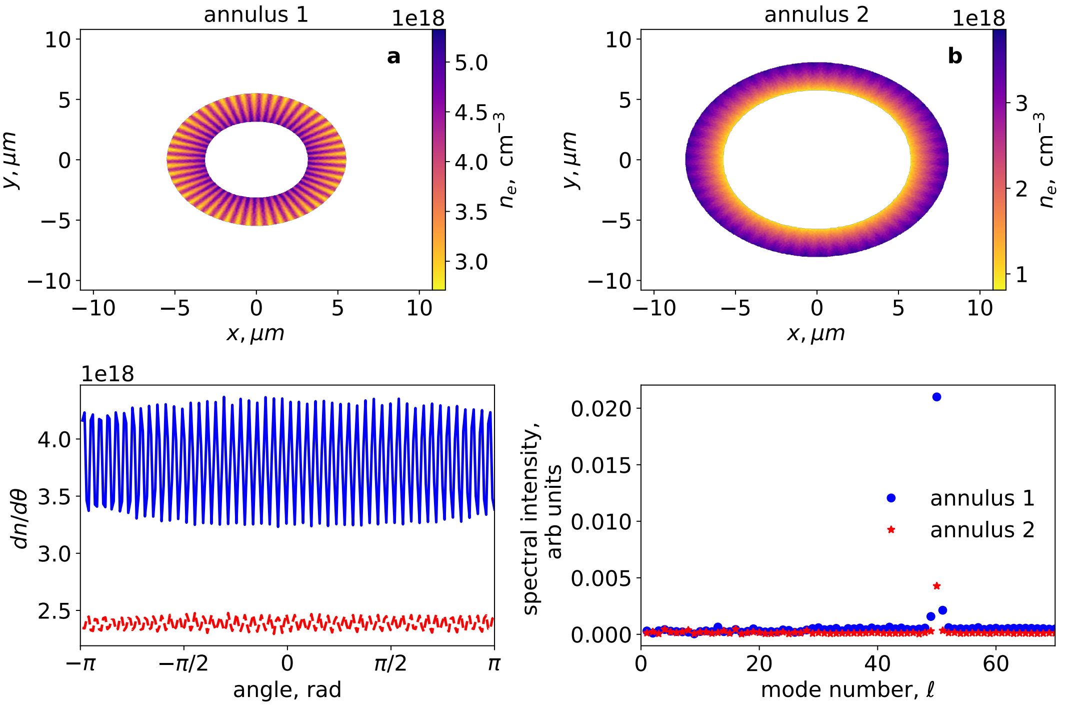

Figure 5.17: Same layout as Fig. 5.14 but at timestep = 20 fs.

5.3 Discussion

5.3.1 Temperature Dependence

As shown in the previous section, similarly to what can be observed in the slab geometry/homogeneous case, the temperature is able to weaken and ultimately suppress the current filamentation instability in a converging geometry.

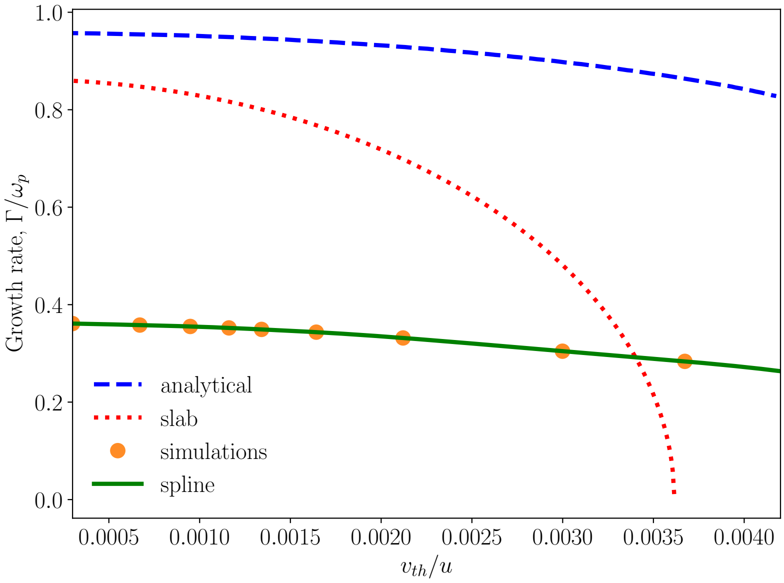

Figure 5.18: Growth rate as a function of temperature from the analytical predictions (dash blue), the growth rate from the slab geometry as a function of temperature (dash red) inferred growth rate from the simulations (orange dots), a spline fitting the inferred growth rate from the simulations (solid green).

Figure 5.18 shows the growth rates inferred from the simulations using Eq. (5.22) and calculated from the semi-analytical analysis as a function of temperature. For comparison, the temperature dependence for a homogeneous system is also shown. Figure 5.18 demonstrates an agreement of the scaling with the converging geometry. While a quicker suppression of the instability is predicted for slab geometry, the simulations demonstrate growth extending to higher temperatures. The inferred growth rates and the semi-analytical predictions also agree in the temperatures at which the instability disappears. The model has a shortcoming at higher temperatures, where it fails to provide a qualitative description of the decrease in growth rate and yields a sudden disappearance of the saddle point representing the maximum local temporal growth rates. Lower number densities have a larger discrepancy with the semi-analytical predictions. The study can be continued to provide a more accurate description of the instability at higher temperatures.

Mode Dependence

The slab geometry and the semi-analytical theory for a converging geometry with a fixed initial temperature predict that the growth rates decrease and the instability is suppressed at large mode numbers. In slab geometry, the range of unstable modes is smaller than in converging geometry. Using Eqn. (5.22), we can calculate the growth rates from the simulations.

Fig. 5.19 demonstrates a faster decay in growth rate from the simulations than in the semi-analytical predictions. From the simulations it can be inferred that the rings required a longer overlap before the instability develops. The simulations demonstrate a peak at approximately $\ell = 7$, which is similar to the slab geometry results but not the semi-analytical predictions. The simulations demonstrate a decrease as the mode number is increased. The semi-analytical predictions reach a maximum at 41 marked with an x in Fig. 5.19. The behaviour of the growth rates inferred from the simulations agree with the semi-analytical predictions to some extent.

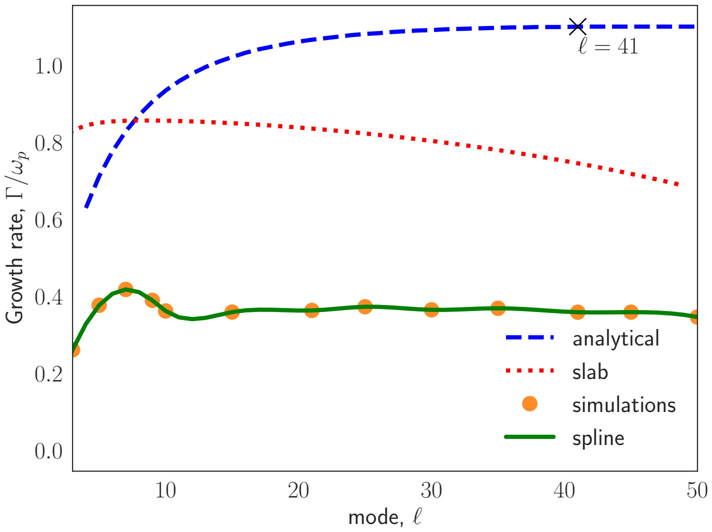

Figure 5.19: Semi-analytically predicted growth rates for varying mode number (dashed blue line), local approach using a slab geometry (dashed red), growth rates inferred from simulations with different initial modulation (orange dots) with a fitted spline (solid green line)

5.4 Conclusions

In this chapter, we have developed a theory to describe instabilities in a converging geometry. An analytical description for a cold, inhomogeneous and relativistic plasma is developed. Using the continuity, momentum and Maxwell's equations, we've obtained a set of coupled, linear differential equations that can be treated as an eigenvalue problem. A WKB approximation is used to approximate wave numbers. The eigenvalues of the system are solved for, and the corresponding wave numbers obtained. By mapping the real against the imaginary parts of the wavenumbers, we are able to obtain the maximum local temporal growth rates of the instability. The growth rates inherit a spatial dependence from the electron number density. PIC simulations have been performed to support the semi-analytical descriptions with two counter-streaming electron annuli representing a small fraction of a continuous converging/diverging stream of electrons where one annulus is initially modulated whilst the other one is unmodulated where, in practice, the modulations will arise from random fluctuations instead of a seed. After the annuli interact, the initially unmodulated annulus demonstrates a sinusoidal azimuthal modulation π out of phase to the initially modulated annulus. The corresponding growth rate is calculated and agrees well with the semi-analytical description. Expanding from the cold plasma approach, a pressure term with an isotropic temperature distribution is added to the momentum equation. A modified set of coupled, linear ordinary differential equations is obtained that can be scaled down to the cold plasma by setting the temperature to zero. The maximum temporal growth rates are obtained in the same way as for the cold case and the growth rates exhibit a dependence on position as well as mode number ℓ and temperature. It is found that positions further away from the axis and large mode numbers will yield smaller growth rates. PIC simulations are performed to support the semi-analytical theory with the same setup as in the cold case. Increasing the temperature reduces the growth rates in a similar scale with the semi-analytical approach and can completely suppress the instability.

In addition to varying the temperature for a fixed mode number, the mode number dependence is also studied, which demonstrates that larger mode numbers decrease the instability growth rates in the simulation. The study can be expanded by investigating temperature anisotropies to compare the analysis done by Jia *et al* [65]. Furthermore, a more rigorous examination using methods presented by Schroeder and Esarey [51] can be used to obtain a more accurate description of the thermal effects in a converging geometry. Also, the study can be expanded by making the system time-dependent and solving numerically in space and time.

Chapter 6

Particle Dynamics at the back of the LWFA bubble

6.1 Introduction

Experiments presented in chapter 4 demonstrated evidence of azimuthal striations of electrons as ejected from the LWFA [83]. These are evidence of the current filamentation instability [4, 61, 62]. To explore the origin of them, we investigate the trajectories and particle dynamics of the “side electrons”. Full 3D PIC and quasi 3D PIC simulations have been performed with particle tracking enabled. From the electron trajectory, we then develop a reduced model that interprets the electron interactions at the back of the LWFA bubble. Then, reduced 2D simulations are performed in the form of counterstreaming annuli and counterstreaming slabs. This chapter provides a simulation-based description to add interpretation of the experimental results described in chapter 4 combining the theory presented in chapter 5.

6.2 3D simulations

To model the experiments, quasi-3D simulations using `FBPIC` [100] and 3D simulations using `OSIRIS` [112] are performed to visualize side electrons. The `OSIRIS` simulations have a resolution of $14 \times 20\,\mathrm{nm}$, $a_0 = 3, w_0 = 7$, a density of $2 \times 10^{19}\,\mathrm{cm}^{-3}$, 4 particles per cell and an initial temperature of $0\,\mathrm{eV}$. While the simulations agree with measurements from experimental results on emitted charge [113], the spatial distribution of the side electrons do not show evidence of striations. Initial analysis of the `OSIRIS` simulations do demonstrate very fine azimuthal modulations in the radial momenta of the particles ejected as side electrons. However, as an initial electron temperature spread is increased to the electrons (while maintaining all the other parameters fixed), the azimuthal modulations quickly disappear. The sheath electrons are investigated to determine if a modulation can arise after crossing or "bouncing" from the back of the LWFA bubble which could explain if instabilities occur.

In Fig. 6.1, we show the azimuthal modulations by taking the azimuthal distribution of the number density and the azimuthal distribution of the radial momenta at the back of the bubble. Figure 6.1 (**d**) and (**f**) do not show any evidence of growth or striations after interaction. The simulations demonstrate a homogeneous electron distribution along the transverse plane which implies there are no modulations. A fast Fourier transform (FFT) of the azimuthal number density calculated from `FBPIC` and `OSIRIS` data at different timesteps and different longitudinal positions reveals that no predominant mode or azimuthal structure is present in the number density or radial momenta. One explanation for this is that the resolution is too low. However, a fine

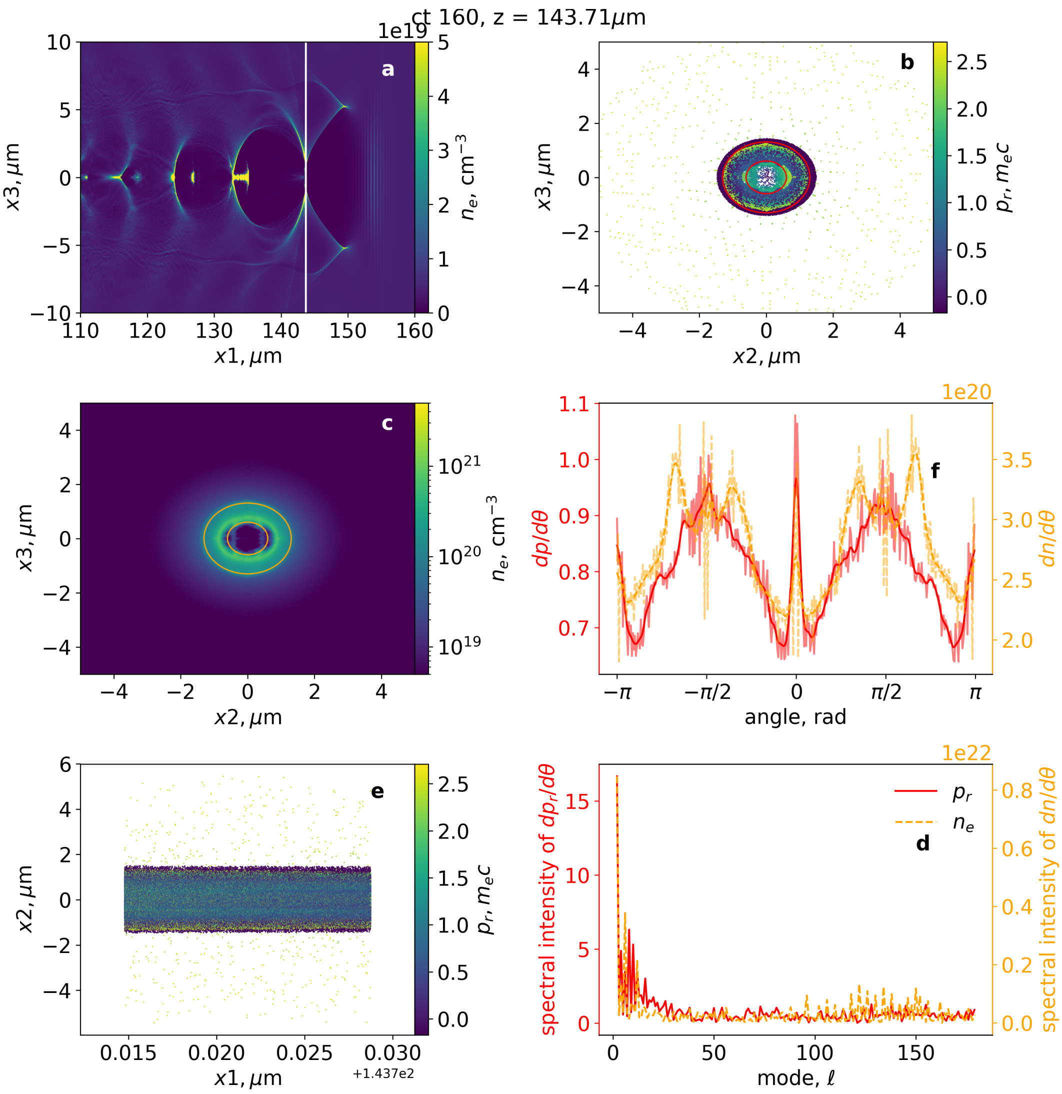

Figure 6.1: (**a**) Electron density in the longitudinal plane with a vertical line denoting the position where information is obtained from. (**b**) Particle position in the transverse plane coloured by their radial momentum with a red annulus corresponding to the selection of particles to be analyzed. (**c**) Number density in the transverse plane corresponding to the lineout in part (**a**). (**d**) Radial density in the azimuthal direction and number density in the azimuthal direction. (**e**) Scatterplot of the lineout. (**f**) Fast Fourier transform. x_1, x_2, and x_3 correspond to the transverse coordinates and x_3 to the longitudinal coordinate.

resolution does not exhibit the microstructures. An even higher resolution simulation requires more resources, the PIC code `FBPIC` has a limitation on the observation of azimuthal striations due to the number of azimuthal mode numbers in the simulations. Each extra mode increases the amount of resources utilized in GPUs. This quasi-3D simulation allowed for up to 3 modes (modes 0,1 and 2). Also, increasing the azimuthal modes higher than 6, leads to numerical instabilities.

We have explored options that could potentially yield a description for the azimuthal striations present in the side electrons. An example of the explanation would be the interaction of the side electrons with the background plasma. However, the density of the background plasma and the outgoing beam would yield a an instability with a very low growth rate. We present an plausible explanation of the origin of the striations present in the side electrons by investigating the dynamics of electrons at back of the bubble and counterstreaming electron flows. The back of the bubble has a very large number density (near critical density) because particles converge on-axis and can yield sufficiently high growth rates for instabilities to occur. This requires a thorough understanding of the particle trajectories at the back of the bubble.

6.3 Electron trajectories and dynamics

Side electrons are first displaced from their initial positions in the plasma due to the ponderomotive force of the laser pulse, and drawn back by the electrostatic fields of the ions, which form the sheath of the bubble. A common misconception is that all the electrons forming the sheath cross at the rear of the bubble [18, 28]. Particles with sufficient transverse momentum can overcome the influence of the ions and be ejected as side electrons. We used the simulations presented in the previous section to investigate the trajectories of the side electrons, which are usually ejected at an angle ≈ 40 degrees w.r.t. the propagation axis [83]. Side electrons are chosen in the simulations by filtering electrons which their final recorded energy is between 1 and 2.5 MeV, and their last recorded transverse position is larger than the bubble radius which is calculated to be $\approx 5\,\mu$m. Because particles converge on the axis of the bubble, the electron density increases by at least two orders of magnitude above the background plasma density. The concentration of charge can repel converging electrons.

Side electrons are selected and studied at three different timesteps of the simulation. Each timestep corresponds to the longitudinal position of the laser, $ct = 180\,\mu$m, $260\,\mu$m, $360\,\mu$m. The `FBPIC` simulations show that 10% to 30% of particles ejected as side electrons cross the back of the bubble. Not all side electrons that cross do so at the first bubble, but some at subsequent ones. They can gather enough whilst forming part of the subsequent bubbles and then cross. The remaining fraction of side electrons "bounce" due to the large charge concentration at the back of the bubble. The simulations suggest that the majority of these side electrons bounce off the back of the first bubble. Fig. 6.2 shows the trajectories of side electrons that have bounced without reaching or crossing the axis, and the averages ($\langle . \rangle$) of the cosines of the relative angles between the initial azimuthal angle and current azimuthal angle ($\langle \cos(\theta_t - \theta_i) \rangle$) of the same particle. Part **f** and **g** of Fig. 6.1 shows a histogram of electrons which have bounced and crossed. It is clear that particles which have crossed have a near 0 deg or 360 deg difference with their initial angle. The bounced electrons demonstrate that most particles have a difference of ≈ 180 deg. However, there are some electrons that have ≈ 0 deg or ≈ 360 deg implying that they may have been mislabelled as bounced rather

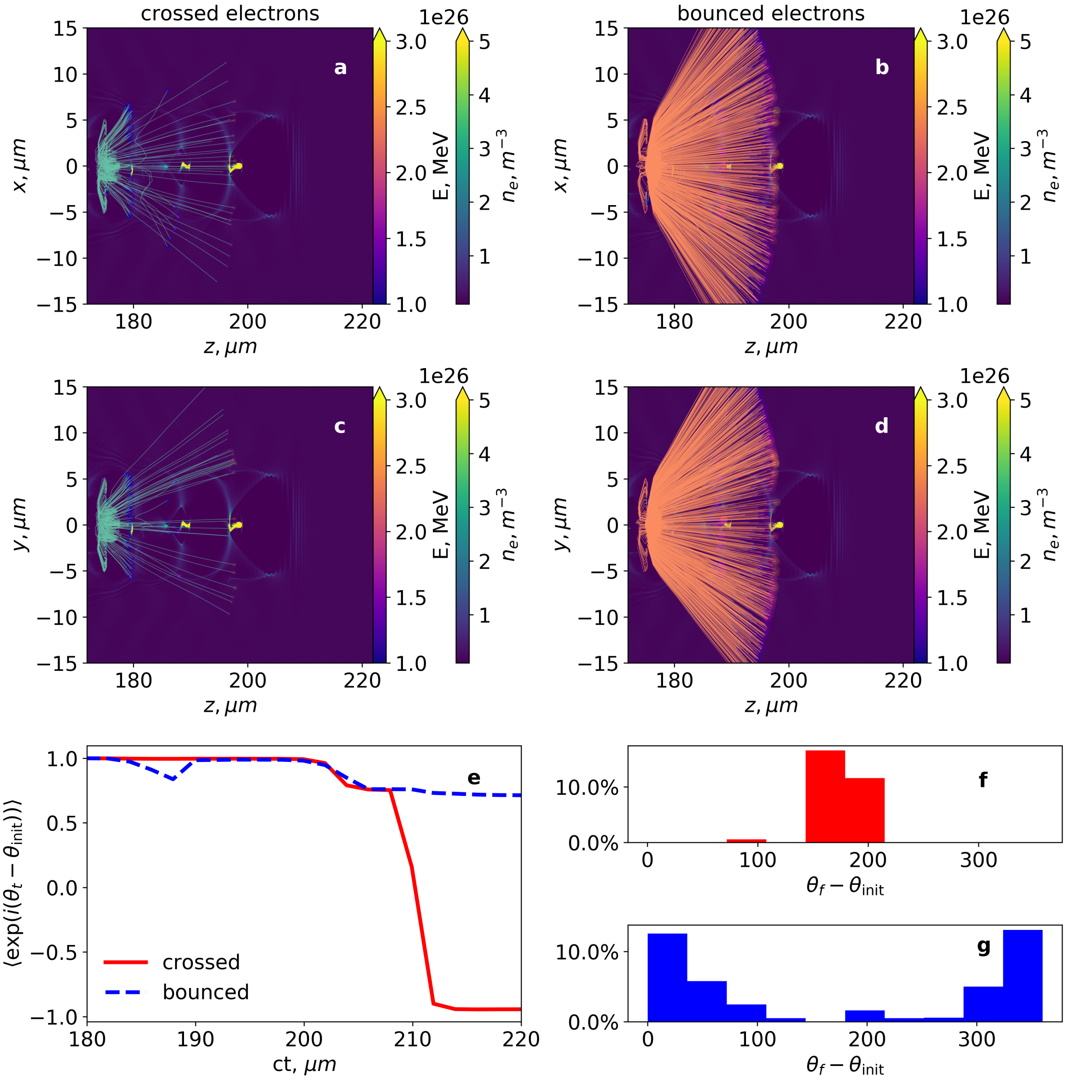

Figure 6.2: Electron density in the longitudinal plane with trajectories and particle position superimposed and colour coded with their energy and transparency corresponding to the weights for crossed (**a**, **c**) and bounced electrons (**b**, **d**). History of the averages of the cosines of the relative angle per time step for crossed and bounced electrons (**e**), histogram of the distribution of relative angle for crossed (**f**) and bounced (**g**) electrons.

than cross. However, the electrons were individually checked to see the trajectories and they have bounced off axis. This can be attributed to the initial position of the electrons to be close to an axis so the difference in angle yield either ≈ 0 deg or ≈ 360 deg. Most side electrons were initially located closer to the axis than a bubble radius. Side electrons are displaced by the ponderomotive force excerted by the laser pulse and later attracted back by the electric field of the ions inside the bubble. As the electrons approach the axis, their transverse momenta decrease due to the higher repulsion felt by the proximity to the axis and high charge, but some have enough momenta to overcome the potential on the axis at the back of the bubble. As they cross, they experience the repulsive force of the large charge concentration. They scatter and acquire transverse and longitudinal momenta before being ejected as side electrons. Several do not have sufficient transverse momenta to be ejected as side electrons and form the sheath of consequent bubbles. Bounced electrons can gain sufficient transverse momenta to be ejected as side electrons, or they can form the subsequent bubble sheaths.

6.3.1 Interaction of particles

As the electron bubble is formed, a sheath with a high number density is formed. From a frame of reference co-propagating with the back of the bubble, the back of the sheath takes the form of a disk where particles converge onto the axis. The disk will have a finite thickness. To model the back of the bubble, we assume that all the particles converge on axis at a constant radial velocity and that they have no axial velocity. The particles will then converge on and can cross the axis. However, we add a small thermal spread to avoid a density singularity on axis. We disregard this region in this study.

Fig 6.3 shows the energies (**b**) and radial momenta (**c**) of electrons in a selected volume at the back of the bubble. The depth of the volume, 600 nm, is chosen is to

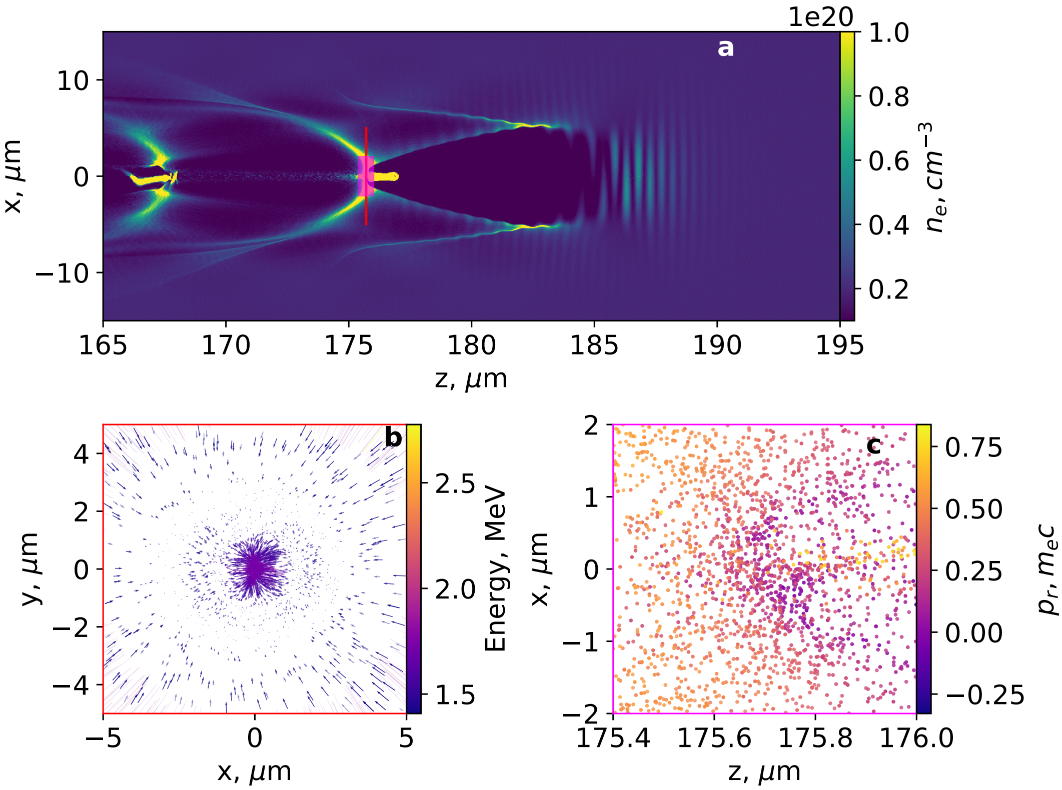

Figure 6.3: Electron density in the plane propagation axis plane with a red lineout corresponding to a volume with dimensions $5\,\mu$m $\times 5\,\mu$m $\times 5\,$nm and a magenta lineout corresponding to a volume of $2\,\mu$m $\times 2\,\mu$m $\times 600\,$nm (**a**). A plot (corresponding to the red lineout in frame (**a**)) with particle position in the transverse plane at $z = 175.7\,\mu$m with an arrow showing their radial momenta coloured by their energy and the transparency corresponding to the particle weights (**b**). A scatterplot in the propagation axis for particles (corresponding to the magenta lineout in frame (**a**) in the back of the bubble coloured by their radial momentum and their transparency correponds to their weight (**c**).

confirm that the particles are in close proximity. Fig 6.3 amplifies the conclusions drawn from Fig 6.2 by demonstrating electrons with opposite transverse momenta where the electron flows overlap. Around $2\,\mu$m from the axis, many electrons have near-zero radial momenta. Further in the simulation, the electrons with zero transverse momenta change direction from converging to diverging and counterstream with converging electrons. However, assuming that the velocity directions are not randomised, but azimuthal angles change either by little (when bouncing, Fig. 6.2 (**f**)) or by close to 180 degrees (when crossing, Fig. 6.2 (**g**)) due to the on-axis charge, an azimuthal modulation formed in the converging electron stream leads to an in-phase modulation in a diverging stream if the electrons have bounced, while in a stream of electrons having crossed only modulations with even mode numbers are in phase, but those with odd mode numbers are out of phase with the converging stream. Since the unstable growth requires out-of-phase modulations in the counter-streams, the modulations must change phase in the opposite case. The out of phase modulations are needed for the feedback loop. If the instability is to persist, the peaks and troughs of the converging or diverging electrons will have to rearrange to permit the current filamentation of both converging and diverging populations. A magnetic field co-propagating with the back of the bubble can allow for the instability to continue forming and perpetuate the filamentation at the back of the bubble. This magnetic field can arise due to the interaction of particles at the back of the bubble. It can also seed a modulation in new electrons which are converging into the back of the bubble. Fig. 6.4 shows a schematic of the history of the electrons as they converge towards high charge.

From the initial simulations from `FBPIC` and `OSIRIS`, it is concluded that most particles bounce off rather than go through the axis. Therefore, the filamentation instability can only grow if modulations can re-arrange quickly.

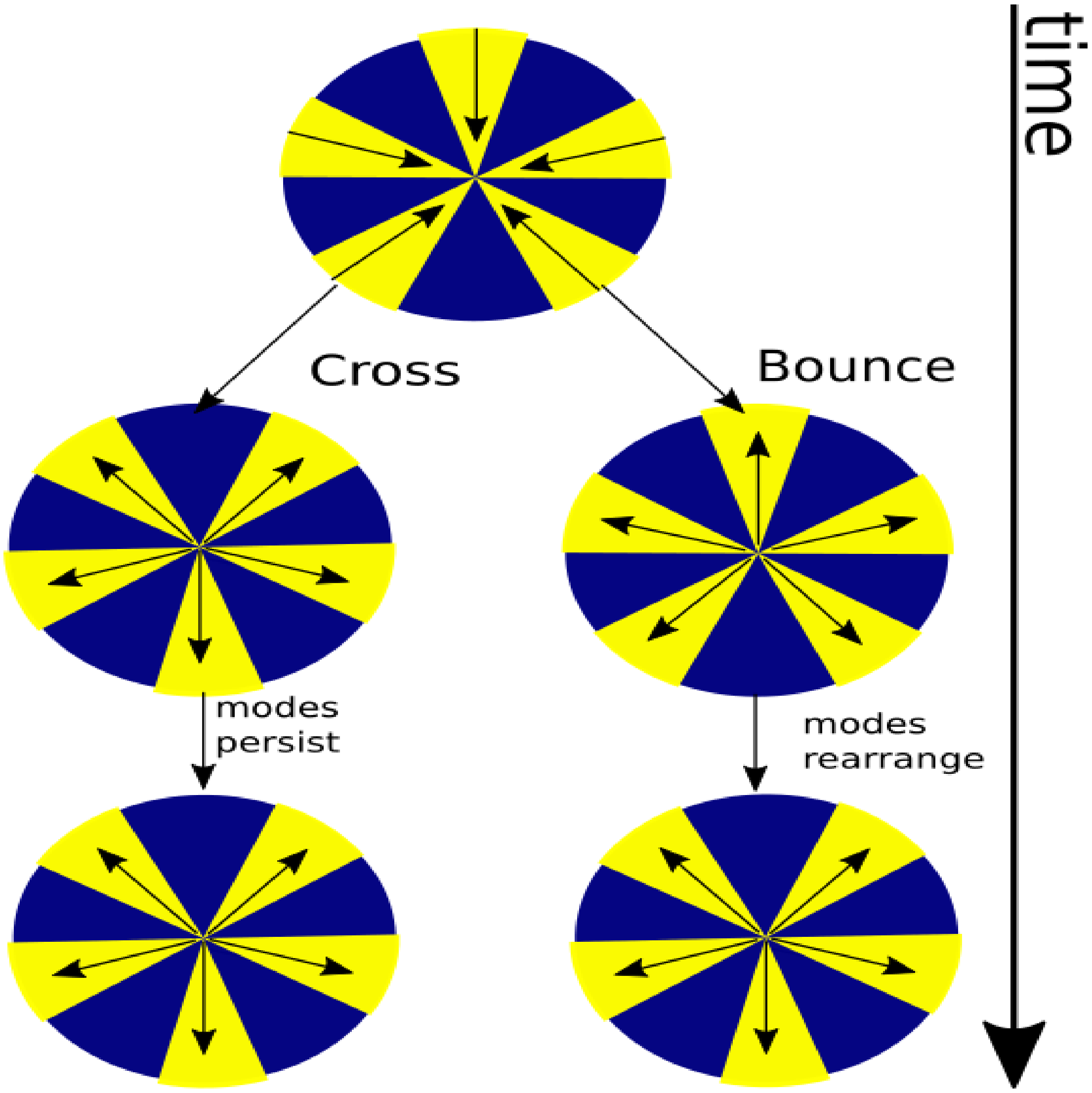

Figure 6.4: A schematic describing the scenario for crossing and bouncing electrons. The yellow wedges correspond to electron modulations and the arrows to the direction of the flow.

6.3.2 Mode rearrangement

Counterstreaming annuli

To demonstrate how density modulations in the electron streams re-arrange, simulations using `EPOCH`[33] have been performed to replicate the back of the bubble for two counterstreaming electron annuli with in-phase modulations. The parameters are similar from those used from the `FBPIC` and `OSIRIS` simulations. The annuli have a number density of $1.1\times10^{20}\,\mathrm{cm}^{-3}$ at the point of full overlap, where $n_1 = A_2 n_2 / A_1$, where n_j is the number density of the annuli; A_j is the area of the annuli, a radial velocity corresponding to $\gamma = 2.5$, a temperature of 12.8 eV as for the `FBPIC` and `OSIRIS` simulations. The annuli have corresponding co-propagating ion annuli to avoid expansion and initial electric and magnetic fields are added explicitly since `EPOCH` assumes vanishing initial fields.

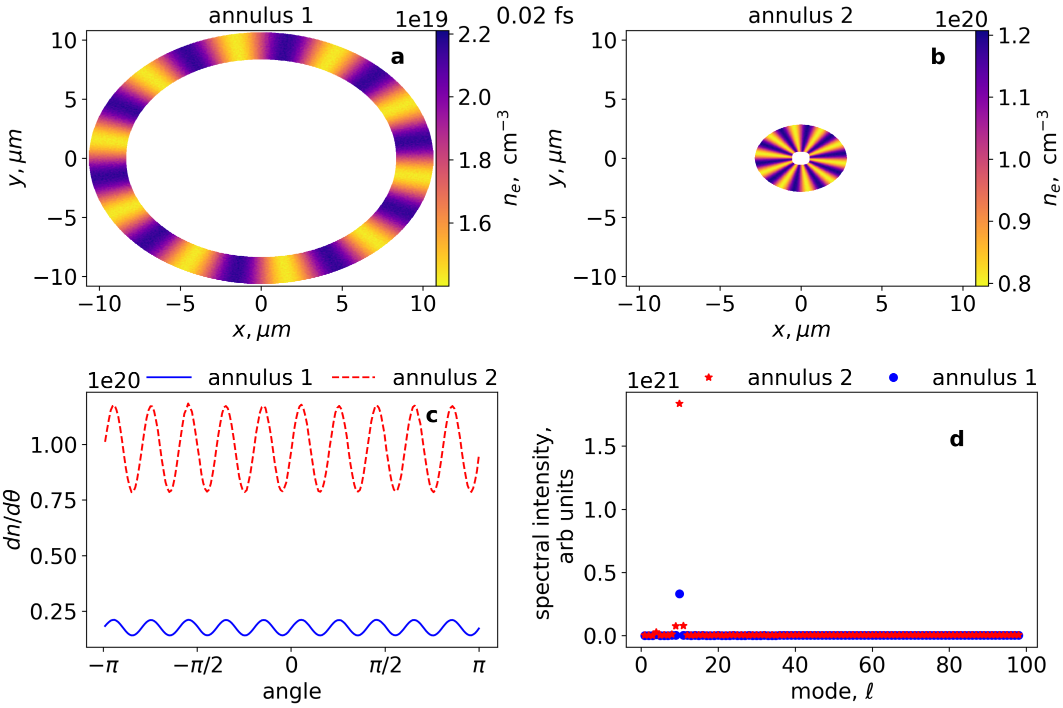

Figure 6.5: Electron number density of the converging (**a**) and diverging (**b**) electron annuli, the radially integrated azimuthal number density (**c**), and their corresponding fast Fourier transform (FFT) (**d**) at the initial timestep

Figure 6.5 (**a**) and (**b**) are the initial setup with both annuli exhibiting sinusoidal modulations in the azimuthal direction, both with mode number 10 and 20% relative amplitudes. As annulus 1 shrinks and annulus 2 expands, they pass through each other. As described in the previous chapter, the modulations respond to the interaction with a small delay. Fig. 6.6 shows the same simulation after the annuli have fully overlapped. In Fig. 6.6, the modulation depth of annulus 1 has decreased. As the annulus shrinks, the electrons are compressed to a smaller volume than it was before, leading to stronger repulsion which reduces the relative modulation strength, while that of annulus 2 persists during its expansion. Prior to full overlap, annulus 2 had a stronger

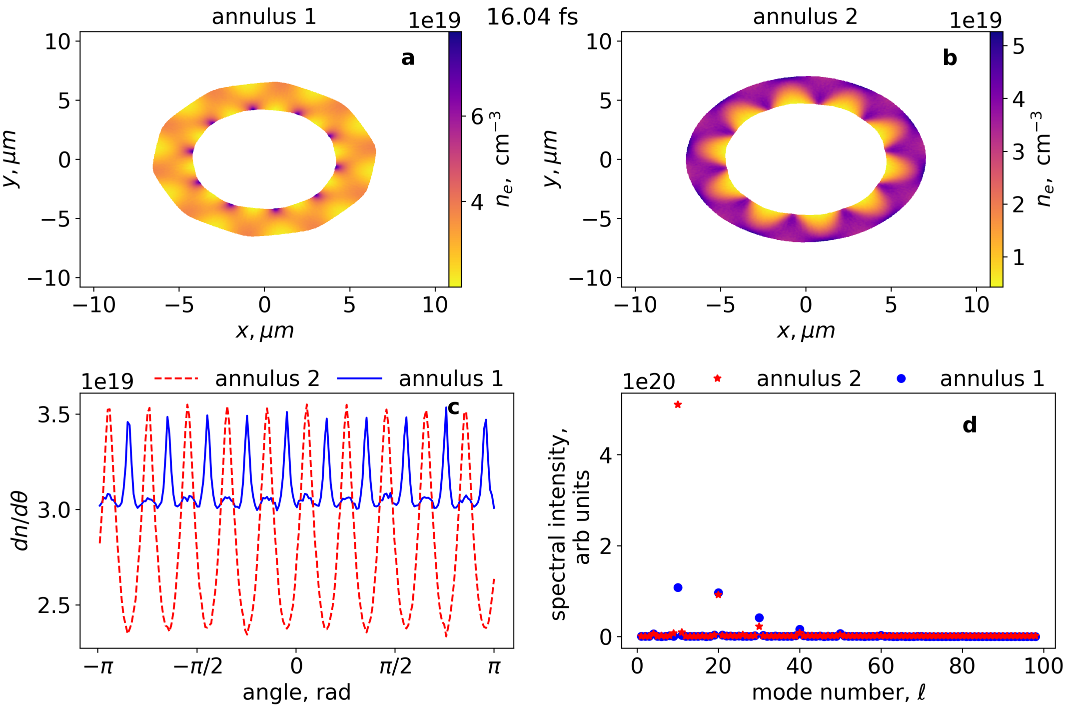

Figure 6.6: As Fig. 6.5, but snapshot at 16.04 fs.

modulation strength and continued to have a stronger modulation. This implies that when the annuli overlap and the average densities are equal, the density modulations in annulus 2 are stronger than in annulus 1, and the corresponding currents dominate the generation of the magnetic field. In addition to re-arranging the modulations in annulus 1 (causing a phase shift of π). Figure 6.6 **c**) and **d**) show peaks in the azimuthal intensity which can be attributed to the radial integration to obtain the data for **c**. As demonstrated, from two in-phase modulated populations, where one population has a weaker modulation, the stronger modulation dominates and imposes its phase on the modulation. Fig. 6.6 **a**) shows that the modulations have re-arranged on the inside of annulus 1, but not on the outside. This corresponds to the duration of overlap and thus interaction with annulus 2. On the other hand, the decrease of modulation depth from inside to outside of annulus 2 is due to the reaction to the in-phase modulations in annulus 1. The radial dependence of the modulation strength is largely due to the setup of the electron streams as rings of finite width in the simulation.

Discussion

The simulations for two counterstreaming annuli demonstrate that the instability can persist for two pre-modulated streams in a converging geometry. The presence of a modulation that is π out of phase with respect to annulus 2 is a clear indication. However, it remains to show that the signal grows during interaction. Using the eqn. 5.22 we can compare the signal growth

Fig. 6.7 shows the evolution of the signal and the growth rate. In the beginning of the simulation, the growth rate decays since both annuli are not interacting. The repulsion forces of the electrons also dampen the modulation depth. The re-arranging of the modulations necessary for the growth of their amplitudes causes a delay compared to the case where just one stream is modulated. The positive growth rate observed towards the end of the overlapping period is ascribed to the completion of the re-arrangement. Unstable growth occurs and the instability survives a collision of two annuli with in-

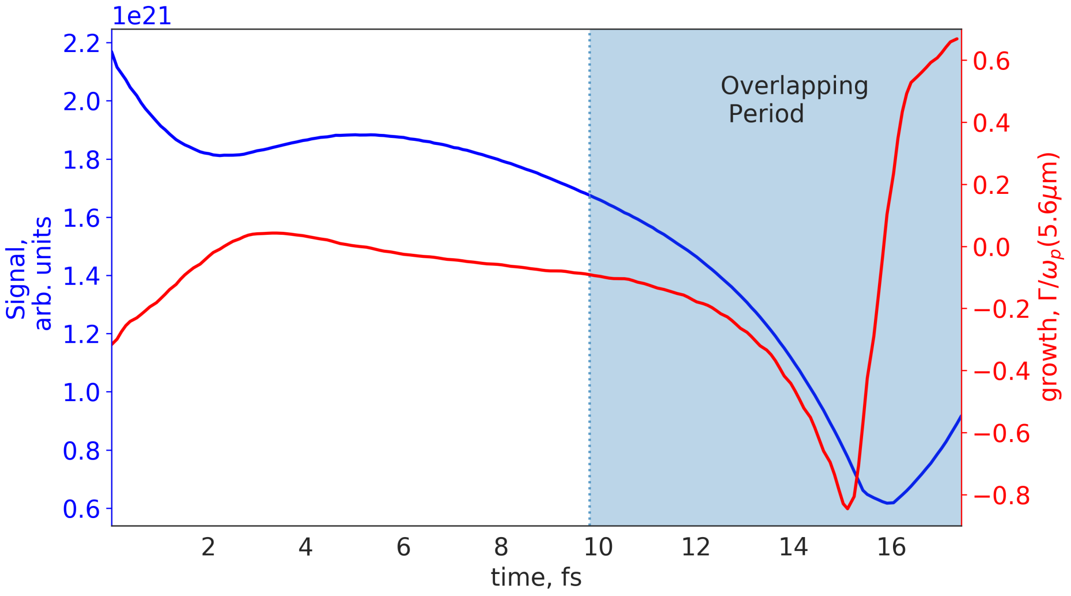

Figure 6.7: Signals of the modulation (solid blue line) and the inferred growth rate (solid red); the overlapping period denoted is coloured blue.

phase modulations. In practice, both bounced and crossed particles would interact. However, there are more bounced particles and thus will dominate over the crossed particles.

Counter-streaming slabs

To confirm the observations in the previous subsections, we have performed simulations with two counterstreaming slabs of electrons flowing through each other. Both slabs have a number density of $1 \times 10^{20}\,\mathrm{cm}^{-3}$, equal and opposite velocities corresponding to a Lorentz factor $\gamma = 2$, and temperature of $T = 12.8\,\mathrm{eV}$ as in the `FBPIC` and `OSIRIS` simulations. The cell size is $10 \times 10\,\mathrm{nm}$, with 20 particles per cell in a $5 \times 5\,\mu\mathrm{m}$ simulation window. Both populations have been given initial sinusoidal modulations transverse to the direction of propagation, with wavelength $\lambda = 300\,\mathrm{nm}$ and modulation strengths (relative to the average density) of 10% for slab 1 and 8% for slab 2. The simulations have periodic boundary conditions and do not have initial fields explicitly added as in the counter-streaming annuli case.

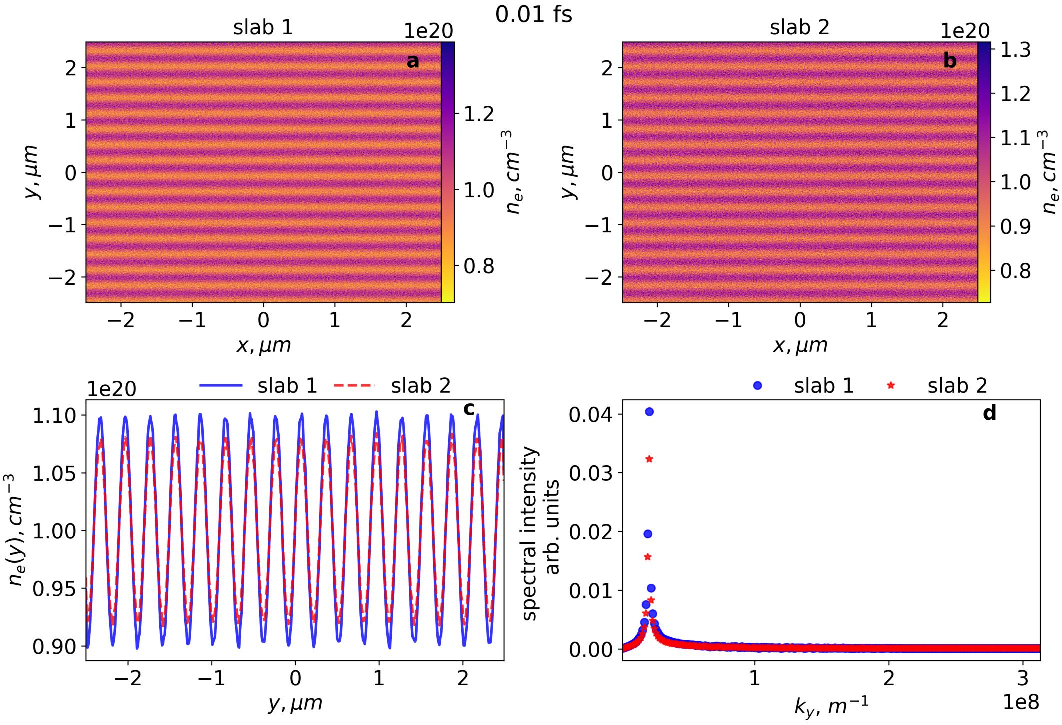

Figure 6.8: Electron number densities of slabs 1, (**a**), and 2, (**b**), averaged over x along y, (**c**), and the corresponding fast Fourier transform, (**d**).

Fig 6.8 shows the initial timestep of the simulation. Both counter-streaming populations fully overlap and interact from the start of the simulation, so that the instability evolves everywhere in the same way. The modulations, which are initially in phase, compete to set up an unstable pattern of out-of-phase modulations characteristic of the filamentation instability. As the simulation progresses, slab 1 with its stronger modulation determines the phase of the magnetic field, which re-distributes the electrons in slab 2, resulting in an out-of-phase modulation.

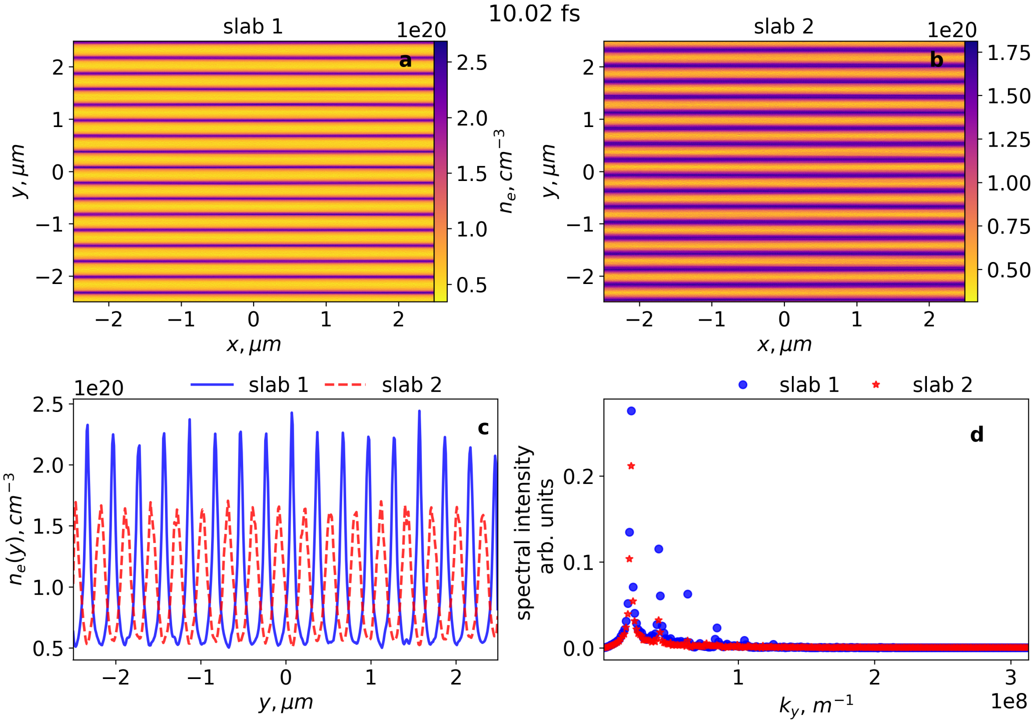

Figure 6.9: As Fig. 6.8 but timestep 10 fs

As shown in Fig 6.9, after a short time, the modulation strengths in both slabs increase because of the instability. As discussed above, the increase in the modulation strength is a clear indication of the current filamentation instability.

Discussion

Figures 6.8 and 6.9 support our hypothesis from the results in the counterstreaming annuli simulations, where a pre-modulated electron population colliding with an in-phase, pre-modulated electron population, but with a weaker modulation strength, will lead to the stronger modulation imposing the phase on the modulation.

From Fig. 6.10 it is immediately noticeable that growth begins before 6 fs. The growth rate is then similar to what is expected for the homogeneous case, but then

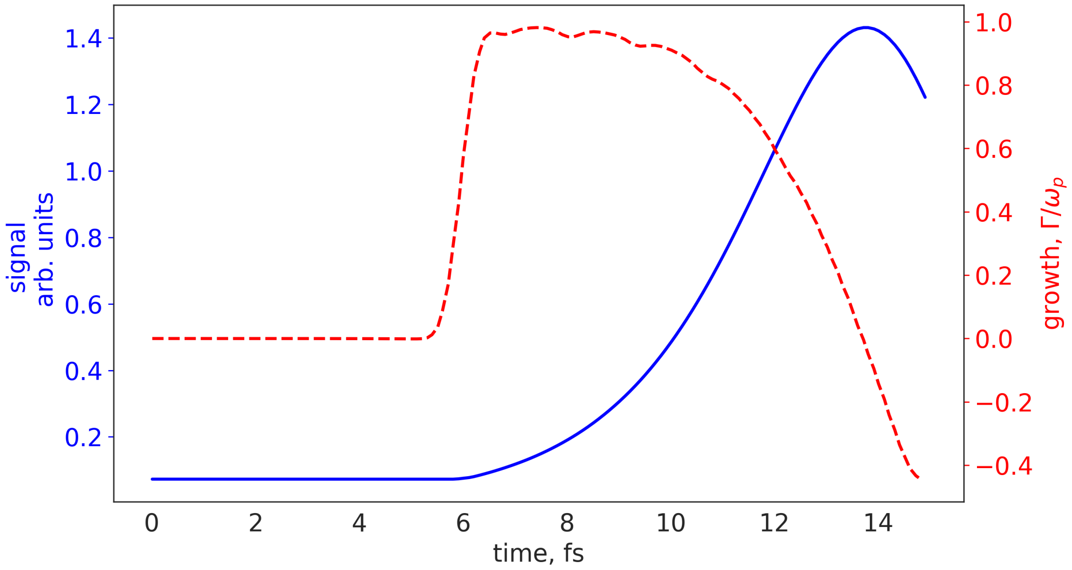

Figure 6.10: Signals of the modulation (solid blue line) and the inferred growth rate (dashed red)

drops off as non-linear effects become important.

Equal modulation strengths

In the previous examples, the phase adopted by the modulations is determined by the one that is stronger at the start of the interaction. In order to ascertain how the instability evolves without such an initial asymmetry, a simulation using `EPOCH` has been performed similar to that in the previous section, but with initial modulation strengths of 10% for both slabs.

In the cases considered above, the interaction of the two counter-streaming slabs gives rise to the current filamentation instability. In contrast to these cases, in absence of an asymmetry between the streams, perturbations grow from random fluctuations, resulting in noisy modulations with broad spectra, as can be seen from Fig. 6.12.

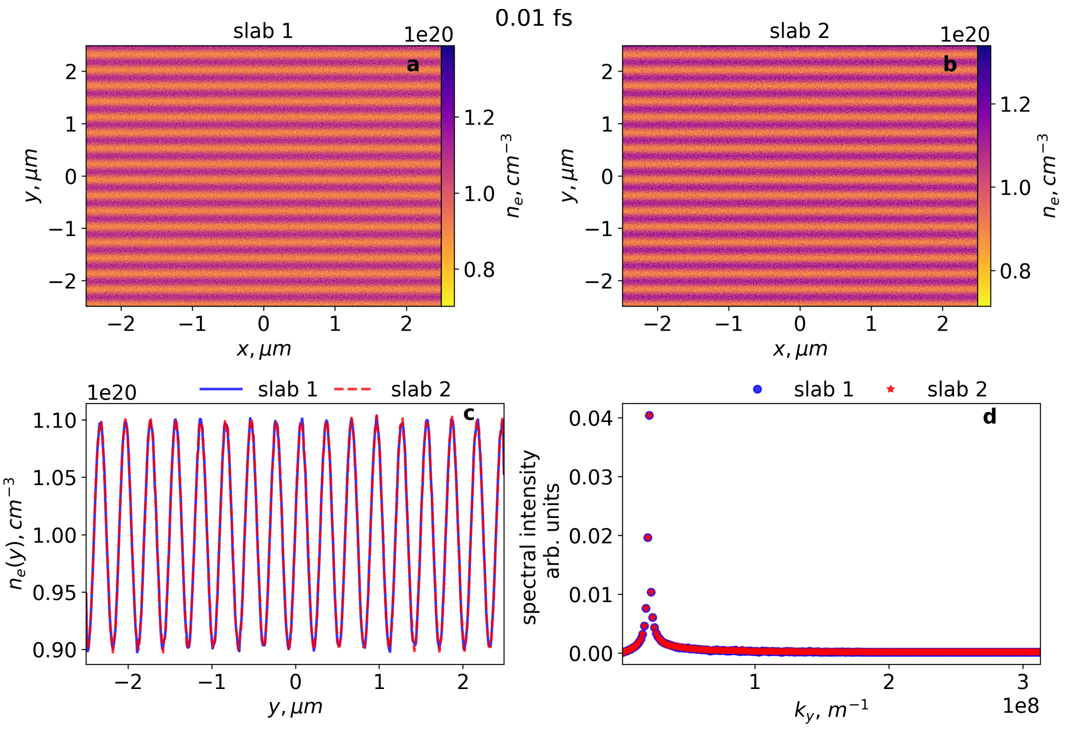

Figure 6.11: Electron number densities of slabs 1, (**a**), and 2, (**b**),averaged over x along y, (**c**), and the corresponding fast Fourier transform, (**d**).

Discussion

The case for two equally modulated slabs shows unstable growth without either slab dominating the other one. As from Figures 6.11 and 6.12, it is clear that unstable growth can be attributed to the noise inherent in both of the bunches. This noise is attributed to the deviations caused by small perturbations in the plasma.

Fig. 6.13 shows a large difference from the case for two modulated bunches with different strengths. The instability takes longer to develop and the inferred growth rate is weaker. The delay in growth development can be attributed to the "lack of an effective seed", similar to the case of two unmodulated counterstreaming beams. Initially, the perturbations have a wave number spectrum determined by the fluctuations, but as

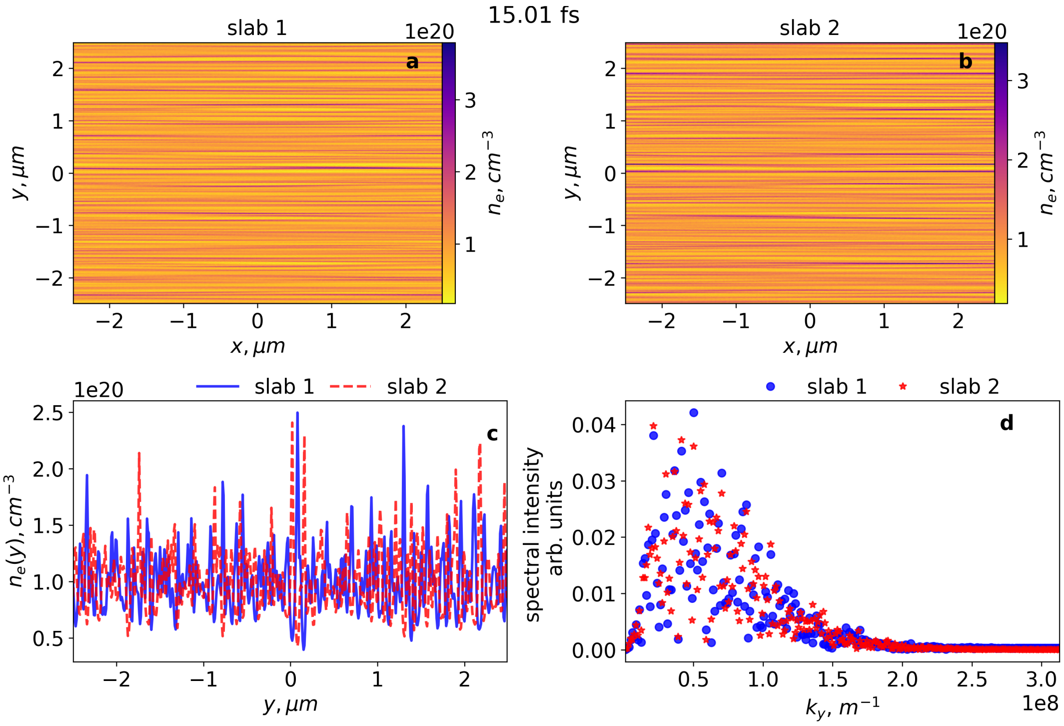

Figure 6.12: As Fig. 6.11 but snapshot for timestep 15 fs

they grow, the wave number with the highest growth rate will dominate. These grows similarily as with the initially unmodulated case.

Reversed beams

To replicate to a limited extent the situation of electrons bouncing off the repulsive potential at the back of the wakefield bubble and changing directions, another simulation was set up where the slabs instantaneously change the direction of motion whilst the electric and magnetic fields stay the same. This is to replicate the conditions at the back of the bubble where electrons will change momentum and interact with electric and magnetic fields which are in-phase with the electron number density modulation. The simulation is for two counter-propagating slabs with in-phase modulations of slightly

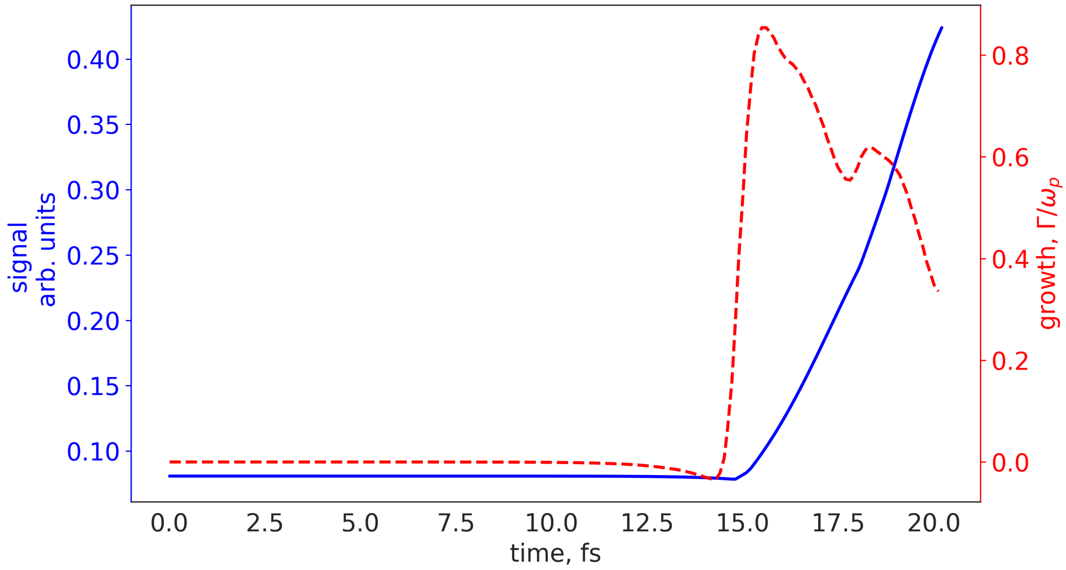

Figure 6.13: Signals of the modulation (solid blue line) and the inferred growth rate (dashed red)

different strengths. The initial setup is as in Fig 6.8 for the first part of the simulation, which is exactly the same as in the counter-streaming slabs subsection. At timestep 10 fs, the slabs change direction and then counterstream in the fields developed due to the instability created by the initial streams. The currents of the reversed slabs yield a magnetic and electric field opposite to those of the first simulation immediately prior to reversal. After changing the direction, the growth stagnates for a few timesteps but it quickly recovers and continues. Fig 6.14 shows the growth 5 fs after changing the direction of the momentum. This simulation demonstrates that even though the initial fields, for the second part of the simulation, have the opposite orientation to that corresponding to the electron currents the unstable growth continues after a short delay due to the inertia of the currents in the filaments. The systems adapts quickly to this

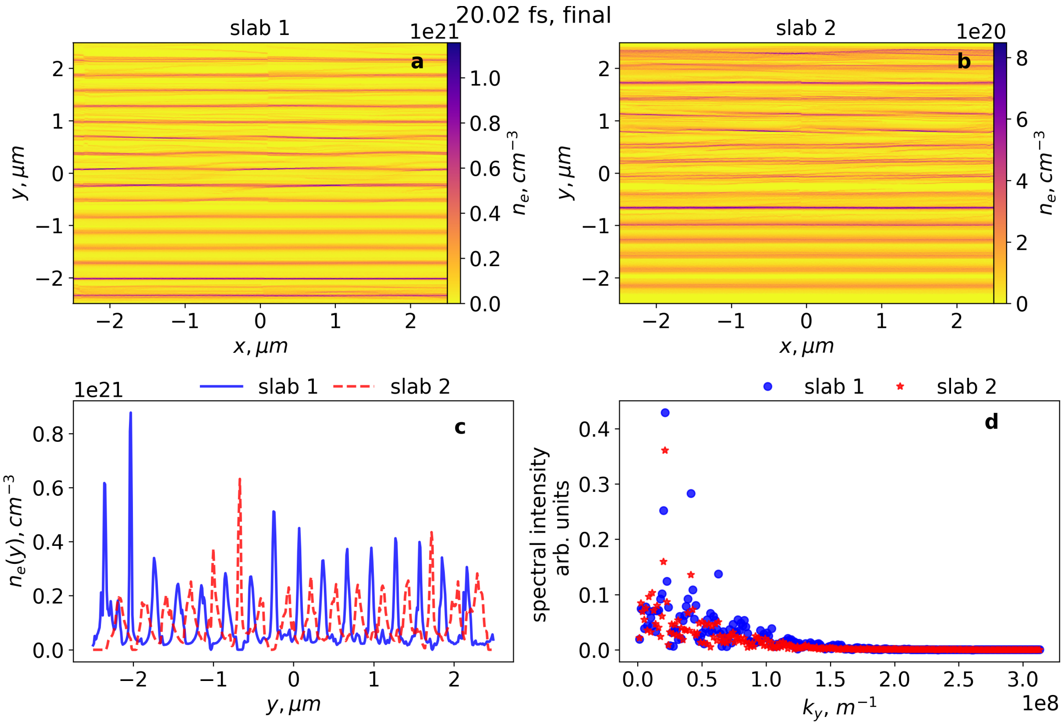

Figure 6.14: Number density of slab 1 (**a**), slab2 (**b**), corresponding averaged number density along x, (**c**) and their corresponding fast Fourier transform (**d**) in timestep 20 fs corresponding ton the initial setup after changing the momentum direction.

new setup albeit with the opposite initial currents making clear that unstable growth can occur.

Discussion

Similarly, the signal growth is worth discussing for reversed flows and different modulation strengths. From the simulation presented in the previous subsection, it is noticeable that the instability persists. However, the unstable growth varies along the initial and the pre-loaded (second part of the) simulation with the slabs reversing the propagation direction.

Fig. 6.15 shows the evolution of the signal and growth rate in this simulation. The

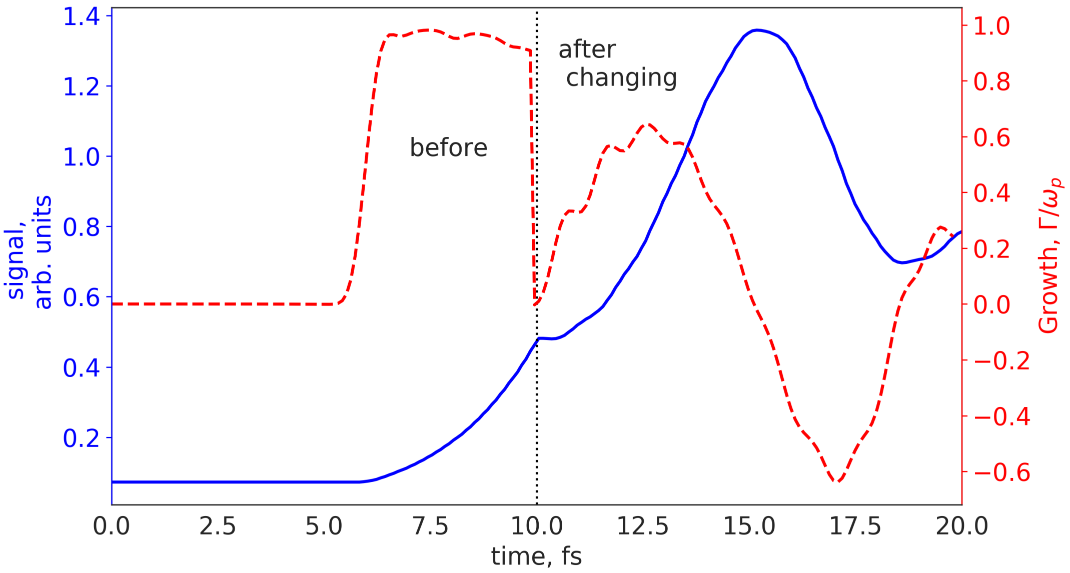

Figure 6.15: Signals of the modulation before and after the electron streams reverse direction (solid blue line) and the inferred growth rate (dashed red).

unstable growth takes around 5.5 fs to develop after the momenta reverses. As we change the direction of propagation of the slabs, the growth pauses and the signal plateaus for a few femtoseconds before increasing again. Later on, the instability enters its nonlinear phase and the predetermined modulation at $\lambda = 300\,\mathrm{nm}$, begins to reach a peak strength before decreasing to half its strength. The growth rate also demonstrates this by showing a decrease and then a slight increase.

Reflected beams, reflected boundary

As in the previous subsection, we want to see what happens when an electron beam is reflected to encounter itself in the process, i.e., having the same process. While encountering itself, it would interact with an in-phase modulation with equal strength and we would expect to see a similar result to that presented in the previous sections.

Instead of having two counterstreaming beams as presented previously, we now have a single electron beam propagating in the $-x$-direction with a velocity corresponding to $\gamma = 2$. The beam has an initial number density of $1 \times 20\,\mathrm{cm}^{-3}$, and we increase the window size in $+x$-direction to approximate a constant flow of electrons to the left boundary. The size of the window is now 10 µm tall and 12 µm wide. From Fig. 6.16, it is observed that a modulation is present in the front of the reflected beam. Part **b** of Fig. 6.16 also demonstrates an out-of-phase modulation in the reflected beam. Unstable

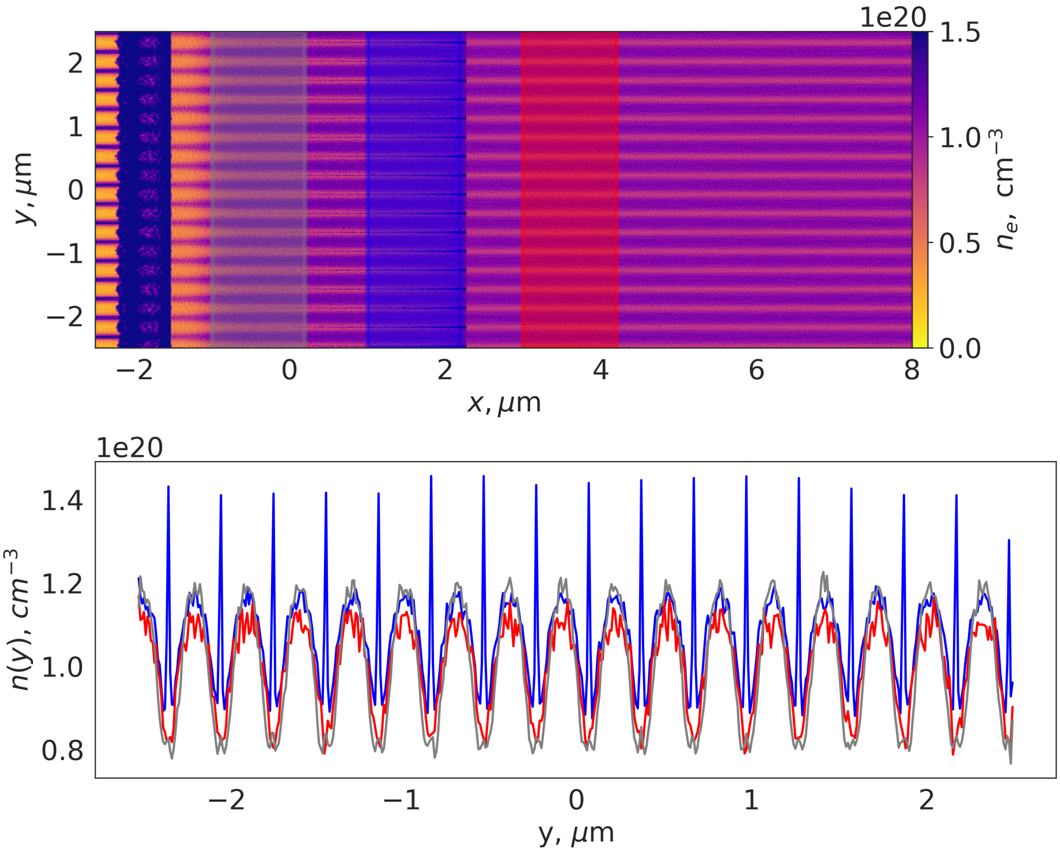

Figure 6.16: Timestep 16.4 fs of the reflective boundary simulation. Number density of the electron slab with a grey lineout of width $1.2\,\mu$m, a blue lineout at $1\,\mu$m with the same width and a red lineout at $3\,\mu$m with the same width (**a**). The number density along y averaged in x with the three corresponding coloured lineouts in (**a**), (**b**).

growth is able to predominate even when the reflected beam interacts with itself. This yields a stronger argument that bouncing electrons from the back of the bubble will interact with the incoming beam and can change the phase of the modulation.

6.4 Conclusions

The experiment discussed in the chapter 3 showed evidence azimuthal striations in the electron beam ejected transversely to the laser wakefield bubble's propagation. In this chapter, we discussed the causes of these microstructures. PIC simulations have been performed to study the dynamics and trajectories of electrons as they are ejected transversely from the laser wakefield bubble structure. Most of these side electrons originate from within a bubble radius of the propagation axis, and most of them (between 70% and 90%) have bounced off the large charge concentration at its rear. Diverging electrons (side electrons and electrons forming the subsequent bubbles) counterstream and interact with converging electrons which are closing the bubble structure, which can lead to streaming instabilities.

Quasi-3D simulations in `FBPIC` and full 3D simulations `OSIRIS` have been performed to test if azimuthal modulations are plausible in the LWFA. Neither code demonstrated any azimuthal striations. In the case of `FBPIC` the lack of azimuthal striations in the side electrons can be attributed to the low mode number constraint to perform these simulations. `OSIRIS` lack of results can be attributed to resolution and particle number which are limitations for modern super computers. Further studies can be performed to demonstrate if grid heating can diminish the growth of instabilities at regions of high density with a small number of cells. A reduced model of the full simulations is adopted for two pre-modulated systems, consisting of two counterstreaming annuli, and they have demonstrated succesful change of phase of the modulation of one particle populations and the other mantaining its phase.

2D simulations in a slab geometry have been performed to confirm the observations from the counter-streaming annuli simulations. Two counter-streaming electron slabs with in-phase modulations with asymmetric modulation strengths have been performed. The simulations demonstrate that the stronger modulation imposes a phase change on the weaker modulated slab. 2D simulations with two in-phase, but equally strong modulations have been performed and demonstrate unstable growth from noise. A third simulation, where the propagation of the slab is reversed while mantaining the field information of the original direction has been performed. These demonstrate a stagnation in the unstable growth, which then regains strength before nonlinear effects become important. Finally, simulations with a reflective boundary demonstrates that a reflected beam propagating within itself will also impose a change in phase and exhibit unstable growth. These set of simulation support the hypothesis that when particle have bounced and interacted with incoming beams, it is possible that a modulation phase may switch to perpetuate the instability. To conclude, further 2D slab geometry simulations with a reflective boundary need to be performed and the growth rates studied at different points. Besides, a future project related to this investigation would be to perform 3D simulations with increased resolution and particle numbers to search for striations.

Chapter 7

Conclusions and outlook

In this thesis, we have developed a theory for streaming instabilities in converging/diverging geometries for relativistic plasmas. We began by introducing the problem for inhomogeneous plasma streaming radially inwards whilst interacting with another beam streaming radially outwards. We derived a set of linear, coupled ordinary differential equations that are then solved as an eigenvalue problem. The eigenvalues demonstrate a coalescence and bifurcation of the real and imaginary parts of the wavenumber as a function of position for real frequencies. We then implemented an approach where the real and imaginary parts of the wavenumber are mapped for varying imaginary frequency and investigated for saddle points that switch from the real to the negative imaginary parts of the wavenumber. The spatial dependence of the growth rates is also investigated as the number density is spatially dependent and it is demonstrated to have an inverse depedence on the radial positions.

Particle-in-cell simulations were performed for two counterstreaming electron annuli to investigate the microstructure formation for counterstreaming beams in a converging geometry. In the simulations co-moving ion beams were added to avoid an expansion of the electron annuli and cancel any initial fields prescribed by the PIC codes. An initial small modulation was added to an annulus to seed the instability and for ease of calculation. The initially unmodulated annuli exhibited a modulation to the same mode number π out of phase with the initially modulated bunch in any of the iterations. The thermal spread is calculated along the simulation to discard coupling between the CFI and Weibel instabilities. The growth is compared with the single propagating annuli to demonstrate the extent of geometrical effects in the annuli and discard any artificial growth/decay. The growth rate is then calculated from an FFT of the azimuthal number density of each annuli. The growth rates agree well within an order of magnitude to the semi-analytically calculated growth rates and exhibit a radial dependence similarily. The semi-analytical theory is expanded further by adding a small thermal spread to the plasma. The thermal spread is anisotropic and can be calculated from the equations of state. The thermal spread is added to model more accurately the experimental observations and avoid a seemingly infinite range of modes yielding unstable growth as for CFI in the cold case (see streaming instability section). The semi-analytical predictions yield a finite spatial range where the instability is plausible, similarily as in the cold case. The maximum, local, temporal growth rates are obtained by mapping the real and imaginary parts of the wavenumbers with varying imaginary frequency. The range of mode numbers yielding the instability is reduced, as in the slab geometry case. A range yielding the maximum growth rate is obtained and shows to favour smaller mode numbers. The favouring of small azimuthal mode number can be attributed to particles that escape the pinching magnetic fields due to their higher energies.

Further PIC simulations are performed to compare the prescribed semi-analytical results. Simulations using an initially modulated bunch, as in the cold case, were performed, except with isotropic temperature distributions. The growth rates obtained show qualitative similarities to the semi-analytical prescription, in addition to the range of mode numbers that yield the largest growth rates. The temperature range in which the instability is present also agrees qualitatively with the predicted growth rates.

The thesis also reports on experiments performed to observe microstructure formation in side electrons from a laser wakefield accelerator. The side electrons demonstrate a very high charge and striations in their azimuthal direction. These seem quasi-periodic in nature, which resembles the current filamentation instability. Such striations are observed in the side electrons in every shot. It can be inferred that an instability is bound to occur which result in filamentation of the radially outward propagating electrons. From these experimental observations, we develop a theory taht may explain the origin of the striations.

Full 3D PIC simulations using `OSIRIS` and quasi-3D simulations using `FBPIC` were performed to compare with the experimental results, and investigate if azimuthal striations in the radial momentum of side electrons can be reproduced. The full simulations failed to demonstrate such striations when an initial temperature was added. Numerical amplification of the temperature of the particles can "wash out" azimuthal modulations and suppress the instability mechanism. It has been demonstrated in literature that thermal effects can effectively suppress instabilities [65]

A theory for the particle dynamics at the back of the bubble is proposed to explain the azimuthal strations at the back of the bubble. These investigate counterstreaming flows and show that the majority of electrons that are ejected as “side electrons” bounce off from the charge build a region concentrated on the axis of the bubble. We then present a reduced model of a beam bouncing and interacting with itself. The beam is reduced to two counter-streaming annuli and modelled in PIC simulations using `EPOCH`. Both annuli have in-phase modulations. After interaction, annuli changed its phase of modulation implying that an instability adjusts its modulation phase. To support this argument, simulations in slab geometry were performed for i) two counter streaming slabs, ii) with an asymmetric modulation strength, iii) equal modulation strength, reversed at a timestep and iv) reflected from a boundary. Each simulation demonstrated a change of modulation phase with exception of the equally modulated strengths which demonstrated a modal distribution similar to two initially unmodulated bunches.

The methods presented in this thesis provide an insightful approach to studying instabilities in cold and warm plasma with converging/diverging geometries. This semi-analytical approach can be applied to a wide range of equations that cannot be solved analytically or where analytical solutions are too complicated. This theory can be expanded to encompass a kinetic approach, rather than a fluid approach which can yield insight to the deformation of plasma distribution functions and including coupling to more instabilities.

Further PIC simulations need to be performed to investigate microstructure formation at the rear of the bubble. A study in the self-heating in these PIC codes is required to prove the extent of the influence of the grid in the particles. It is known that the laser-particle interactions also heat particles. More simulations with a larger number of particles per cell would yield a better result and hopefully a better agreement between theory and experiments.

Bibliography

[1] R. J. Goldston and P. H. Rutherford. *Introduction to plasma physics*. Taylor and Francis Group, 2005.

[2] T. Robinson. Kelvin-Helmholtz Clouds (DI00152). URL `https://opensky.ucar.edu/islandora/object/imagegallery:151`. accessed May 24, 2022.

[3] P. K. Sharma and R. K. Chhajlani. Kelvin–Helmholtz instability of magnetized plasma with polytropic pressure laws. *Phys. Plasmas*, **5**(3):625–634, 1998. doi: 10.1063/1.872780. URL `https://doi.org/10.1063/1.872780`.

[4] A. Bret, L. Gremillet, and M. E. Dieckmann. Multidimensional electron beam-plasma instabilities in the relativistic regime. *Phys. Plasmas*, **17**(12):120501, 2010. doi: 10.1063/1.3514586. URL `https://doi.org/10.1063/1.3514586`.

[5] T. Tajima and J. M. Dawson. Laser electron accelerator. *Phys. Rev. Lett.*, **43**:267–270, 1979. doi: 10.1103/PhysRevLett.43.267. URL `https://link.aps.org/doi/10.1103/PhysRevLett.43.267`.

[6] D. Strickland and Mourou. G. Compression of amplified chirped

optical pulses. *Opt. Commun.*, **56**(3):219–221, 1985. ISSN 0030-4018. doi: https://doi.org/10.1016/0030-4018(85)90120-8. URL `https://www.sciencedirect.com/science/article/pii/0030401885901208`.

[7] D. J. Griffiths. *Introduction to electrodynamics.* Pearson Education, fourth edition. edition, 2014. ISBN 9781292021423.

[8] J. D. Jackson. *Classical electrodynamics.* Wiley, New York, 3rd edition, 1999. ISBN 047130932X.

[9] P. Gibbon. *Short Pulse Laser Interactions with Matter.* Imperial College Press, 2005. doi: 10.1142/p116. URL `https://www.worldscientific.com/doi/abs/10.1142/p116`.

[10] A. L. Pokrovsky and A. E. Kaplan. Relativistic reversal of the ponderomotive force in a standing laser wave. *Phys. Rev. A*, **72**:043401, 2005. doi: 10.1103/PhysRevA.72.043401. URL `https://link.aps.org/doi/10.1103/PhysRevA.72.043401`.

[11] H. Boot and D. A. Harvie. Charged Particles in a Non-uniform Radio-frequency Field. *Nature*, **180**(4596):1187–1187, 1957. ISSN 1476-4687. doi: 10.1038/1801187a0.

[12] D. Bauer, P. Mulser, and W. H. Steeb. Relativistic ponderomotive force, uphill acceleration, and transition to chaos. *Phys. Rev. Lett.*, **75**(25):4622–4625, 1995. ISSN 0031-9007.

[13] T. W. B. Kibble. Refraction of electron beams by intense electromagnetic waves. *Phys. Rev. Lett.*, **16**(23):1054–1056, 1966. ISSN 0031-9007.

[14] G. J. Morales and Y. C. Lee. Ponderomotive-force effects in a nonuniform plasma. *Phys. Rev. Lett.*, **33**(17):1016–1019, 1974. ISSN 0031-9007.

[15] J. R. Cary and A. N. Kaufman. Ponderomotive effects in collisionless plasma: A lie transform approach. *Phys. Fluids*, **24**(7):1238–1250, 1981. doi: 10.1063/1.863527. URL `https://aip.scitation.org/doi/abs/10.1063/1.863527`.

[16] C. Grebogi and R. G. Littlejohn. Relativistic ponderomotive hamiltonian. *Phys. Fluids*, **27**(8):1996–2004, 1984. doi: 10.1063/1.864855. URL `https://aip.scitation.org/doi/abs/10.1063/1.864855`.

[17] P. Sprangle, E. Esarey, A. Ting, and G. Joyce. Laser wakefield acceleration and relativistic optical guiding. *Appl. Phys. Lett.*, **53**(22):2146–2148, 1988. doi: 10.1063/1.100300. URL `https://doi.org/10.1063/1.100300`.

[18] E. Esarey, C. B. Schroeder, and W. P. Leemans. Physics of laser-driven plasma-based electron accelerators. *Rev. Mod. Phys.*, **81**(3):1229–1285, 2009. ISSN 0034-6861.

[19] J. M. Dawson. Nonlinear electron oscillations in a cold plasma. *Phys. Rev.*, **113** (2):383–387, 1959. ISSN 0031-899X.

[20] E. Esarey and M. Pilloff. Trapping and acceleration in nonlinear plasma waves. *Phys. Plasmas*, **2**(5):1432–1436, 1995. doi: 10.1063/1.871358. URL `https://doi.org/10.1063/1.871358`.

[21] I. Kostyukov, A. Pukhov, and S. Kiselev. Phenomenological theory of laser-plasma interaction in "bubble" regime. *Phys. Plasmas*, **11**(11):5256–5264, 2004. doi: 10.1063/1.1799371. URL `https://doi.org/10.1063/1.1799371`.

[22] A. Pukhov and J. Meyer-ter-Vehn. Laser wake field acceleration: The highly non-linear broken-wave regime. *Appl. Phys. B.*, **74**(4):355–361, 2002. ISSN 1432-0649. doi: 10.1007/s003400200795.

[23] W. Lu, C. Huang, M. Zhou, M. Tzoufras, F. S. Tsung, W. B. Mori, and T. Katsouleas. A nonlinear theory for multidimensional relativistic plasma wave wakefields. *Phys. Plasmas*, **13**(5):056709, 2006. ISSN 1070-664X. doi: 10.1063/1.2203364.

[24] S. Bulanov, N. Naumova, F. Pegoraro, and J. Sakai. Particle injection into the wave acceleration phase due to nonlinear wake wave breaking. *Phys. Rev. E*, **58**:R5257–R5260, 1998. doi: 10.1103/PhysRevE.58.R5257. URL `https://link.aps.org/doi/10.1103/PhysRevE.58.R5257`.

[25] M. P. Tooley, B. Ersfeld, S. R. Yoffe, A. Noble, E. Brunetti, Z. M. Sheng, M. R. Islam, and D. A. Jaroszynski. Towards attosecond high-energy electron bunches: Controlling self-injection in laser-wakefield accelerators through plasma-density modulation. *Phys. Rev. Lett.*, **119**:044801, 2017. doi: 10.1103/PhysRevLett.119.044801. URL `https://link.aps.org/doi/10.1103/PhysRevLett.119.044801`.

[26] I. Kostyukov, E. Nerush, A. Pukhov, and V. Seredov. A multidimensional theory

for electron trapping by a plasma wake generated in the bubble regime. *New J. Phys.*, **12**(4):045009, 2010. ISSN 1367-2630.

[27] A. G. R. Thomas. Scalings for radiation from plasma bubbles. *Phys. Plasmas*, **17**(5):056708, 2010. doi: 10.1063/1.3368678. URL `https://doi.org/10.1063/1.3368678`.

[28] X. Yang, E. Brunetti, D. Reboredo Gil, G.H. Welsh, F.Y. Li, S. Cipiccia, B. Ersfeld, D.W. Grant, P.A. Grant, M.R. Islam, M.P. Tooley, G. Vieux, S.M. Wiggins, Z.M. Sheng, and D.A. Jaroszynski. Three electron beams from a laser-plasma wakefield accelerator and the energy apportioning question. *Sci. Rep.*, **7**, 2017. ISSN 2045-2322. doi: 10.1038/srep43910.

[29] D. Swanson. *Plasma Waves (2nd edition)*, volume **45**. Institute of Physics, 2003. doi: 10.1088/0741-3335/45/6/701.

[30] M. L. Boas. *Mathematical methods in the physical sciences.* Wiley, Hoboken, NJ, 3rd edition, 2006. ISBN 9780471198260.

[31] C. .K Birdsall and A. B. Langdon. *Plasma physics via computer simulation.* McGraw-Hill, New York, 1985. ISBN 0070053715.

[32] K. S. Yee. Numerical solution of initial boundary value problems involving maxwell's equations in isotropic media. *IEEE Transactions on Antennas and Propagation*, **14**(3):302–307, 1966. ISSN 0018-926X.

[33] T. D. Arber, K. Bennett, C. S. Brady, A. Lawrence-Douglas, M. G. Ramsay, N. J. Sircombe, P. Gillies, R. G. Evans, H. Schmitz, A. R. Bell, and C. P. Ridgers.

Contemporary particle-in-cell approach to laser-plasma modelling. *Plasma Phys. Control. Fusion*, **57**(11):1–26, 2015.

[34] H. Abe, J. Miyamoto, and R. Itatani. Grid effects on the plasma simulation by the finite-sized particle. *J. Comput. Phys.*, **19**(2):134–149, 1975. ISSN 0021-9991. doi: 10.1016/0021-9991(75)90085-6.

[35] R. A. Fonseca, L. O. Silva, F. S. Tsung, V. K. Decyk, W. Lu, C. Ren, W. B. Mori, S. Deng, S. Lee, T. Katsouleas, and J. C. Adam. Osiris: A three-dimensional, fully relativistic particle in cell code for modeling plasma based accelerators. In Peter M. A. Sloot, Alfons G. Hoekstra, C. J. Kenneth Tan, and Jack J. Dongarra, editors, *Computational Science — ICCS 2002*, pages 342–351, Berlin, Heidelberg, 2002. Springer Berlin Heidelberg. ISBN 978-3-540-47789-1.

[36] A. Vanthieghem, M. Lemoine, and L. Gremillet. Stability analysis of a periodic system of relativistic current filaments. *Phys. Plasmas*, **25** (7):072115, 2018. ISSN 1070-664X. doi: 10.1063/1.5033562. URL `https://aip.scitation.org/doi/10.1063/1.5033562`.

[37] D. Branch. *Supernova Explosions [internet resource]*. Astronomy and astrophysics library. Springer, 1st ed. 2017.. edition, 2017. ISBN 9783662550540.

[38] K. Quinn, L. Romagnani, B. Ramakrishna, G. Sarri, M. E. Dieckmann, P. A. Wilson, J. Fuchs, L. Lancia, A. Pipahl, T. Toncian, O. Willi, R. J. Clarke, M. Notley, A. Macchi, and M. Borghesi. Weibel-induced filamentation during an ultrafast

laser-driven plasma expansion. *Phys. Rev. Lett.*, **108**(13):135001–135001, 2012. ISSN 00319007. URL `http://search.proquest.com/docview/1010496217/`.

[39] Z. Mikić and M. A. Lee. An introduction to theory and models of cmes, shocks, and solar energetic particles. In *Coronal Mass Ejections*, volume **21** of *Space Sciences Series of ISSI*, pages 57–80. Springer New York, 2006. ISBN 9780387450865.

[40] N. Gopalswamy, Z. Mikić, D. Maia, D. Alexander, H. Cremades, P. Kaufmann, D. Tripathi, and Y. M. Wang. The pre-cme sun: Report of working group e. In *Coronal Mass Ejections*, volume **21** of *Space Sciences Series of ISSI*, pages 303–339. Springer New York, New York, NY, 2006. ISBN 9780387450865.

[41] A. Biancalani, A. Bottino, S. Briguglio, A. Könies, P. Lauber, A. Mishchenko, E. Poli, B. D. Scott, and F. Zonca. Linear gyrokinetic particle-in-cell simulations of Alfvén instabilities in tokamaks. *Phys. Plasmas*, **23**(1):12108, 2016. ISSN 1070-664X.

[42] Y. Shen, J.Q. Dong, A.P. Sun, M.K. Han, H.R. Du, Z.X. Wang, H.D. He, Z.X. He, L.F. Wang, and J.L. Wang. Impurity induced kinetic shear Alfvén and kinetic ballooning instabilities in tokamak plasmas. *Nucl. Fusion*, **58**(1):14004, 2017. ISSN 0029-5515.

[43] E. J. Strait. Magnetic control of magnetohydrodynamic instabilities in tokamaks. *Phys. Plasmas*, **22**(2):21803, 2015. ISSN 1070-664X.

[44] N. A. Krall and A. W. Trivelpiece. *Principles of plasma physics.* San Francisco Press, 1986.

[45] J. J. Sakurai. *Modern quantum mechanics.* Pearson Education, second edition, 2014. ISBN 9781292037158.

[46] D. Bohm and E. P. Gross. Theory of plasma oscillations. a. origin of medium-like behavior. *Phys. Rev.*, **75**:1851–1864, 1949. doi: 10.1103/PhysRev.75.1851. URL `https://link.aps.org/doi/10.1103/PhysRev.75.1851`.

[47] R. C. Davidson. *Physics of nonneutral plasmas.* Imperial College Press ; World Scientific, London : Singapore ; River Edge, NJ, 2001. ISBN 1860943020.

[48] A. B Mikhailovskii and O. G Onishchenko. Drift instabilities of a relativistic plasma. part 1. kinetic description of drift effects in a relativistic plasma. *J. Plasma Phys.*, **37**(1):15–28, 1987. ISSN 0022-3778.

[49] A. B. Mikhailovskii. *Electromagnetic instabilities in an inhomogeneous plasma.* Institute of Physics, 1st edition, 1992. ISBN 0750301821.

[50] M. Lazar, R. Schlickeiser, and P. K. Shukla. Cumulative effect of the filamentation and weibel instabilities in counterstreaming thermal plasmas. *Phys. Plasmas*, **13**(10):102107, 2006. doi: 10.1063/1.2357047. URL `https://doi.org/10.1063/1.2357047`.

[51] C. B. Schroeder and E. Esarey. Relativistic warm plasma theory of nonlinear laser-driven electron plasma waves. *Phys. Rev. E*, **81**:056403, 2010. doi: 10.1103/PhysRevE.81.056403. URL `https://link.aps.org/doi/10.1103/PhysRevE.81.056403`.

[52] D. A. Burton and A. Noble. Longitudinal wave-breaking limits in a unified geometric model of relativistic warm plasmas. *J. Phys. A Math. Theor.*, **43**(7):075502, 2010. doi: 10.1088/1751-8113/43/7/075502. URL `https://doi.org/10.1088/1751-8113/43/7/075502`.

[53] B Lehnert. Basic features of plasma instabilities. Technical report, Kungliga Tekniska Hoegskolan, 1972. URL `https://www.osti.gov/biblio/4586585`.

[54] A. Bret, M. C. Firpo, and C. Deutsch. Bridging the gap between two stream and filamentation instabilities. *Laser Part. Beams*, **23**(3):375–383, 2005. doi: 10.1017/S0263034605050536.

[55] A. Bret. Hierarchy of instabilities for two counter-streaming magnetized pair beams. *Phys. Plasmas*, **23**(6):062122, 2016. doi: 10.1063/1.4954307. URL `https://doi.org/10.1063/1.4954307`.

[56] A. Bret, L. Gremillet, and C. Deutsch. Oblique instabilities in relativistic electron beam plasma interaction. In *Proceedings of the 16th International Symposium on Heavy Ion Inertial Fusion*, volume **577**, pages 317 – 319, 2007. doi: https://doi.org/10.1016/j.nima.2007.02.021. URL `http://www.sciencedirect.com/science/article/pii/S0168900207003713`. Proceedings of the 16th International Symposium on Heavy Ion Inertial Fusion.

[57] R. J. Briggs. *Electron-stream interaction with plasmas.* M.I.T. Press Cambridge, 1964.

[58] P. A. Sturrock. Kinematics of growing waves. *Phys. Rev.*, **112**(5):1488–1503, 1958. ISSN 0031-899X.

[59] F. Haas and B. Eliasson. A new two-stream instability mode in magnetized quantum plasma. *Phys. Scr.*, **90**, 2015.

[60] F. Bret, A .and Haas. Connection between the two branches of the quantum two-stream instability across the k space. *Phys. Plasmas*, **17**(5):052101–052101–5, 2010. ISSN 1070-664X.

[61] E. S. Weibel. Spontaneously growing transverse waves in a plasma due to an anisotropic velocity distribution. *Phys. Rev. Lett.*, **2**:83–84, 1959. doi: 10.1103/PhysRevLett.2.83. URL `https://link.aps.org/doi/10.1103/PhysRevLett.2.83`.

[62] B. D. Fried. Mechanism for instability of transverse plasma waves. *Phys. Fluids*, **2**(3):337–337, 1959. doi: 10.1063/1.1705933. URL `https://aip.scitation.org/doi/abs/10.1063/1.1705933`.

[63] R. C. Davidson, D. A. Hammer, I. Haber, and C. E. Wagner. Nonlinear development of electromagnetic instabilities in anisotropic plasmas. *Phys. Fluids*, **15**(2): 317–333, 1972. ISSN 0031-9171.

[64] M. Sarrat, D. Del Sarto, and A. Ghizzo. A pressure tensor description for the time-resonant weibel instability. *J. Plasma Phys.*, **83**(1):705830103, 2017. doi: 10.1017/S0022377816001264.

[65] Q. Jia, H. B. Cai, W. W. Wang, S. P. Zhu, Z. M. Sheng, and X. T. He. Effects of the background plasma temperature on the current filamentation instability. *Phys. Plasmas*, **20**(3):032113, 2013. doi: 10.1063/1.4796052. URL `https://doi.org/10.1063/1.4796052`.

[66] A. Bret, L. Gremillet, D. Bénisti, and E. Lefebvre. Exact relativistic kinetic theory of an electron-beam-plasma system: Hierarchy of the competing modes in the system-parameter space. *Phys. Rev. Lett.*, **100**(20), 2008. doi: 0031-9007.

[67] A. Meurer, C. P. Smith, M. Paprocki, O. Čertík, S. B. Kirpichev, M. Rocklin, S. Kumar, A.and Ivanov, J. K. Moore, T. Singh, S.and Rathnayake, S. Vig, B. E. Granger, R. P. Muller, F. Bonazzi, H. Gupta, S. Vats, F. Johansson, F. Pedregosa, M. J. Curry, Andy R. T., Š. Roučka, A. Saboo, I. Fernando, S. Kulal, R. Cimrman, and A. Scopatz. Sympy: symbolic computing in python. *J. Comput. Sci.*, **3**:e103, 2017. ISSN 2376-5992. doi: 10.7717/peerj-cs.103. URL `https://doi.org/10.7717/peerj-cs.103`.

[68] A. Bret. A simple analytical model for the weibel instability in the non-relativistic regime. *Phys. Lett. A*, **359**(1):52–55, 2006. doi: 10.1016//j.physleta.2006.05.081.

[69] J. G. Siambis. Relativistic fluid equations for intense electron beams. *Phys. Fluids*, **30**(3):896–903, 1987. doi: 10.1063/1.866343. URL `https://aip.scitation.org/doi/abs/10.1063/1.866343`.

[70] W. A. Newcomb. Warm relativistic electron fluid. *Phys. Fluids*, **25**(5):846–851, 1982. ISSN 0031-9171.

[71] S. Pennisi and A. M. Anile. Fluid models for relativistic electron beams: An independent derivation. *Phys. Fluids. B, Plasma Phys.*, **3**(4):1091–1103, 1991. ISSN 0899-8221.

[72] M. Tzoufras, C. Ren, F. S. Tsung, J. W. Tonge, W. B. Mori, M. Fiore, R. A. Fonseca, and L. O. Silva. Space-charge effects in the current-filamentation or weibel instability. *Phys. Rev. Lett.*, **96**:105002, 2006. doi: 10.1103/PhysRevLett.96.105002. URL `https://link.aps.org/doi/10.1103/PhysRevLett.96.105002`.

[73] A. Bret, M.C. Firpo, and C. Deutsch. Between two stream and filamentation instabilities: Temperature and collisions effects. *Laser Part. Beams*, **24**(1):27–33, 2006. ISSN 0263-0346.

[74] F. Califano, F. Pegoraro, and S.V. Bulanov. Spatial structure and time evolution of the weibel instability in collisionless inhomogeneous plasmas. *Phys. Rev. E*, **56** (1):963–969, 1997. ISSN 1063-651X.

[75] F. Catapano, A.V. Artemyev, G. Zimbardo, and I.Y. Vasko. Current sheets with inhomogeneous plasma temperature: Effects of polarization electric field and 2d solutions. *Phys. Plasmas*, **22**(9):92905, 2015. ISSN 1070-664X.

[76] A. A. Stepanenko. Cumulative impact of electromagnetic effects and inhomogeneous temperature distribution on dynamics of plasma filaments at the tokamak edge. *Plasma Phys. Rep.*, **47**(1):1–17, 2021. ISSN 1063-780X.

[77] M. Choudhary, S. Mukherjee, and P. Bandyopadhyay. Experimental observation of self excited co-rotating multiple vortices in a dusty plasma with inhomogeneous

plasma background. *Phys. Plasmas*, **24**(3):033703, 2017. doi: 10.1063/1.4977454. URL `https://doi.org/10.1063/1.4977454`.

[78] R. A. Caldela, R. S. Schneider, and L. F. Ziebell. The dispersion relation and the dielectric tensor of inhomogeneous magnetized plasmas. *J. Plasma Phys.*, **42**(1): 165–175, 1989. doi: 10.1017/S0022377800014240.

[79] H. L. Berk and R. R. Dominguez. Variational method for electromagnetic waves in a magneto-plasma. *J. Plasma Phys.*, **18**(1):31–48, 1977. doi: 10.1017/S0022377800020869.

[80] S. Kalmykov, S. A. Yi, V. Khudik, and G. Shvets. Electron Self-Injection and Trapping into an Evolving Plasma Bubble. *Phys. Rev. Lett.*, **103**(13):135004, 2009. doi: 10.1103/PhysRevLett.103.135004. URL `https://link.aps.org/doi/10.1103/PhysRevLett.103.135004`. American Physical Society.

[81] D. Kaganovich, D. F. Gordon, and A. Ting. Observation of Large-Angle Quasimonoenergetic Electrons from a Laser Wakefield. *Phys. Rev. Lett.*, **100**(21):215002, 2008. doi: 10.1103/PhysRevLett.100.215002. URL `https://link.aps.org/doi/10.1103/PhysRevLett.100.215002`.

[82] L. Zhang, L.M. Chen, W.M. Wang, W.-C. Yan, D.W. Yuan, J.-Y. Mao, Z.H. Wang, C. Liu, Z.W. Shen, A. Faenov, T. Pikuz, D.Z. Li, Y.T. Li, Q.L. Dong, X. Lu, J.L. Ma, Z.Y. Wei, Z.M. Sheng, and J. Zhang. Electron acceleration via high contrast laser interacting with submicron clusters. *Appl. Phys.*

Lett., **100**(1):014104, 2012. ISSN 0003-6951. doi: 10.1063/1.3673911. URL `https://aip.scitation.org/doi/full/10.1063/1.3673911`.

[83] X. Yang, E. Brunetti, D. Reboredo Gil, G. H. Welsh, F. Y. Li, S. Cipiccia, B. Ersfeld, D. W. Grant, P. A. Grant, M. R. Islam, M. P. Tooley, G. Vieux, S. M. Wiggins, Z. M. Sheng, and D. A. Jaroszynski. Three electron beams from a laser-plasma wakefield accelerator and the energy apportioning question. *Sci. Rep.*, **7**:43910, 2017. ISSN 2045-2322. doi: 10.1038/srep43910. URL `http://www.nature.com/srep/2017/170310/srep43910/full/srep43910.html`.

[84] K. Behm, A. Hussein, T. Z. Zhao, S. Dann, B. X. Hou, V. Yanovsky, J. Nees, A. Maksimchuk, W. Schumaker, A. G. R. Thomas, and K. Krushelnick. Measurements of electron beam ring structures from laser wakefield accelerators. *Plasma Phys. Control. Fusion*, **61**(6):065012, 2019. ISSN 0741-3335. doi: 10.1088/1361-6587/ab0622. URL `https://iopscience.iop.org/article/10.1088/1361-6587/ab0622`.

[85] E. Brunetti, X. Yang, F. Y. Li, D. Reboredo Gil, G. H. Welsh, S. Cipiccia, B. Ersfeld, D. W. Grant, P. A. Grant, M. R. Islam, M. Shahzad, M. P. Tooley, G. Vieux, S. M. Wiggins, Z. M. Sheng, and D. A. Jaroszynski. Wide-angle electron beams from laser-wakefield accelerators. In *Laser Acceleration of Electrons, Protons, and Ions IV*, volume **10240**, page 102400P. International Society for Optics and Photonics, 2017. doi: 10.1117/12.2269314.

[86] J. L. Shaw, M. A. Romo-Gonzalez, N. Lemos, P. M. King, G. Bruhaug, K. G. Miller, C. Dorrer, B. Kruschwitz, L. Waxer, G. J. Williams, M. V. Ambat, M. M.

McKie, M. D. Sinclair, W. B. Mori, C. Joshi, Hui Chen, J. P. Palastro, F. Albert, and D. H. Froula. Microcoulomb laser plasma accelerator on OMEGA EP. *Sci. Rep.*, **11**(1):7498, 2021. ISSN 2045-2322. doi: 10.1038/s41598-021-86523-5. URL `https://www.nature.com/articles/s41598-021-86523-5`.

[87] J. G. Trump, E. W. Merrill, and K. A. Wright. Disinfection of sewage wastewater and sludge by electron treatment. *Radiation Physics and Chemistry*, **24** (1):55–66, 1984. ISSN 0146-5724. doi: 10.1016/0146-5724(84)90007-4. URL `http://www.sciencedirect.com/science/article/pii/0146572484900074`.

[88] Z.-H. He, A. G. R. Thomas, B. Beaurepaire, J. A. Nees, B. Hou, V. Malka, K. Krushelnick, and J. Faure. Electron diffraction using ultrafast electron bunches from a laser-wakefield accelerator at kHz repetition rate. *Appl. Phys Lett.*, **102**(6):064104, 2013. ISSN 0003-6951. doi: 10.1063/1.4792057. URL `http://aip.scitation.org/doi/10.1063/1.4792057`.

[89] D. A. Oulianov, R. A. Crowell, D. J. Gosztola, I. A. Shkrob, O. J. Korovyanko, and R. C. Rey-de Castro. Ultrafast pulse radiolysis using a terawatt laser wakefield accelerator. *J. Appl. Phys.*, **101**(5): 053102, 2007. ISSN 0021-8979. doi: 10.1063/1.2696204. URL `https://aip.scitation.org/doi/10.1063/1.2696204`.

[90] X. Yang, E. Brunetti, and D. A. Jaroszynski. High-energy coherent terahertz radiation emitted by wide-angle electron beams from a laser-wakefield accelerator. *New J. Phys.*, **20**(4):043046, 2018. ISSN 1367-2630. doi: 10.1088/1367-2630/aab74d. URL `http://stacks.iop.org/1367-2630/20/i=4/a=043046`.

[91] J. F. Qu, X. F. Li, X. Y. Liu, P. Liu, Y. J. Song, Z. Fu, Q. Yu, and Q. Kong. Terahertz radiation generated by shell electrons in the bubble regime via the interaction between an intense laser and underdense plasma. *Phys. Plasmas*, **26**(3):033115, 2019. ISSN 1070-664X. doi: 10.1063/1.5079437. URL `https://aip.scitation.org/doi/full/10.1063/1.5079437`.

[92] D. Branch and J. D. Wheeler. *Supernova Explosions*. Astronomy and astrophysics library. Springer, 1st edition, 2017. ISBN 9783662550540.

[93] D. Alexander. An introduction to the pre-CME corona. In *Coronal Mass Ejections*, volume **21** of *Space Sciences Series of ISSI*, pages 81–92. Springer New York, New York, NY, 2006. ISBN 9780387450865.

[94] J. M. Hill, M. H. Key, S. P. Hatchett, and R. R. Freeman. Beam-Weibel filamentation instability in near-term and fast-ignition experiments. *Phys. Plasmas*, **12**(8):082304, 2005. ISSN 1070-664X. doi: 10.1063/1.1986988. URL `https://aip.scitation.org/doi/10.1063/1.1986988`.

[95] C. Méndez, O. Varela, E. García, I. Hernández, J. Ajates, J. D. Pisonero, J. L. Sagredo, M. Olivar, and L. Roso. VEGA laser facility beamlines management for pump-probe experiments. In *Fourth International Conference on Applications of Optics and Photonics*, volume **11207**, page 112071Z. International Society for Optics and Photonics, 2019. doi: 10.1117/12.2527481.

[96] L. Volpe, R. Fedosejevs, G. Gatti, J. A. Pérez-Hernández, C. Méndez, J. Apiñaniz, X. Vaisseau, C. Salgado, M. Huault, S. Malko, G. Zeraouli, V. Ospina, A. Long-

man, D. De Luis, K. Li, O. Varela, E. García, I. Hernández, J. D. Pisonero, J. García Ajates, J. M. Alvarez, C. García, M. Rico, D. Arana, J. Hernández-Toro, and L. Roso. Generation of high energy laser-driven electron and proton sources with the 200 TW system VEGA 2 at the Centro de Laseres Pulsados. *High Power Laser Sci. Eng.*, **7**:E25, 2019. ISSN 2095-4719, 2052-3289. doi: 10.1017/hpl.2019.10.

[97] P. Casolaro, L. Campajola, G. Breglio, S. Buontempo, M. Consales, A. Cusano, A. Cutolo, F Di Capua, F. Fienga, and P. Vaiano. Real-time dosimetry with radiochromic films. *Sci. Rep.*, **9**(1):1–11, 2019. ISSN 2045-2322. doi: 10.1038/s41598-019-41705-0. URL `https://www.nature.com/articles/s41598-019-41705-0`.

[98] S. Devic, N. Tomic, and D. Lewis. Reference radiochromic film dosimetry: Review of technical aspects. *Phys. Med.*, **32**(4):541–556, 2016. ISSN 1120-1797. doi: 10.1016/j.ejmp.2016.02.008. URL `http://www.sciencedirect.com/science/article/pii/S112017971600510X`.

[99] S. Agostinelli, J. Allison, K. Amako, J. Apostolakis, H. Araujo, P. Arce, M. Asai, D. Axen, S. Banerjee, G. Barrand, F. Behner, L. Bellagamba, J. Boudreau, L. Broglia, A. Brunengo, H. Burkhardt, S. Chauvie, J. Chuma, R. Chytracek, G. Cooperman, G. Cosmo, P. Degtyarenko, A. Dell'Acqua, G. Depaola, D. Dietrich, R. Enami, A. Feliciello, C. Ferguson, H. Fesefeldt, G. Folger, F. Foppiano, A. Forti, S. Garelli, S. Giani, R. Giannitrapani, D. Gibin, J. J. Gómez Cadenas, I. González, G. Gracia Abril, G. Greeniaus, W. Greiner, V. Grichine, A. Grossheim, S. Guatelli, P. Gumplinger, R. Hamatsu, K. Hashimoto, H. Hasui,

A. Heikkinen, A. Howard, V. Ivanchenko, A. Johnson, F. W. Jones, J. Kallenbach, N. Kanaya, M. Kawabata, Y. Kawabata, M. Kawaguti, S. Kelner, P. Kent, A. Kimura, T. Kodama, R. Kokoulin, M. Kossov, H. Kurashige, E. Lamanna, T. Lampén, V. Lara, V. Lefebure, F. Lei, M. Liendl, W. Lockman, F. Longo, S. Magni, M. Maire, E. Medernach, K. Minamimoto, P. Mora de Freitas, Y. Morita, K. Murakami, M. Nagamatu, R. Nartallo, P. Nieminen, T. Nishimura, K. Ohtsubo, M. Okamura, S. O'Neale, Y. Oohata, K. Paech, J. Perl, A. Pfeiffer, M. G. Pia, F. Ranjard, A. Rybin, S. Sadilov, E. Di Salvo, G. Santin, T. Sasaki, N. Savvas, Y. Sawada, S. Scherer, S. Sei, V. Sirotenko, D. Smith, N. Starkov, H. Stoecker, J. Sulkimo, M. Takahata, S. Tanaka, E. Tcherniaev, E. Safai Tehrani, M. Tropeano, P. Truscott, H. Uno, L. Urban, P. Urban, M. Verderi, A. Walkden, W. Wander, H. Weber, J. P. Wellisch, T. Wenaus, D. C. Williams, D. Wright, T. Yamada, H. Yoshida, and D. Zschiesche. Geant4 a simulation toolkit. *Nucl. Instum. Methods. Phys. Res. B*, **506**(3): 250–303, 2003. ISSN 0168-9002. doi: 10.1016/S0168-9002(03)01368-8. URL `http://www.sciencedirect.com/science/article/pii/S0168900203013688`.

[100] R. Lehe, M. Kirchen, I. A. Andriyash, B. B. Godfrey, and J. L. Vay. A spectral, quasi-cylindrical and dispersion-free Particle-In-Cell algorithm. *Comput. Phys. Commun.*, **203**:66–82, 2016. ISSN 0010-4655. doi: 10.1016/j.cpc.2016.02.007. URL `http://www.sciencedirect.com/science/article/pii/S0010465516300224`.

[101] W. Lu, M. Tzoufras, C. Joshi, F. S. Tsung, W. B. Mori, J. Vieira, R. A.

Fonseca, and L. O. Silva. Generating multi-GeV electron bunches using single stage laser wakefield acceleration in a 3D nonlinear regime. *Phys. Rev. Accel. Beams*, **10**(6):061301, 2007. doi: 10.1103/PhysRevSTAB.10.061301. URL `http://link.aps.org/doi/10.1103/PhysRevSTAB.10.061301`.

[102] B. A. Shadwick, C. B. Schroeder, and E. Esarey. Nonlinear laser energy depletion in laser-plasma accelerators. *Phys. Plasmas*, **16**(5): 056704, 2009. ISSN 1070-664X. doi: 10.1063/1.3124185. URL `https://aip.scitation.org/doi/10.1063/1.3124185`.

[103] S. P. D. Mangles, C. D. Murphy, Z. Najmudin, A. G. R. Thomas, J. L. Collier, A. E. Dangor, E. J. Divall, P. S. Foster, J. G. Gallacher, C. J. Hooker, D. A. Jaroszynski, A. J. Langley, W. B. Mori, P. A. Norreys, F. S. Tsung, R. Viskup, B. R. Walton, and K. Krushelnick. Monoenergetic beams of relativistic electrons from intense laser-plasma interactions. *Nature*, **431** (7008):535–538, 2004. ISSN 1476-4687. doi: 10.1038/nature02939. URL `https://doi.org/10.1038/nature02939`.

[104] C. G. R. Geddes, Cs Toth, J. van Tilborg, E. Esarey, C. B. Schroeder, D. Bruhwiler, C. Nieter, J. Cary, and W. P. Leemans. High-quality electron beams from a laser wakefield accelerator using plasma-channel guiding. *Nature*, **431** (7008):538–541, 2004. ISSN 1476-4687. doi: 10.1038/nature02900. URL `https://doi.org/10.1038/nature02900`.

[105] J. Faure, Y. Glinec, A. Pukhov, S. Kiselev, S. Gordienko, E. Lefebvre, J.-P. Rousseau, F. Burgy, and V. Malka. A laser-plasma accelerator producing mo-

noenergetic electron beams. *Nature*, **431**(7008):541–544, 2004. ISSN 1476-4687. doi: 10.1038/nature02963. URL `https://doi.org/10.1038/nature02963`.

[106] X. Yang, E. Brunetti, D. Reboredo Gil, G.H. Welsh, F.Y. Li, S. Cipiccia, B. Ersfeld, D.W. Grant, P.A. Grant, M.R. Islam, M.P. Tooley, G. Vieux, S.M. Wiggins, Z.M. Sheng, and D.A. Jaroszynski. Three electron beams from a laser-plasma wakefield accelerator and the energy apportioning question. *Sci. Rep.*, **7**, 2017. ISSN 2045-2322. doi: 10.1038/srep43910.

[107] L. I. Inigo Gamiz, B. Ersfeld, E. Brunetti, S. R. Yoffe, R. A. Cairns, A. Noble, G. K. Holt, and D. A. Jaroszynski. Microstructure formation in radially counter-streaming electron flows. *New J. Phys.*, **23**, 2021. doi: 10.1088/1367-2630/abe8f6. URL `https://doi.org/10.1088/1367-2630/abe8f6`.

[108] F. T. Gratton and G. Gnavi. Two-stream instability in convergent geometry. *Phys. Fluids*, **30**(2):548–556, 1987. doi: 10.1063/1.866352. URL `https://aip.scitation.org/doi/abs/10.1063/1.866352`.

[109] Harris C. R., Millman K. J., van der Walt S. J., Gommers R., Virtanen P., Cournapeau D., Wieser E., Taylor J., Berg S., Smith N. J., Kern R., Picus M., Hoyer S., van Kerkwijk M. H., Brett M., Haldane A., Fernández del Río J., Wiebe M., Peterson P., Gérard-Marchant P., Sheppard K., Reddy T., Weckesser W., Abbasi H., Gohlke C., and Oliphant T. E. Array programming with NumPy. *Nature*, **585**(7825):357–362, 2020. doi: 10.1038/s41586-020-2649-2. URL `https://doi.org/10.1038/s41586-020-2649-2`.

[110] A. Ghizzo, D. Del Sarto, and M. Sarrat. Low- and high-frequency nature of oblique filamentation modes. i. linear theory. *Phys. Plasmas*, **27**(7):072103, 2020. doi: 10.1063/5.0003697. URL `https://doi.org/10.1063/5.0003697`.

[111] A. Bret and C. Deutsch. Hierarchy of beam plasma instabilities up to high beam densities for fast ignition scenario. *Phys. Plasmas*, **12**(8):082704, 2005. doi: 10.1063/1.2012067. URL `https://doi.org/10.1063/1.2012067`.

[112] R. A. Fonseca, L. O. Silva, F. S. Tsung, V. K. Decyk, W. Lu, C. Ren, W. B. Mori, S. Deng, S. Lee, T. Katsouleas, and J. C. Adam. Osiris: A three-dimensional, fully relativistic particle in cell code for modeling plasma based accelerators. In Peter M. A. Sloot, Alfons G. Hoekstra, C. J. Kenneth Tan, and Jack J. Dongarra, editors, *Computational Science — ICCS 2002*, pages 342–351, Berlin, Heidelberg, 2002. Springer Berlin Heidelberg. ISBN 978-3-540-47789-1.

[113] A. Matraillain, L. I. Inigo Gamiz, Brunetti E., G. K. Holt, M. Shahzad, G. Vieux, S. R. Yoffe, B. Ersfeld, J. A. Perez-Hernandez, G. Zeraouli, C. Salgado, G. Gatti, L. Volpe, and D. A. Jaroszynski. Generation of ultra-high charge beams from a laser wakefield accelerator driven by a petawatt laser. *Commun Phys., (under review)*, 2022.